AD-A138 872 PHYSICS OF HIGH TEMPERATURE DENSE PLASMAS(U) NEW MEXICO 1/2
UNIV ALBUQUERQUE DEPT OF CHEMICAL AND NUCLEAR
ENGINEERING D M WOODALL JAN 84 AFOSR-TR-84-0124
UNCLASSIFIED AFOSR-79-0060 F/G 20/9 NL

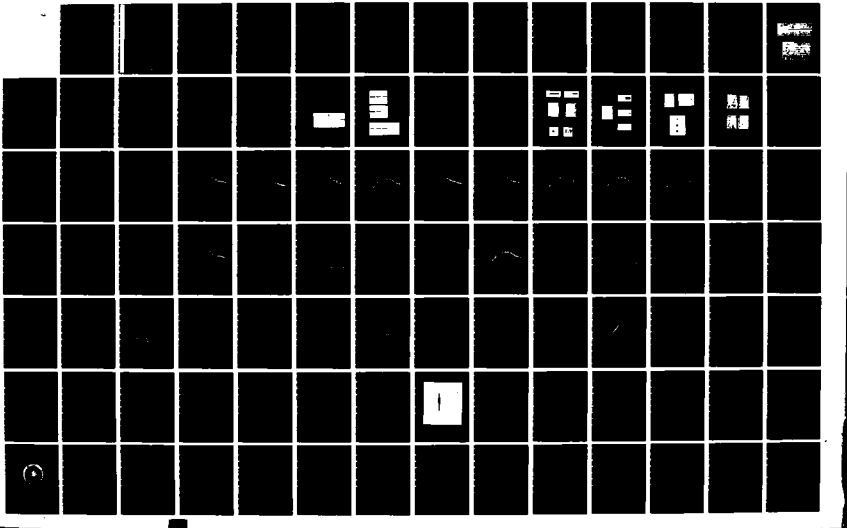

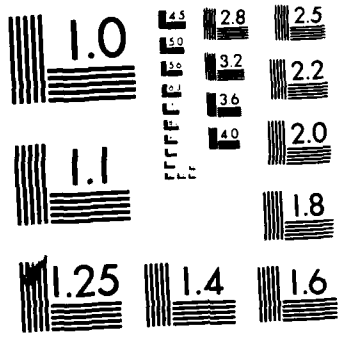

MICROCOPY RESOLUTION TEST CHART
NATIONAL BUREAU OF STANDARDS-1963-A

THE UNIVERSITY OF NEW MEXICO
COLLEGE OF ENGINEERING

BUREAU OF ENGINEERING RESEARCH

Final Report

PHYSICS OF HIGH TEMPERATURE, DENSE PLASMAS

by

David M. Woodall

Report No. NE-100(84)AFOSR-765-2
Work performed under AFOSR Grant AFOSR-79-0060

January 1984

UNCLASSIFIED

SECURITY CLASSIFICATION OF THIS PAGE (When Data Entered)

REPORT DOCUMENTATION PAGE		READ INSTRUCTIONS BEFORE COMPLETING FORM
1. REPORT NUMBER AFOSR-TR- 84-0124	2. GOVT ACCESSION NO. AD-A138872	3. RECIPIENT'S CATALOG NUMBER
4. TITLE (and Subtitle) PHYSICS OF HIGH TEMPERATURE, DENSE PLASMAS		5. TYPE OF REPORT & PERIOD COVERED FINAL 1 Feb 79 - 30 Jun 82 6. PERFORMING ORG. REPORT NUMBER
7. AUTHOR(s) David M. Woodall		8. CONTRACT OR GRANT NUMBER(s) AFOSR-79-0060
9. PERFORMING ORGANIZATION NAME AND ADDRESS University of New Mexico College of Engineering Albuquerque, NM 87131		10. PROGRAM ELEMENT, PROJECT, TASK AREA & WORK UNIT NUMBERS 61102F 2301/A7
11. CONTROLLING OFFICE NAME AND ADDRESS AFOSR/NP Bolling AFB, DC 20332		12. REPORT DATE January 1984 13. NUMBER OF PAGES 171
14. MONITORING AGENCY NAME & ADDRESS(if different from Controlling Office)		15. SECURITY CLASS. (of this report) UNCLASSIFIED 15a. DECLASSIFICATION DOWNGRADING SCHEDULE

16. DISTRIBUTION STATEMENT (of this Report)

Approved for public release;
distribution unlimited.

17. DISTRIBUTION STATEMENT (of the abstract entered in Block 20, if different from Report)

18. SUPPLEMENTARY NOTES

19. KEY WORDS (Continue on reverse side if necessary and identify by block number)

20. ABSTRACT (Continue on reverse side if necessary and identify by block number)

The research undertaken under the AFOSR Grant included three related projects: the production and characterization of a dense plasma target for a REB-Plasma and REB-Neutral Gas heating experiment, the development of plasma diagnostics for REB-Plasma and REB-Neutral Gas heating experiments, and finally, the development of soft x-ray diagnostic techniques of imploding liner experiments.

DD FORM 1 JAN 73 1473

UNCLASSIFIED

SECURITY CLASSIFICATION OF THIS PAGE (When Data Entered)

Final Report

PHYSICS OF HIGH TEMPERATURE, DENSE PLASMAS

by

David M. Woodall

Department of Chemical and Nuclear Engineering
The University of New Mexico
Albuquerque, New Mexico 87131

Report No. NE-100(84)AFOSR-765-2
Work Performed under AFOSR Grant 79-0060

January 1984

TABLE OF CONTENTS

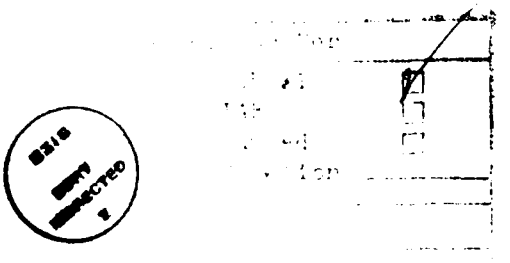

A-1

I. Introduction

This report summarizes work completed under Air Force Office of Scientific Research Grant 79-0060 to the University of New Mexico. The grant spanned the period of February 1, 1979 to June 30, 1982. The Principal Investigator was Professor David M. Woodall of the Department of Chemical and Nuclear Engineering at UNM. The research undertaken under the grant was performed primarily at the Air Force Weapons Laboratory with the Advanced Concepts Branch of the Nuclear Technology Office. A number of graduate research assistants worked with Professor Woodall on the project, and their contributions are noted in the appropriate section of this document. Many of the members of the technical staff at AFWL provided valuable assistance in the completion of this work.

The research undertaken under the AFOSR Grant included three related projects: the production and characterization of a dense plasma target for a REB-Plasma and REB-Neutral Gas heating experiment, the development of plasma diagnostics for REB-Plasma and REB-Neutral Gas heating experiments, and finally, the development of soft x-ray diagnostic techniques of imploding liner experiments. This report has three principal sections, each of which constitutes an independent report on one of the above topics. Section II, "Characterization of a Dense Plasma Source," summarizes the results of the plasma gun research activities undertaken. That work was in the plasma target production and characterization area for planned REB-Plasma heating experiments, to take place at AFWL. The work described was performed primarily by Dr. L. K. Len in his dissertation research. Because of programmatic modification of the use of the PR-1590 in the intense beam program at AFWL, those heating experiments have not yet been completed. Section III, "Intense REB-Neutral Gas Heating Experiments," details the result of diagnostic development for experiments performed in this area at AFWL. Section IV,

"Space and Time Resolved Spectroscopy of High Energy Density Aluminum Plasmas," presents results of such measurements made on the plasma produced by the SHIVA imploding foil experiment at AFWL. The work detailed in sections III and IV was primarily the effort of Dr. G. F. Kiuttu in his dissertation research. This document concludes with section V, an appendix containing a summary of technical presentations and publications supported by and/or reporting work under this grant. Because of the relative independence of each technical section, the references for each section are independently numbered and follow each section.

II. Characterization of a Dense Plasma Source

L. K. Len and D. Woodall

There has developed recently considerable interest in the anomalous heating of a dense plasma by a relativistic electron beam [1-3]. Low power experiments [4] have indicated that the relativistic two-stream instability can cause a significant enhancement over the energy deposition expected classically. Calculations indicate that scaling to currently available power supplies would allow a plasma of 10^{18}-$10^{20}/cm^3$ density to be heated to 30-50 kev. Our goal has been to produce a fully-ionized hydrogen plasma with a density of $2x10^{18}/cm^3$ and a temperature of 5-10 eV with small spatial gradients. That plasma is to be used in a REB-plasma heating experiment with the low divergence, annular beam from the PR1590 [5]. The work reported here is in the operation and characterization of the plasma source for such an experiment.

A. *Description of Experiment*

Our experiments took place in the Plasma Physics Laboratory at the Electron Beam facilities at the Air Force Weapons Laboratory. The plasma source used in the experiments is a co-axial plasma gun [6,7] which is capable of operating either in prefilled mode or puffed mode. In the prefilled mode, the plasma gun chamber is operated with a backfill of the desired gas at a selected pressure. In this case the gun operates in the "snowplow" mode whereby the plasma sheath sweeps up the neutral gas in front of it and subsequently ionizes it.

In the puffed mode the chamber is evacuated to below 1 mtorr, and the gun discharge is initiated by the puffing of gas into the back of the gun by an electromagnetic puff valve. The puff valve is backed by a gas plenum pressurized to 20 psi of gas and is operated with a capacitive discharge through a coil. When a capacitor (40 μF) charged to 1-5 kV is allowed to discharge through the coil, it opens up the valve for a short period (on

the order of a msec) and the puff of gas that enters is capable of filling the gun up to a few torr of pressure. In the puffed mode, the gun operation is mainly via the deflagration process with the gas discharge staying near the insulator. The various components of the gun are shown in Figure II.1.

Figure II.2 shows a diagram of the experimental set-up. The main capacitor bank is comprised of six 40 μF (10 kV) capacitors connected in parallel. It is switched by using a krytron trigger circuit and an ignitron switch. A crowbar circuit is incorporated to avoid unwanted LC ringing. The quartz windows of the vacuum chamber are used for optical diagnostic access. The plasma was fired in both operating modes into a longitudinal magnetic field. Since the REB-plasma heating experiments are to take place in 50-100 kG fields, it is necessary to inject the plasma into such a field. The external magnet around the drift-tube is capable of producing a field in excess of 50 kG. It is driven by a set of twelve 180 μF (8 kV) capacitors. Timing of the firing sequence is accomplished by a Maxwell trigger-delay generator unit. All measurements and signals are recorded on Tektronix 7000 series oscilloscopes.

The main objective of our experiment is to produce a high-density, fully-ionized plasma target for a relativistic electron beam (REB) heating experiment. The desired plasma parameters are $n > 10^{18}$ cm^{-3} at a few electron volts with small spatial gradients. Since our REB machine (Pulserad 1590) produces a cold annular beam, an annular plasma target is preferred.

In this paper, we report on studies of the longitudinal injection of the plasma into a magnetic field and on the various diagnostics for the measurement of the plasma density and temperature. Our diagnostics include visible light spectroscopy (Stark-broadening of H_β line), B-dot probe measurements, Rogowski current monitors, bank voltage measurements, and streak and framing photography.

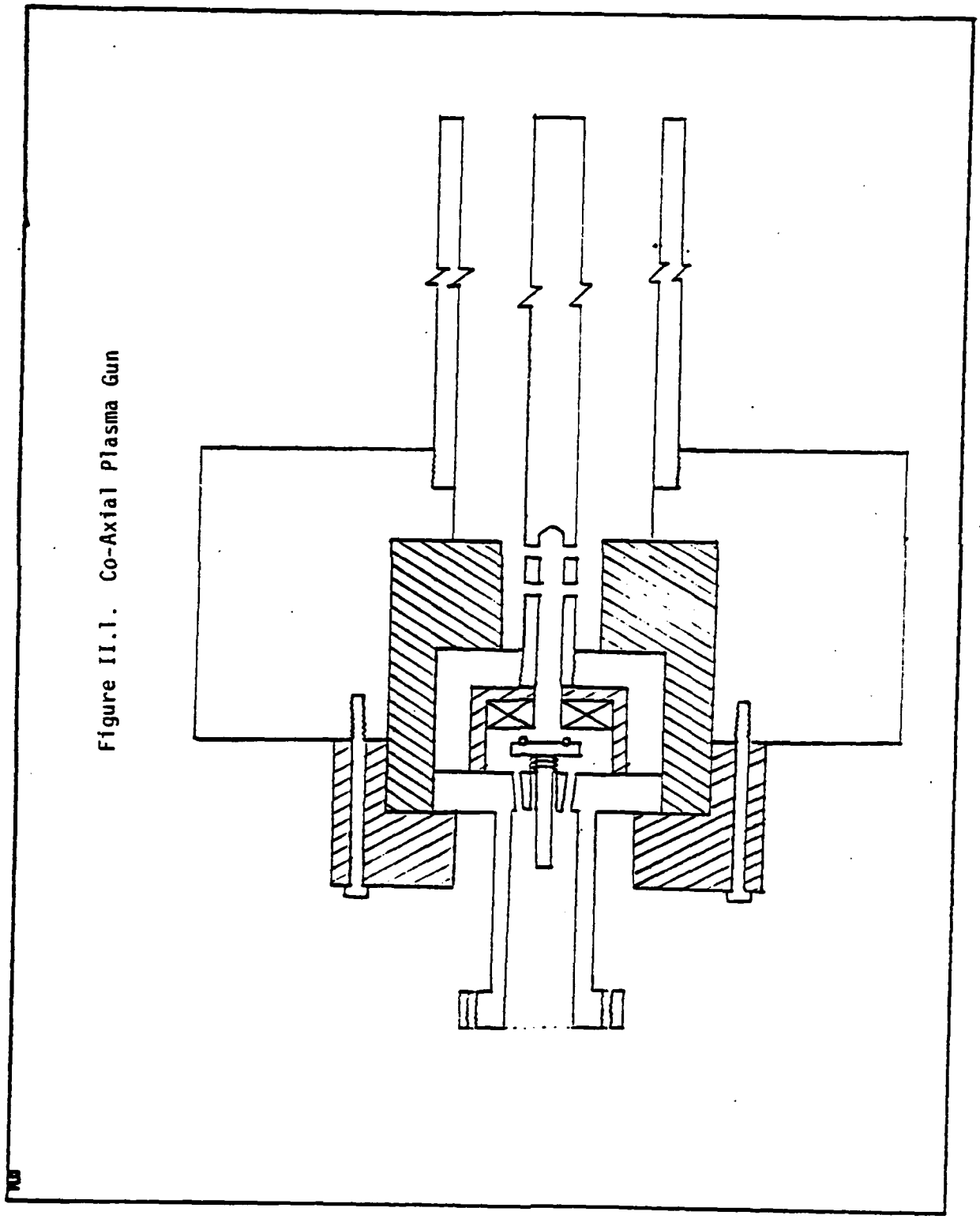

Figure II.1. Co-Axial Plasma Gun

Figure II.2. Experimental Arrangement

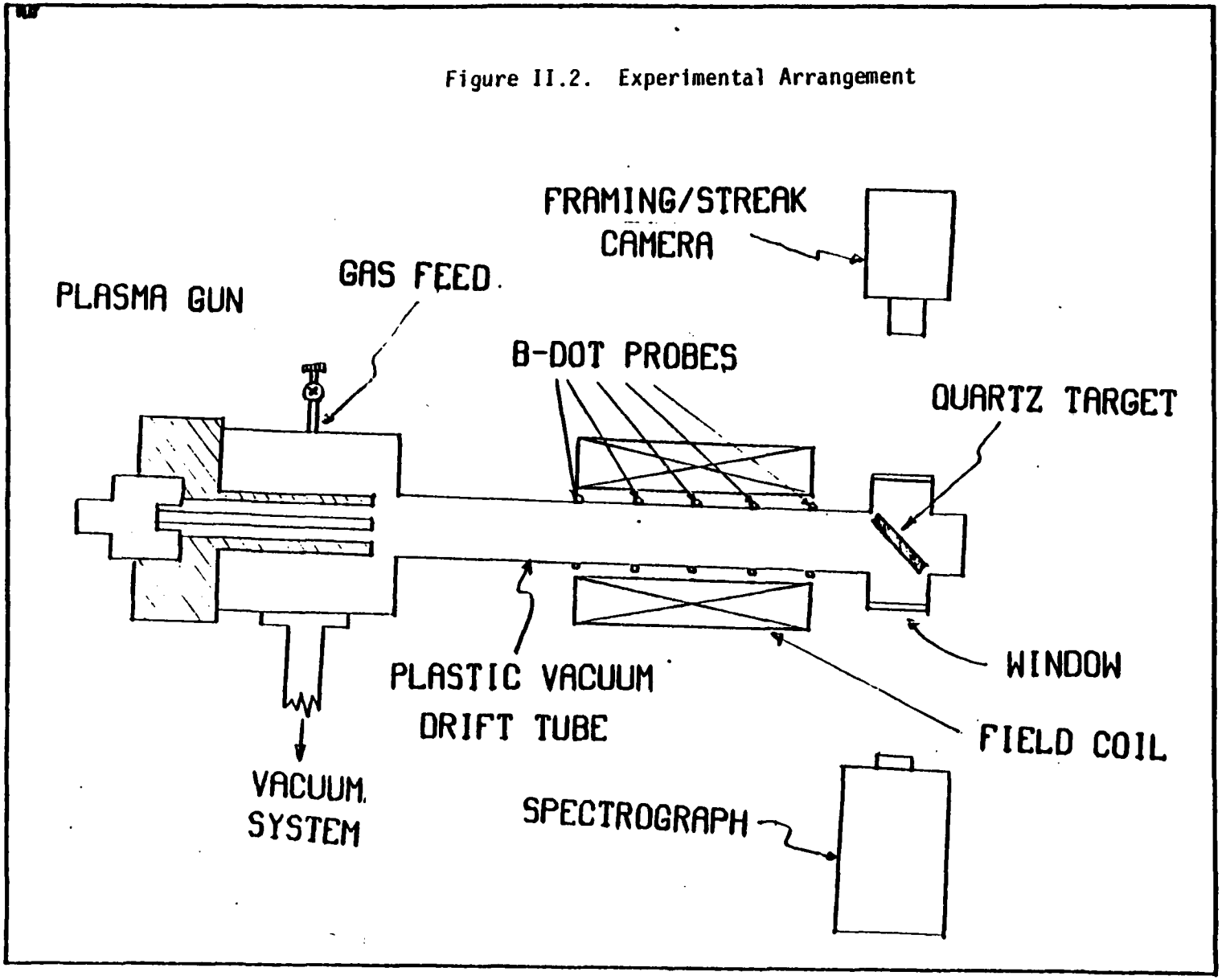

1. Stark Broadening Measurement of the Hβ Line of Hydrogen

A half-meter visible spectrogrpah (Jarrell Ash, Ebert scanning spectrometer, Model 82-000) was used to obtain a time-integrated spctrum of the plasma. The spectra were recorded on polaroid type 57 film (ASA 3000), and were then analyzed using an analysis scheme developed by Dr. M. Collins Clark of AFWL. The program running on a PDP 11/60 digitizes the spectra (with the use of a (Colorado Video) vidicon camera and an image di ..i-zer). The output is in two forms namely, a 2-D array o ntensities, and a plot of the special intensity along an en y scan. In order to minimize measurement errors (primari ec-tronic noise in the vidicon system), the computer averages data over 1000 line-scans. Measurements were made for both the prefilled and the puffed modes of operation. These measurements were done with no external magnetic field. The drift tube in this experiment was stainless steel and the insulator used in the gun was quartz. Subsequent experiments were performed with quartz and plastic drift tubes to observe the spatial variation of plasma visible light emission.

a. Prefilled Mode

The spectra for different prefilled pressures at 7 kV bank voltage are shown in Figure II.3. It can be seen that the plasma is quite clean, with only a small amount of Cu and Al lines which originated from the electrodes of the gun. Those lines probably appear late in time, after the discharge is over. Figures II.4 (a), (b), and (c) show some spectra plotted by the PDP 11/60. As the density of the plasma increases, there is a corresponding increase of the H_β linewidth. The densities calculated are listed in Table II.1. Since the energy supplied remains constant (9 kV charge) as the prefilled pressure is being increased, the percentage of ionization drops (last column in Table II.1).

Figure II.3. Prefill Operation

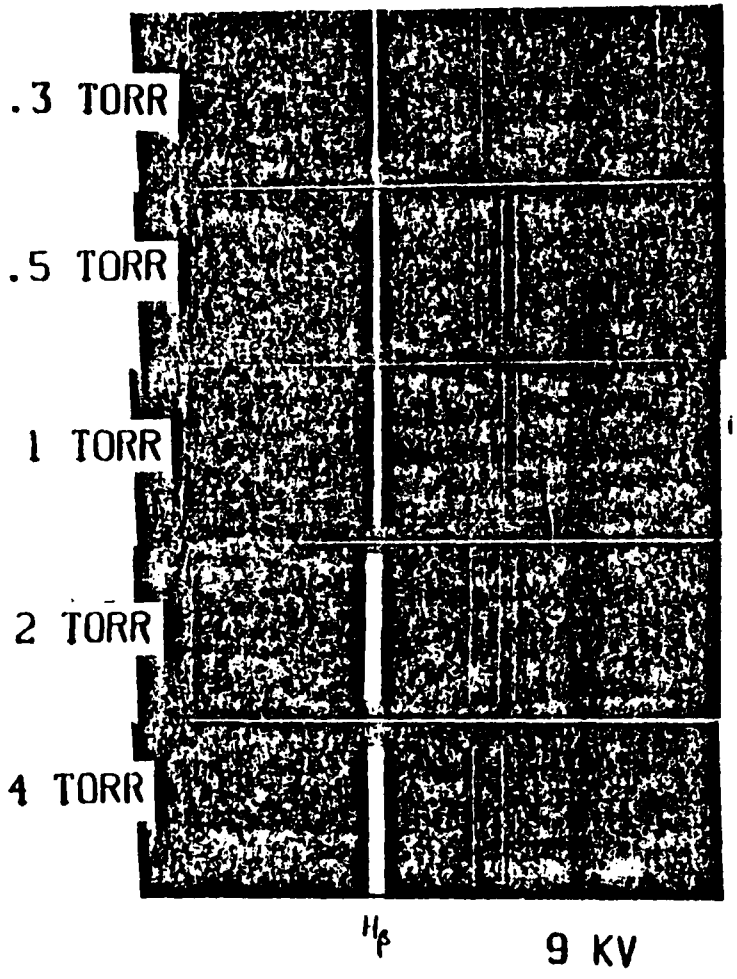

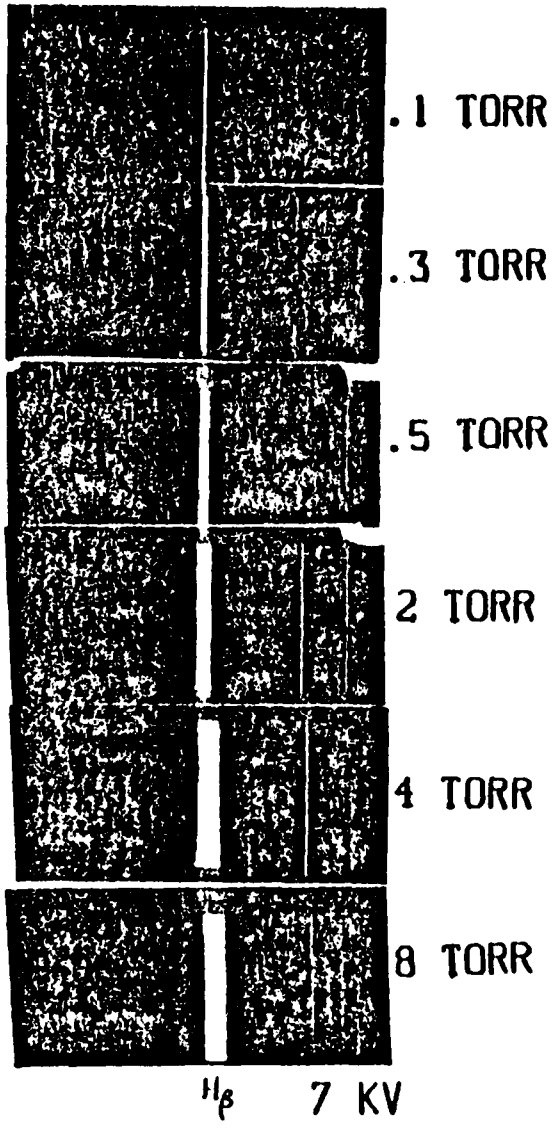

Figure II.4(a). 4 Torr (Prefilled); 9KV Charge at Gun; 50 Micro Slit at 5000A

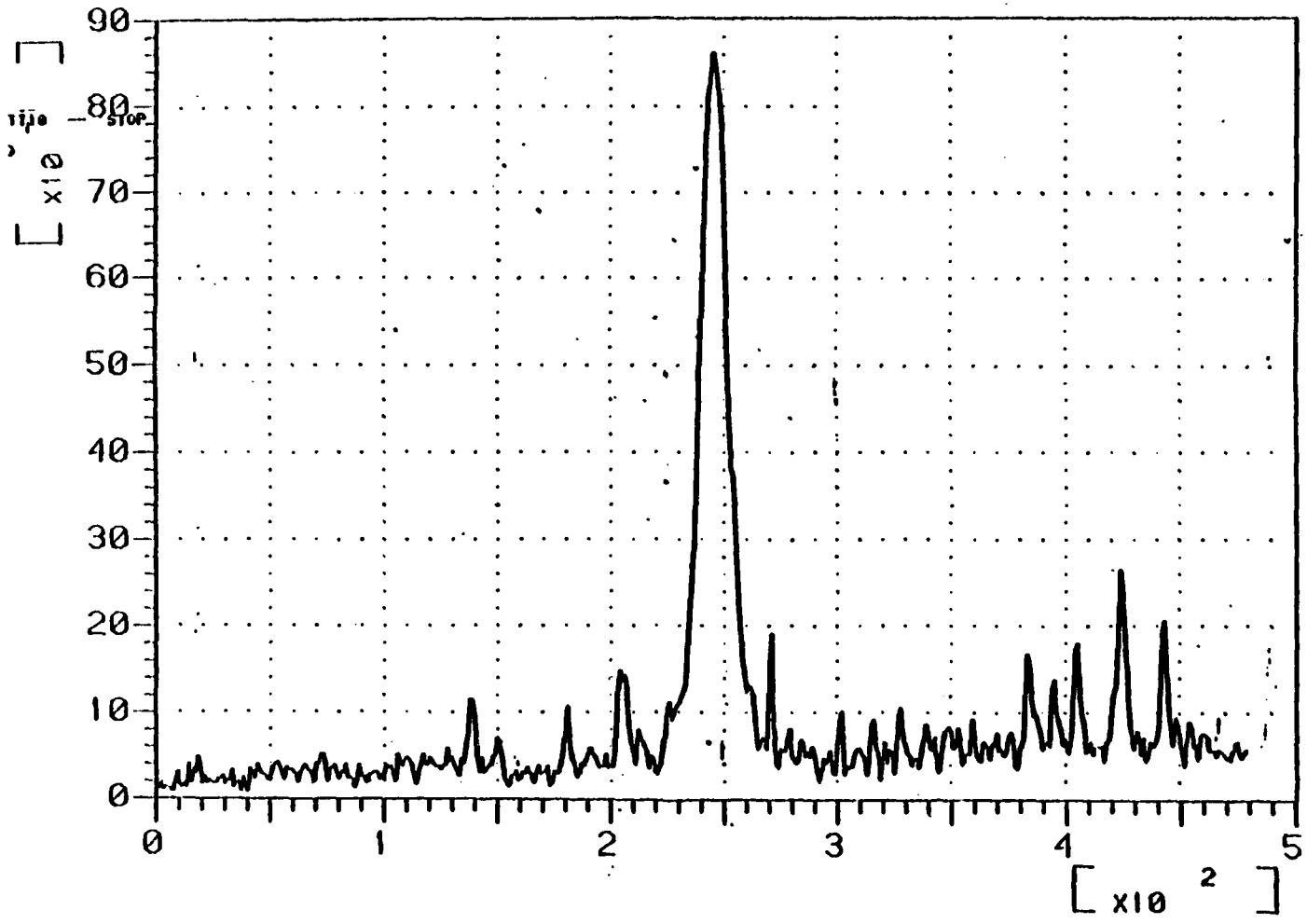

Figure II.4(b). 2 Torr Prefilled

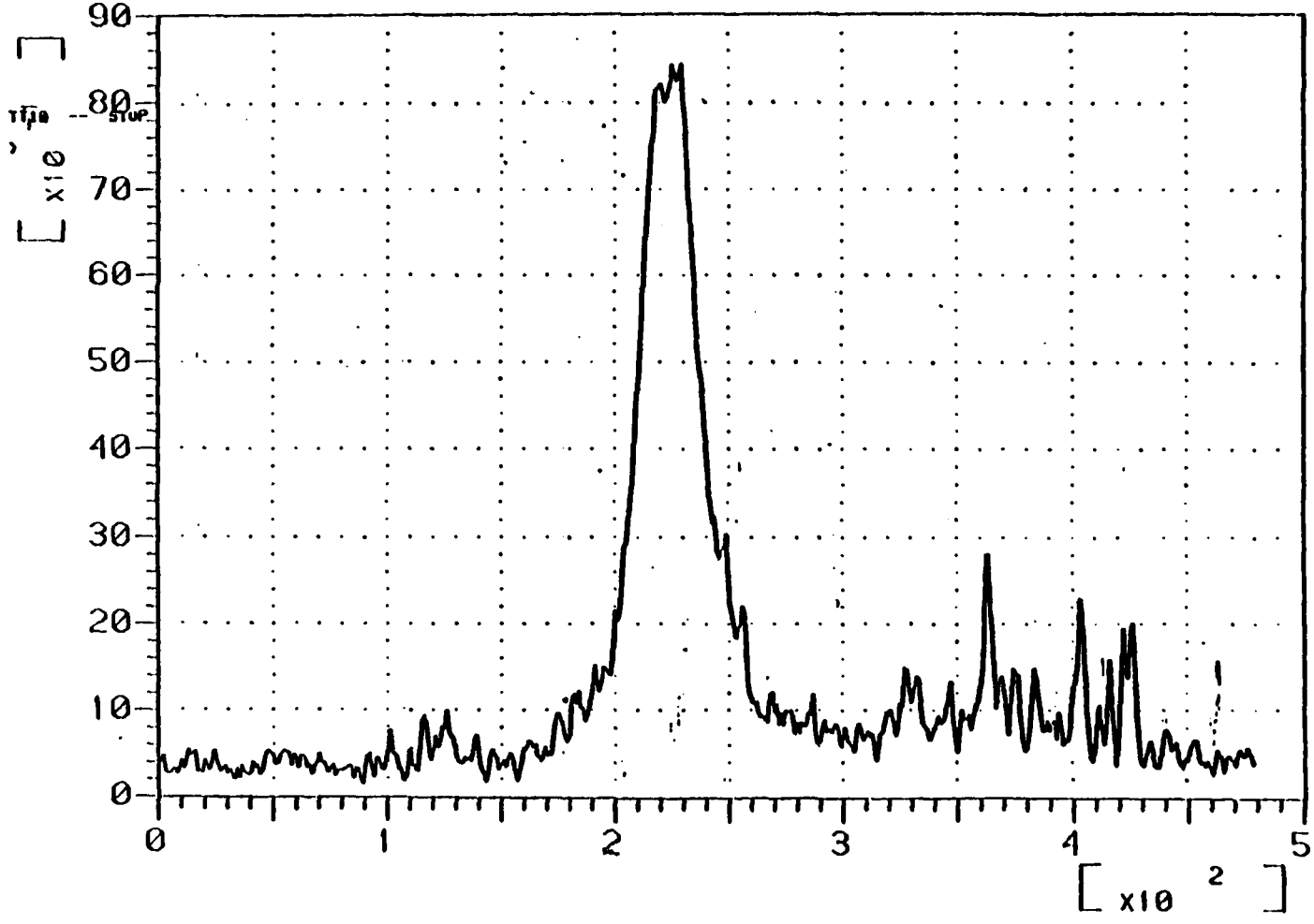

Figure II.4(c) 4 Torr (Prefilled)

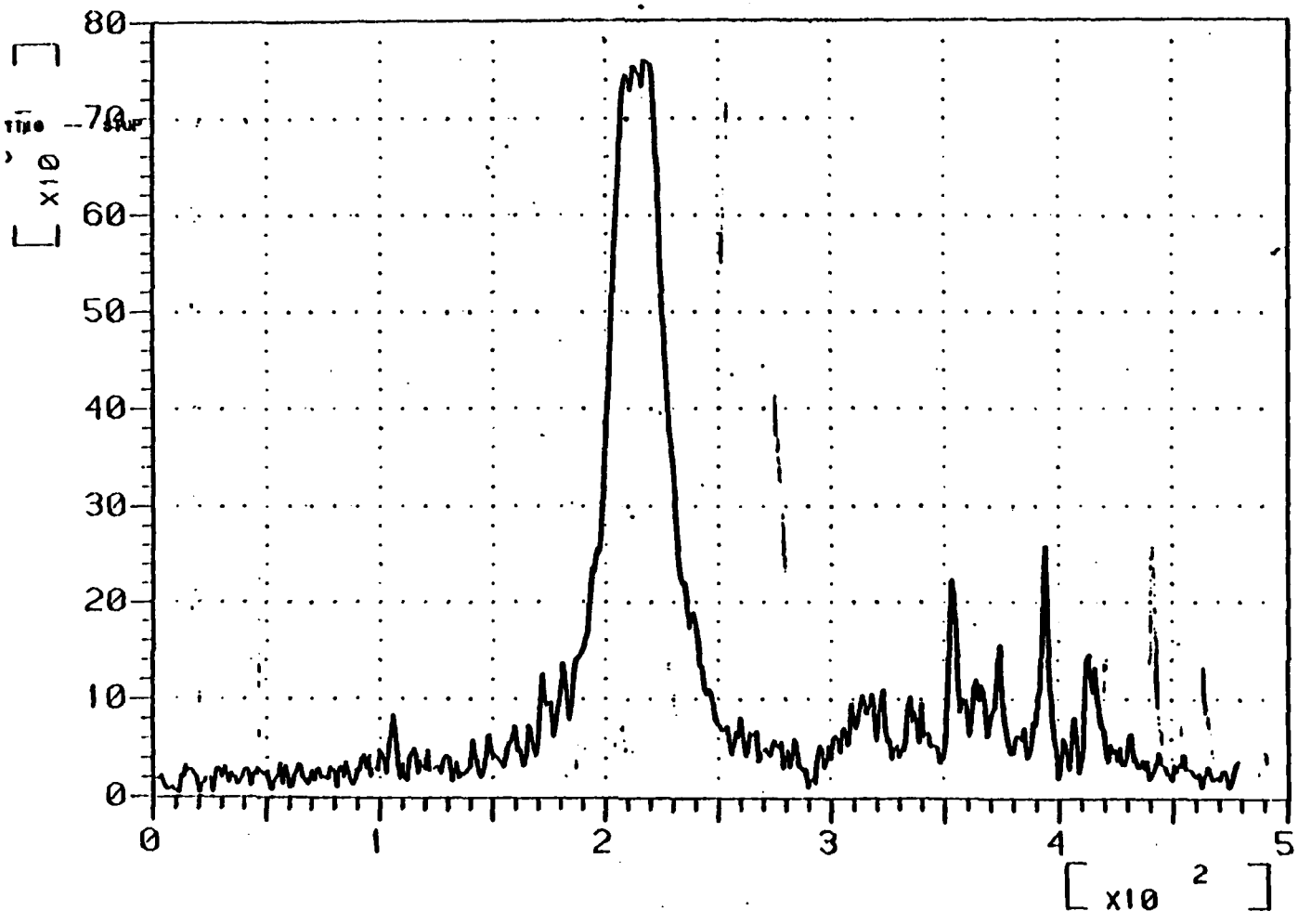

Table II.1

Measured Versus Computed Plasma Density
as a Function of Prefill Gas Pressures

Pressure (torr)	Measured Plasma Density (cm^{-3})	Computed Gas Number Density (cm^{-3})	Percentage of Ionization
0.1	6.0×10^{15}	6.0×10^{15}	100
0.3	1.8×10^{16}	1.8×10^{16}	100
0.5	3.0×10^{16}	3.0×10^{16}	100
1.0	5.6×10^{16}	6.0×10^{16}	93
2.0	7.6×10^{16}	1.2×10^{17}	57.5
4.0	1.3×10^{17}	2.4×10^{17}	50
8.0	1.3×10^{17}	4.7×10^{17}	23

Note: Plasma gun being operated at 7 kV.

b. Puffed mode.

In this mode of operation, the puff valve (which is backed by a hydrogen gas plenum at 20 psi) is first fired, then at a pre-selected time the gun bank is fired. With the puff-valve capacitor charged to 1 kV, the final pressure in the gun chamber is around 2 torr. Figure II.5 shows the spectra obtained at different delay times (the gun being fired at 7 kV). Densities calculated are shown in the graph in Figure II.5. Note the transition which occurs in the data with delay time. The early time firing corresponds to the deflagration case, while the late time corresponds to the pre-fill case (since the gas fills the gun cylinder prior to gun discharge).

2. Injection into an External Magnetic Field

Plasma injection into an external magnetic field of up to 30 kG was examined in the prefilled mode. The stainless steel drift tube was replaced by a plastic (Lexan) one to enable measurement of the B-dot signal corresponding to plasma arrival. The original quartz insulator in the gun was replaced by a polycarbonate (Lexan) insulator, due to delay in acquiring quartz replacements. Visible line spectra obtained are shown in Figure II.6. It can be seen that the Lexan insulator has introduced copious amounts of impurities into the plasma. As the magnetic field increases, the H_β linewidth decreases, indicating that the plasma which penetrates the field has lower density. It can also be seen that at high voltages, the linewidths are larger. Thus a more energetic plasma penetrates more easily into the B-field, as expected. For further work we have gone to a 20 kV gun which can operate at higher densities and higher total energies.

3. Framing and Streak Photography

Some framing and streak photographs were taken with a TRW image-converter camera. A quartz target was introduced into the

Figure II.5. Puffed Operation

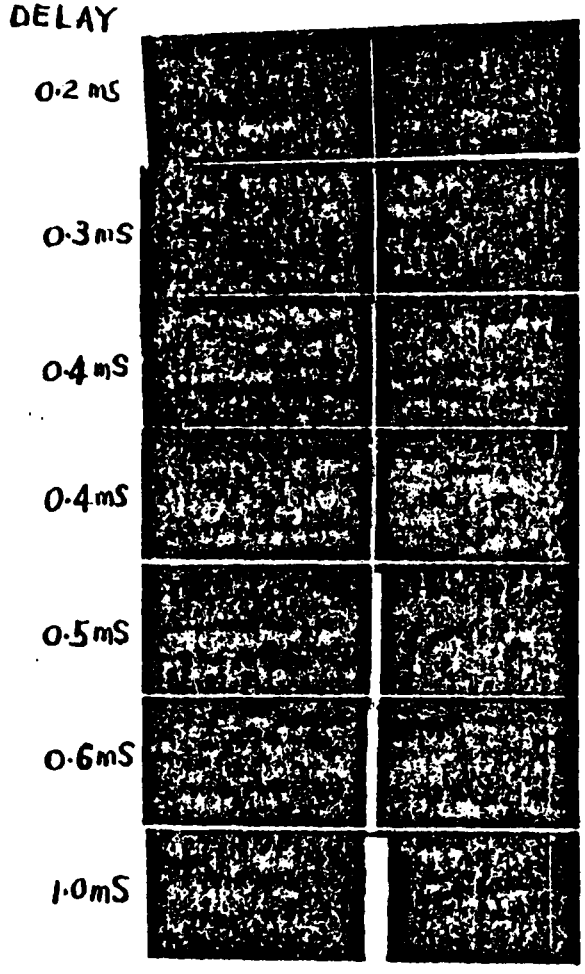

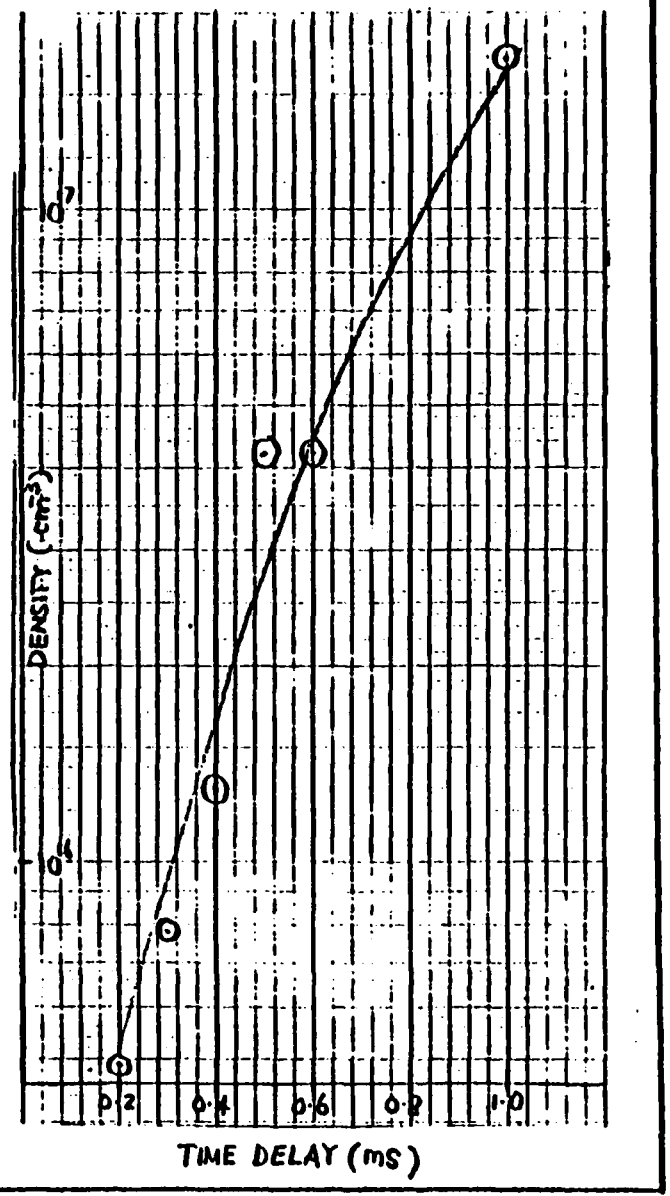

Figure II.6. Prefill Data

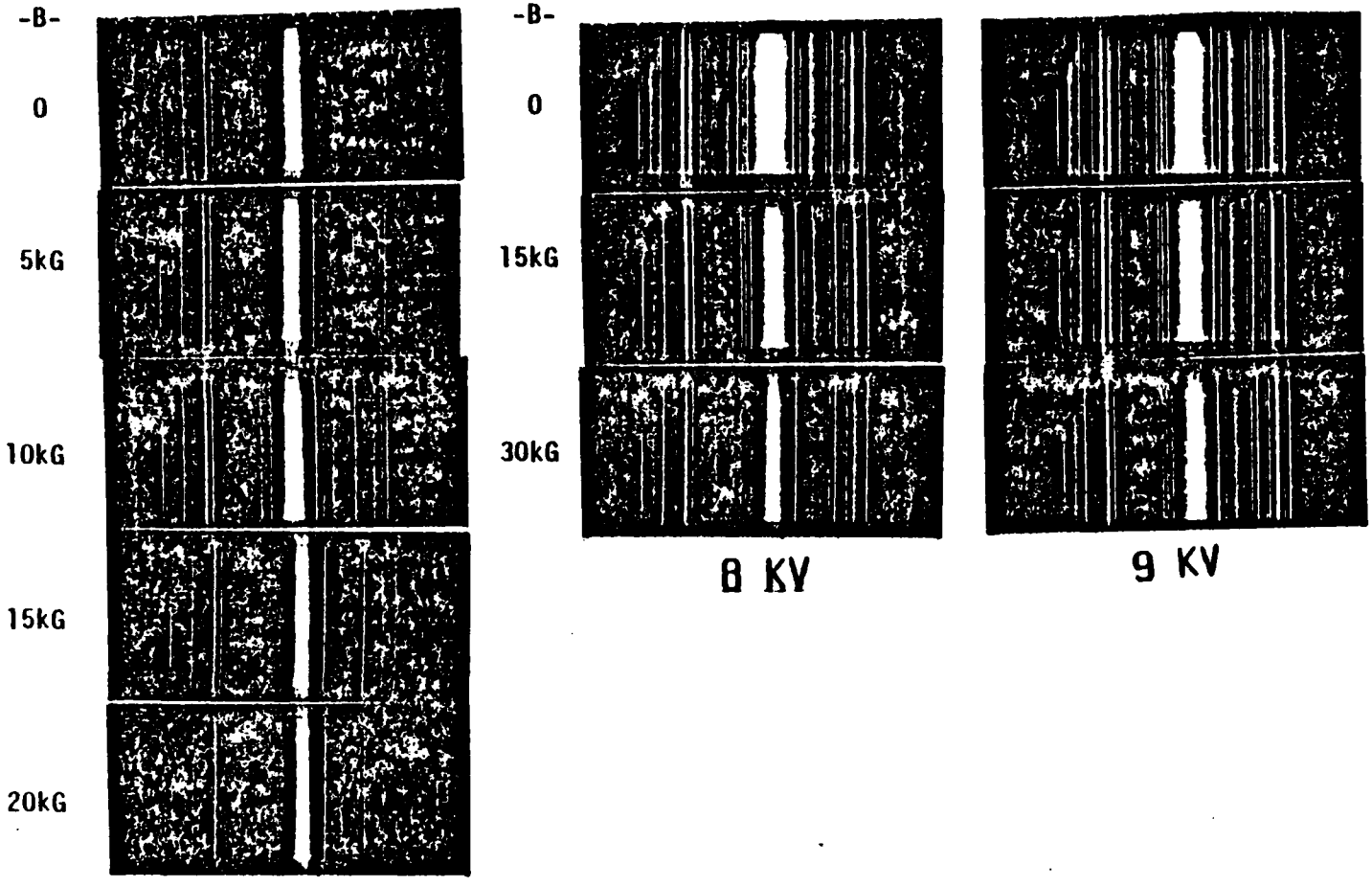

window region of the drift-tube as shown in Figure II.7. This provided a target for the plasma, and the resulting scintillation of the quartz was observed by the camera. Preliminary results are shown in Figures II.8, II.9, and II.10. A black mask covered the view-port except for a horizontal slit, and the camera streaked the image normal to that slit. As a result of placing the quartz target diagonally in the chamber (Figure II.7), the streak picture shows a different time of arrival of the plasma across the image. These preliminary results show that the plasma is relatively uniform, except for a possible m=0 oscillation.

4. B-Dot Loop Measurements

Only a limited number of B-dot measurements were recorded for this bank configuration. Some results are shown in Figure II.11. From the signals recorded, it is quite clear that as the plasma enters the region it excludes the field. However, while traversing the magnetic field region, the field is able to diffuse into and is frozen into the plasma. When the plasma leaves the magnetic field region it drags some field inwards (indicated by the positive spike in signal 5 in Figure II.11). Analysis of this data allows a measurement of plasma conductivity, hence temperature, in the field region. However, since the field diffusion problem is non-linear, a detailed understanding of the plasma behavior would require an MHD code simulation of the experiment. Such a code has not been available for the geometry of the experiment; therefore no further conclusions have been drawn.

B. Plasma Sheath Behavior

In order to understand the focal properties of the plasma source which we have been using, we undertook measurement of the plasma sheath characteristics inside the cylindrical barrel of the gun. This entailed inserting a row of axially and azimuthally spaced B-dot probes through the outer electrode of the

Figure II.7. Fast Photography

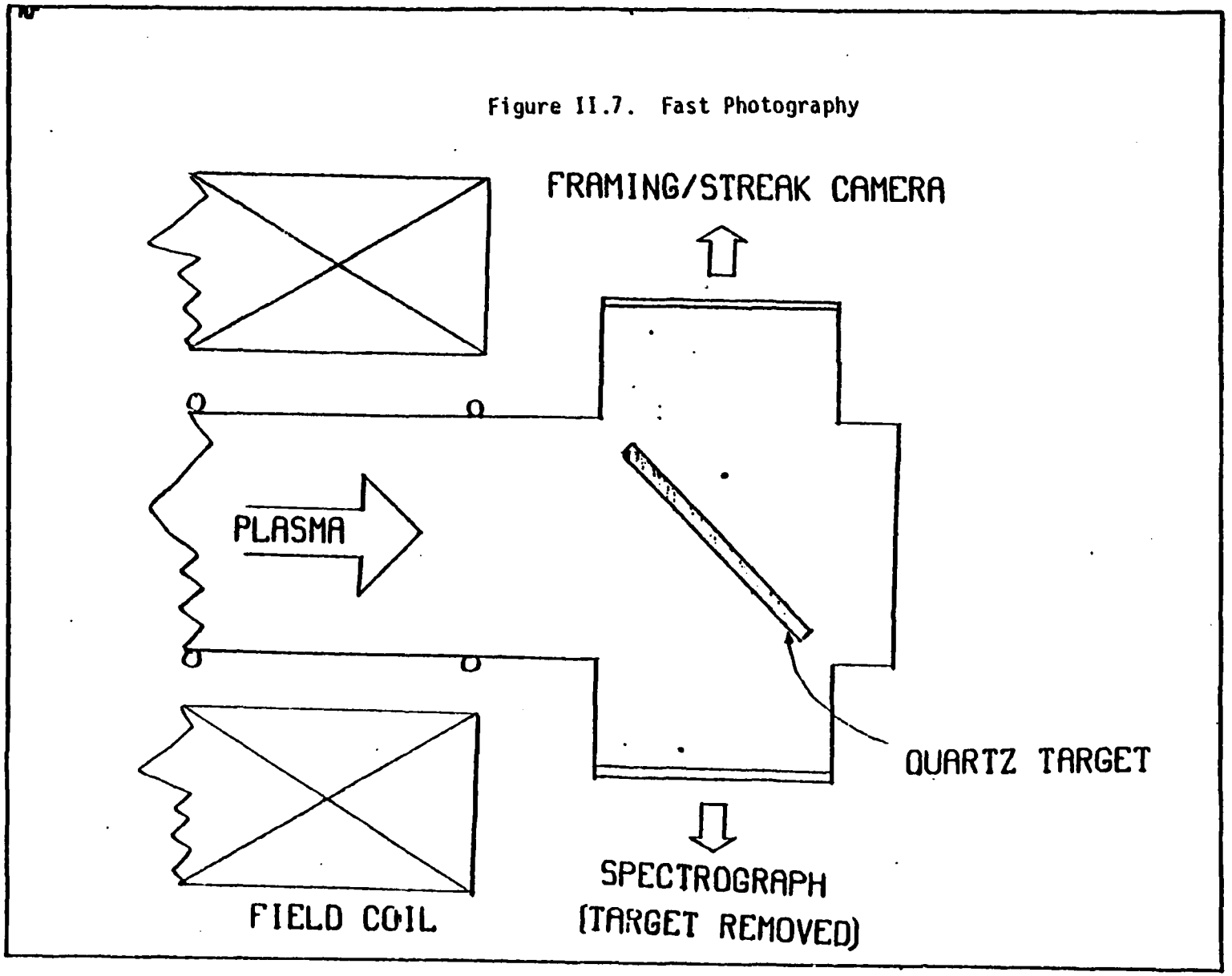

Figure II.8. Streak Photographs

SET - UP

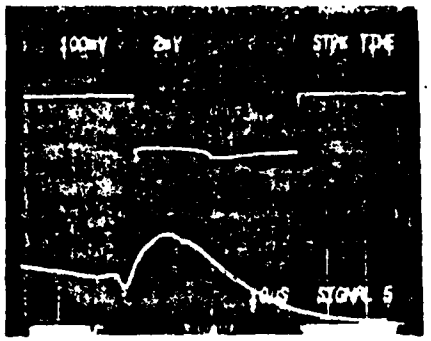

ND 1·3

SLIT

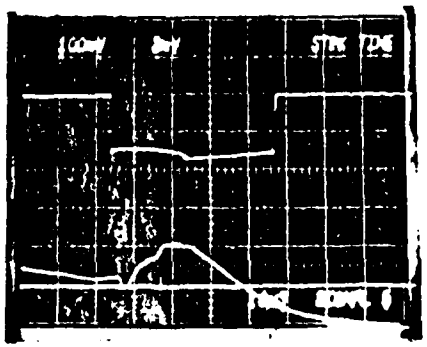

ND1·3

Figure II.9. Streak Photographs.

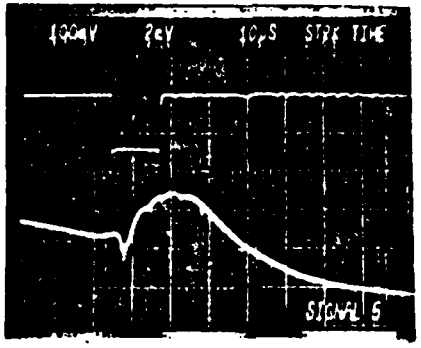

ND1·0

ND 0·3

Figure II.10. Framing Photographs

SET - UP

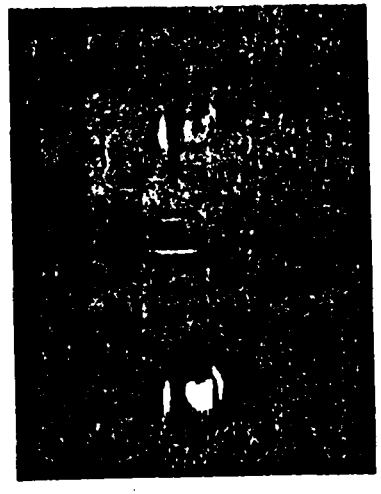

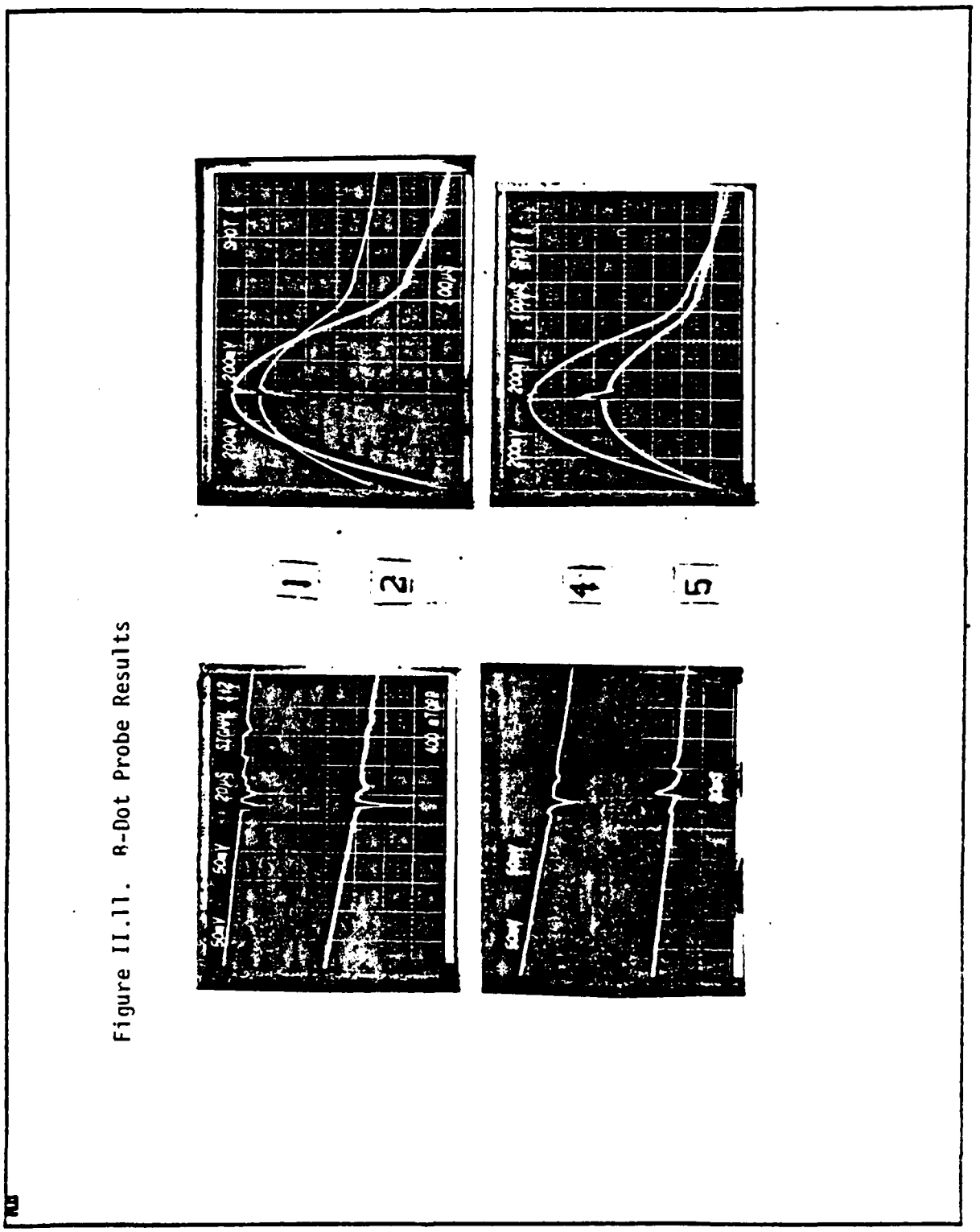

Figure II.11. B-Dot Probe Results

plasma gun. We mapped the plasma current density in the gun as a function of a number of the operational parameters of the gun system. We mapped out the regime of operation which has been characterized as "deflagration" behavior, versus behavior labelled at "snowplow." The gun used for these studies is shown in Figure II.12.

In this series of measurements, the gun is driven by a capacitor bank of 15 to 45 μF at ±18 kV through a single spark gap switch. The total gun current is between 75 and 150 kA. Since the electromechanical puff valve is used in this case, the time delay between the arrival of the gas at the position of the timing spark plug and the triggering of the main capacitor bank is varied from a few tens of microseconds to a few milliseconds.

In order to study the current sheath dynamics and the distribution of current within the coaxial electrodes, it is necessary to measure the time-varying magnetic field distribution within the gun. As with many other gaseous discharge experiments, reproducibility is a major problem. This is especially so in the deflagration mode of operation where the intrinsic time delay (jitter) in the gun may be quite large. To avoid this complication in the data, each set of measurements is collected in one single shot. The spatial resolution is limited by the number of available data recording channels (i.e., the number of oscilloscopes). For the present measurements, only seven channels are devoted to the B-field measurement. An additional channel is used for the Rogowski coil for monitoring the total gun current. For most shots, an open shutter picture of the interior of the plasma gun is also taken.

The probes used for mapping the magnetic field are 4-turn B-dot probes. A description of the probes, their construction

Figure II.12

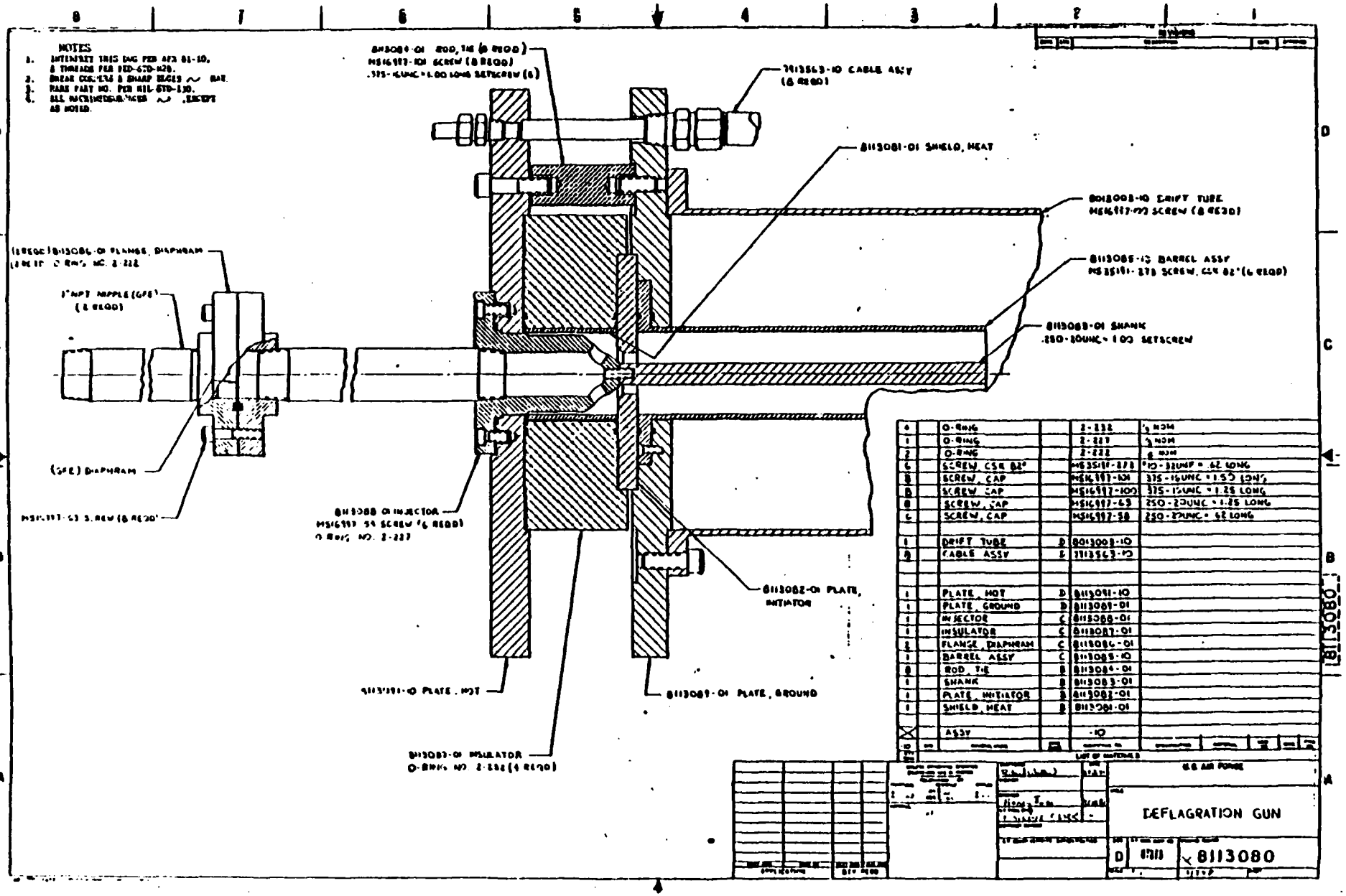
NOTES
8113081-01 SHIELD, HEAT
8113085-10 BARREL ASSY
8113083-01 SHANK
.250-20UNC-1.00 SETSCREW
8113082-01 PLATE, INITIATOR
8113088-01 INJECTOR
8113087-01 INSULATOR
8113084-01 ROD, TIE
8113086-01 FLANGE, DIAPHRAGM
8113091-10 PLATE, HOT
8113089-01 PLATE, GROUND
O-RING NO. 2-232
O-RING NO. 2-227
O-RING NO. 2-222
SCREW, CAP
SCREW, CAP
SCREW, CAP
SCREW, CAP
SCREW, CAP
DRIFT TUBE
CABLE ASSY
PLATE, HOT
PLATE, GROUND
INJECTOR
INSULATOR
FLANGE, DIAPHRAGM
BARREL ASSY
ROD, TIE
SHANK
PLATE, INITIATOR
SHIELD, HEAT
ASSY
DEFLAGRATION GUN
8113080

and calibration is presented in an appendix at the end of this section. The probes are installed 2 cm from one another, with the first probe at 4 cm from the insulator at the breech of the gun. Ten probes can be installed in each row covering almost the entire length of the electrode, but only seven are monitored. In some shots, probes at the same axial position but different θ-positions are monitored to check the symmetry of the current sheath.

The open shutter pictures show that the discharge in the plasma gun is very prone to spoke formation at small time delays. Since open shutter photographs are time integrated, they do not furnish any information on the time history on the plasma. As such, we do not have any knowledge on when the spokes are formed. Furthermore, if the spokes are rotating, then the time integrated photographs will only show a uniform illumination. The signals recorded by the B-dot probes however, do not differ much for shots with or without spokes. Thus it is possible that such spoking occurs late in time (after the first half cycle).

The main objective of this section is to measure the magnetic field distribution axially and to use these measurements to study the behavior of the plasma current sheath within the gun under different operating conditions. In order to meaningfully compare and correlate the signals recorded by probes at different axial positions, it is absolutely necessary to have a common time fiducial mark on each oscilloscope trace. All the oscillograms are set to a common time scale, with reference to the time fiducial mark. Once this is done, the traces can be overlayed on the same graph to display the time of arrival at each probe position. The data will then provide the basis for analysing the plasma current sheath within the coaxial electrodes during the discharge. Measurements have been done for both hydrogen and

argon gas puffs. Each series of measurements consists of a number of shots taken with a different time delay between puffing in the gas and firing of the plasma gun. A typical set of data is presented in Figures II.13(a-d). As mentioned earlier, some data has been collected for shots in which some probes are mounted in different θ-positions but on the same Z-position to provide a symmetry check on the current sheath. One such series of measurement is displayed in Figures II.14(a-e). Each graph in these figures is an overlay of eight traces obtained from one single shot. The first trace (without symbols) is the total current flowing through the plasma gun, as measured by a Rogowski coil located in between the two end plates of the gun. The remaining seven traces are integrated B_θ-dot signals. (Note that these B_θ signals are normalized to units of amperes, with a normalizing factor of $\frac{2\pi r}{\mu_o}$.)

In Figures II.14(a-e), the B-dot probes monitored are designated as B1, B2, B3, B4, B7, B7 and B7, which are respectively 4, 6, 8, 10, 16, 16 and 16 cm from the breech of the plasma gun. The three B7 probes are at the same axial position, but are mounted at θ-positions differing by π/2 from each other. In addition to providing a symmetry check, the amplitude and the time of arrival of these three signals can also be used to confirm the proper calibration of our data acquisition equipment.

At long delay times (Figures II.14(a) and (b), the magnetic signal recorded by each probe has a very steep rise, which is typical of the well known snowplow mode of operation (see, for instance, ref. 8 and 9). This implies that the current sheath is very thin and it moves from the breech towards the muzzle at an approximately uniform speed. The amplitudes and time of the traces show good consistency, an indication that our data acquisition and calibration procedure has indeed been carried out

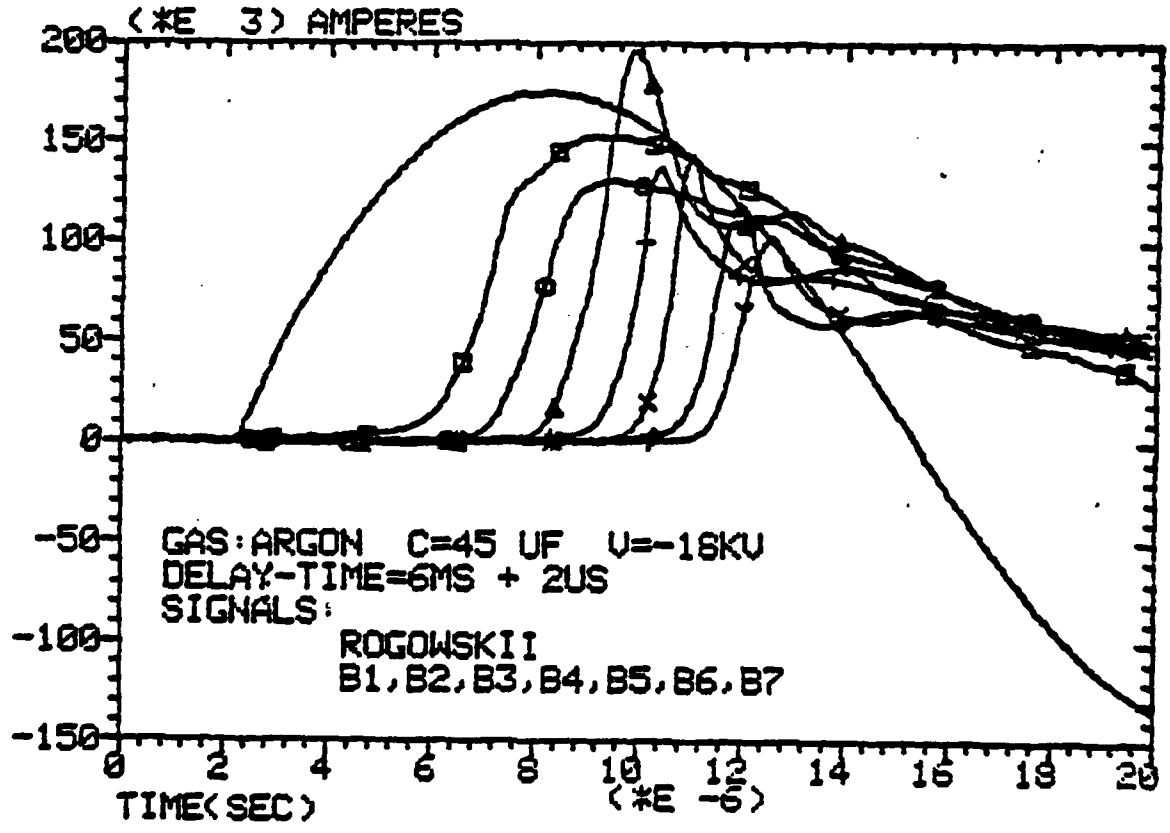

Figure II.13(a)

Current and B_θ Traces.
Shot #7058306: Delay Time = 6.0 ms.

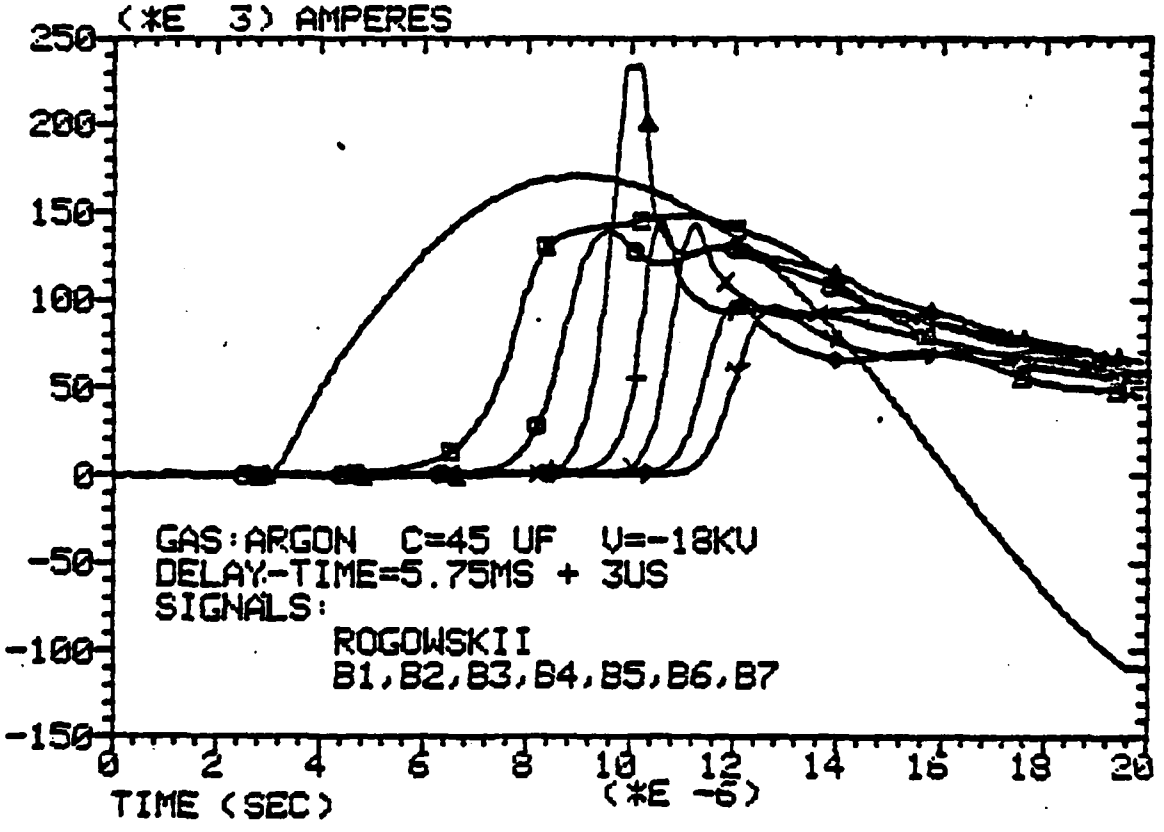

Figure II.13(b)

Current and B_θ Traces.
Shot #7058308: Delay Time = 5.75 ms.

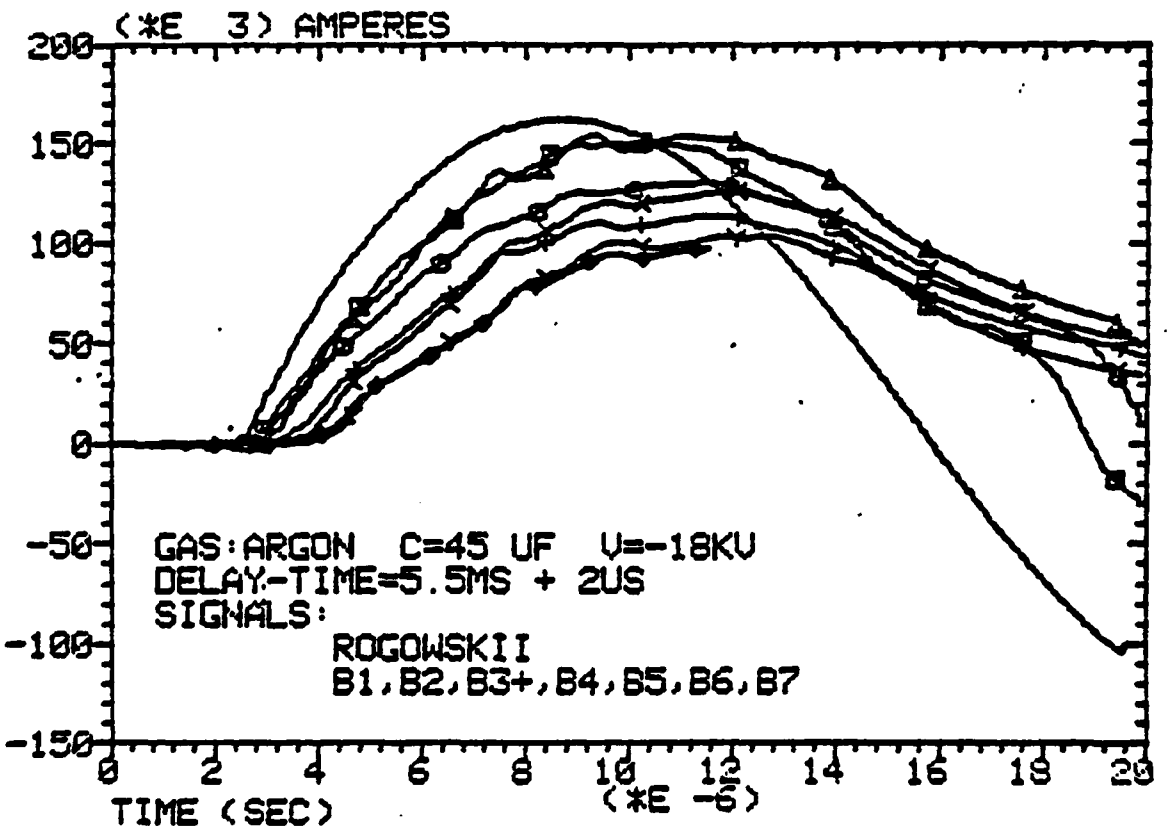

Figure II.13(c)

Current and B_θ Traces.
Shot #7058307: Delay Time = 5.5 ms.

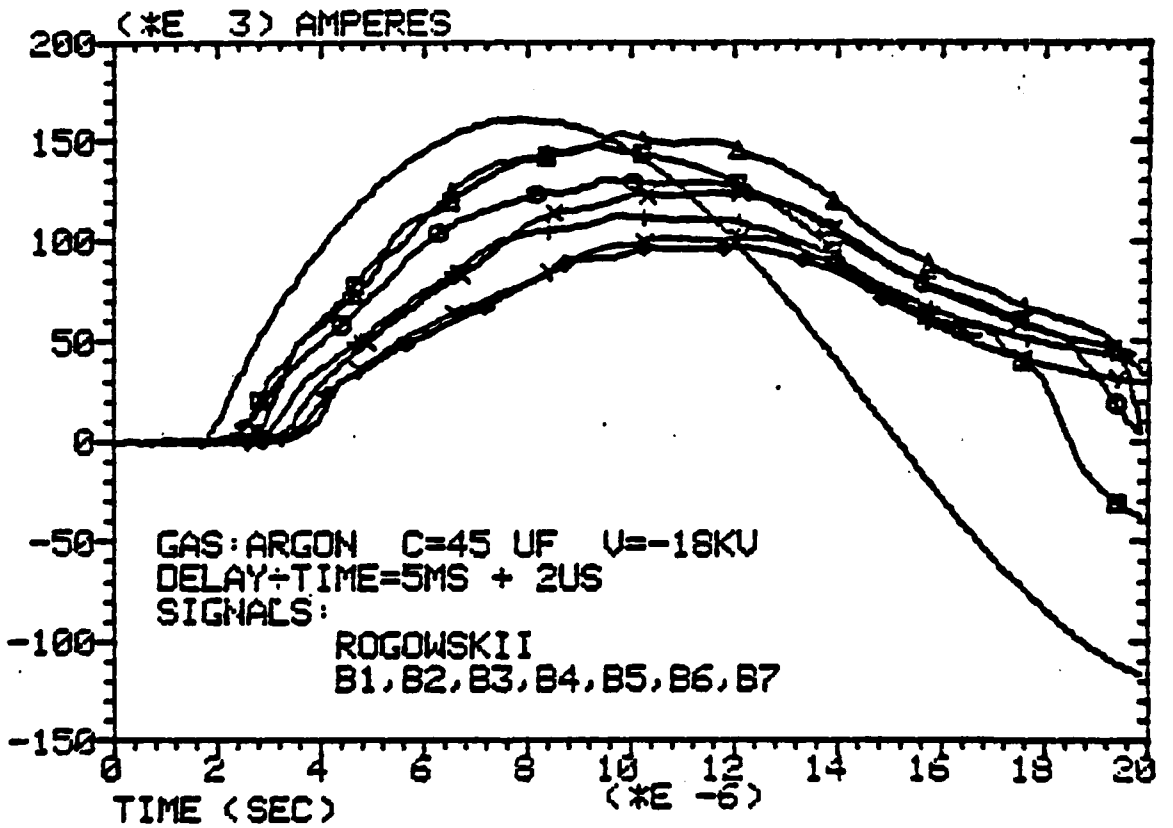

Figure II.13(d)

Current and B_θ Traces.
Shot #7058305: Delay Time = 5.0 ms.

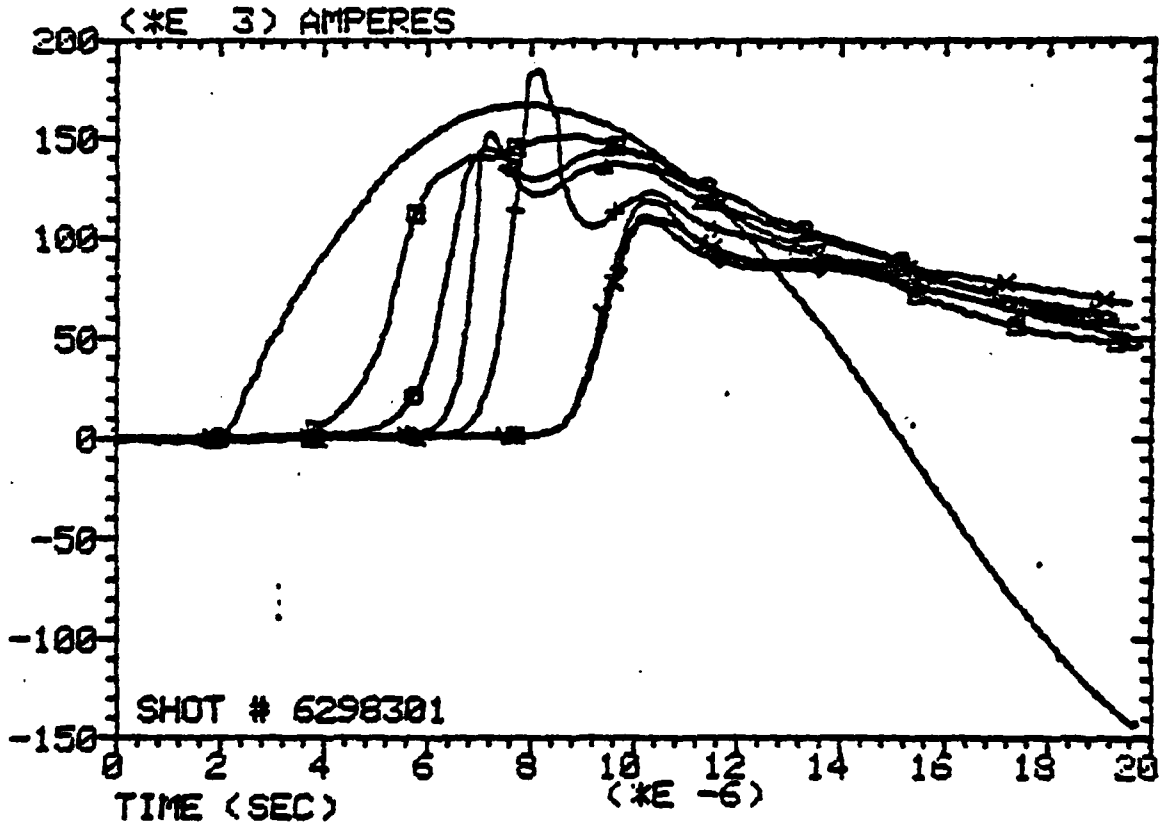

Figure II.14(a)

Current and B_θ Traces.
Shot #6298301: Delay Time = 10.0 ms.

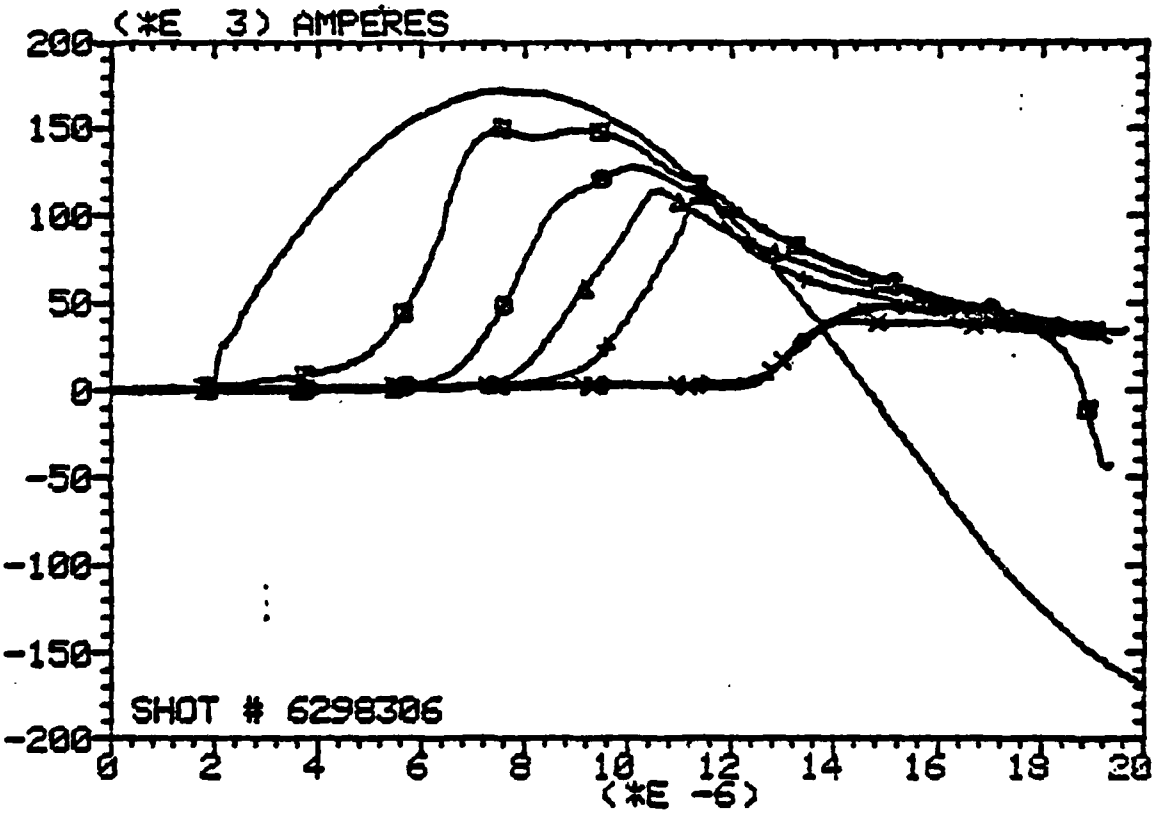

Figure II.14(b)

Current and B_θ Traces.
Shot #6298306: Delay Time = 3.0 ms.

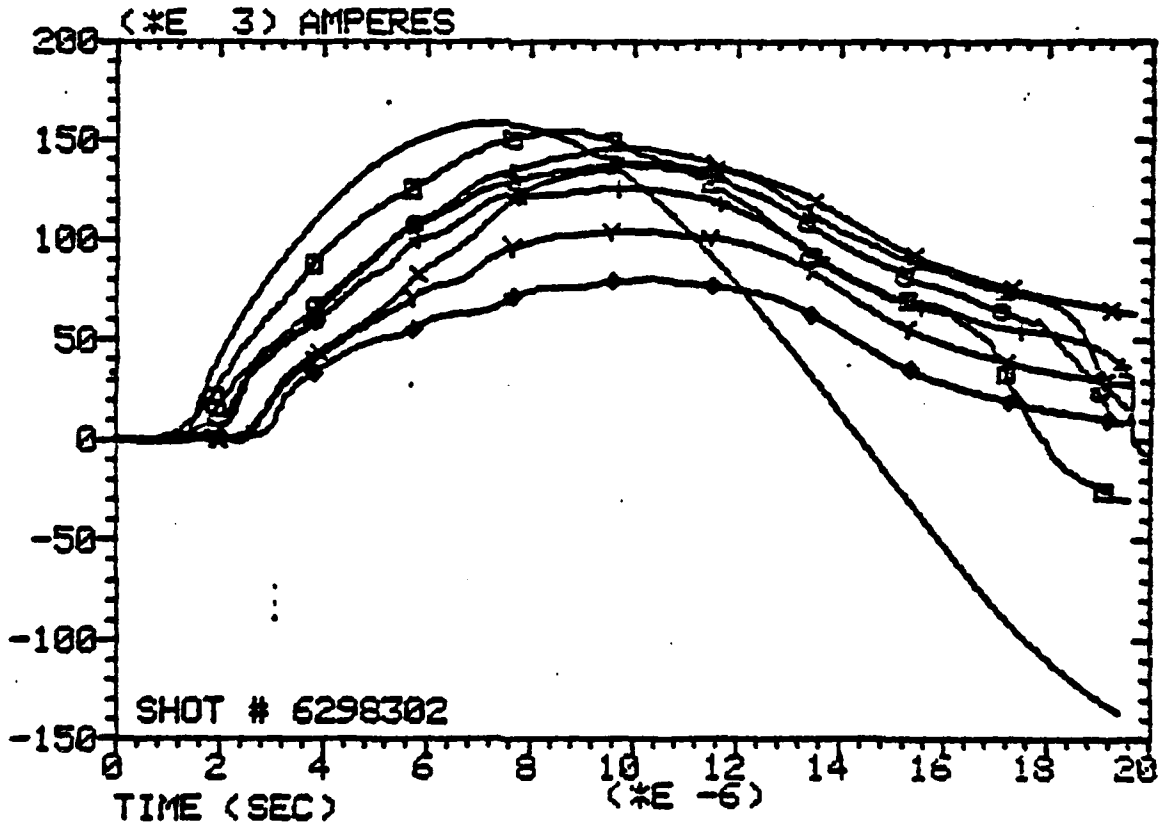

Figure II.14(c)

Current and B_θ Traces.
Shot #6298302: Delay Time = 2.0 ms.

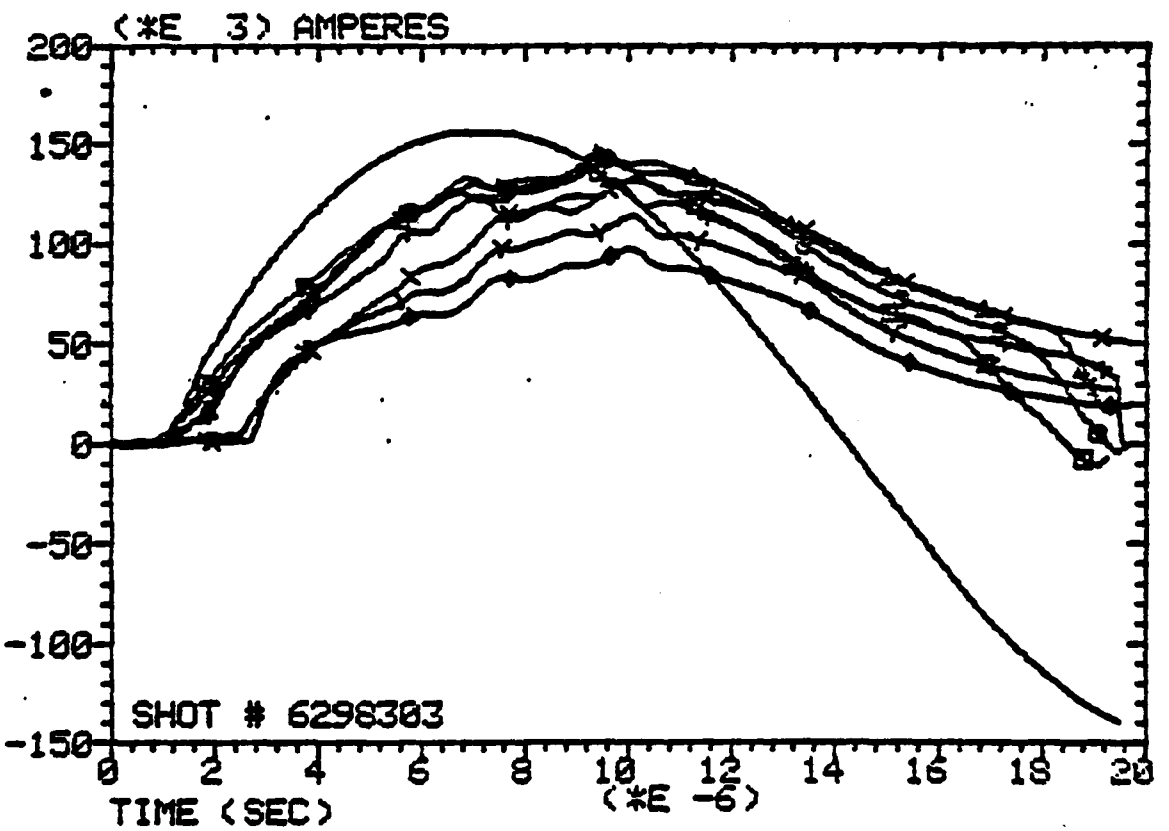

Figure II.(14d)

Current and B_θ Traces.
Shot #6298303: Delay Time = 1.0 ms.

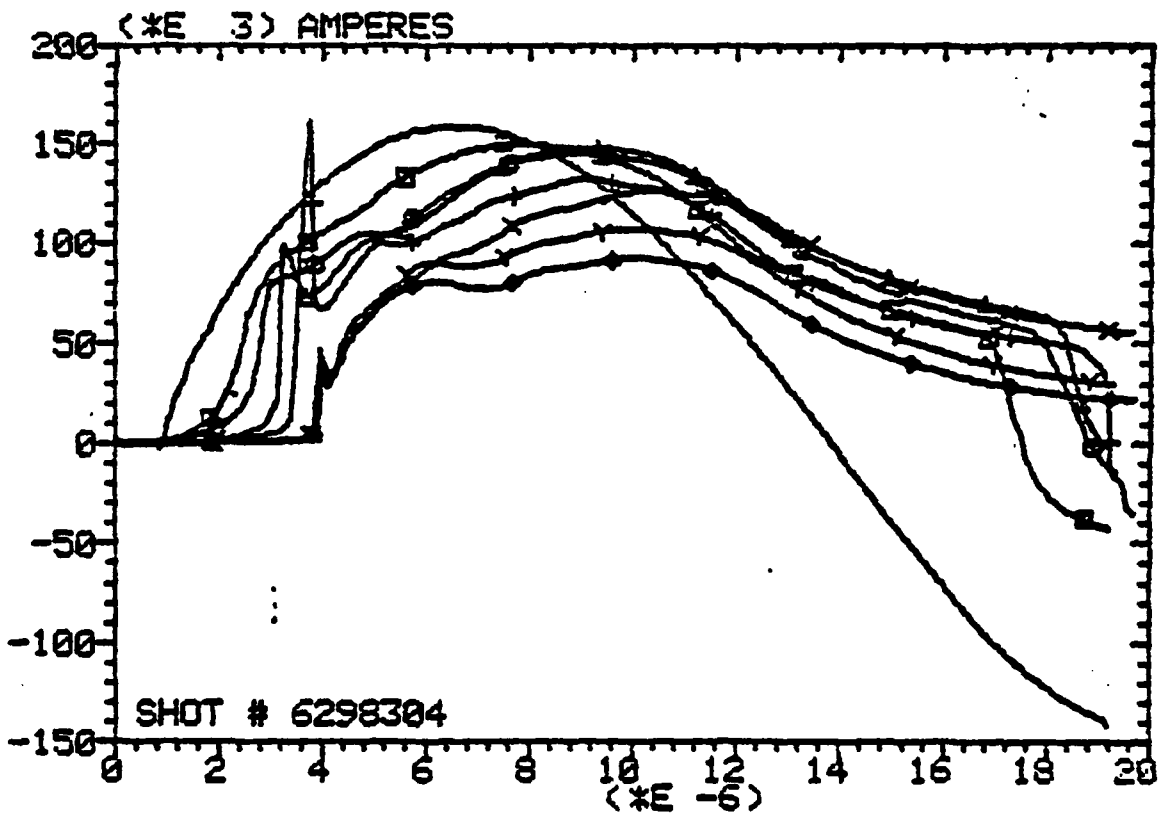

Figure II. (14e)

Current and B_θ Traces.
Shot #6298304: Delay Time = 0.5 ms.

correctly. For these long delay shots, the magnetic field profiles seem to be very symmetric. As the time delay is shortened, one gets into a regime where the operation fo the plasma gun is not well understood, namely, the transition region and the deflagration mode.

At short delays, the magnetic signals rise very gently implying that the plasma gun is operating in a mode which is different from the snowplow mode observed in the long-delay cases. This is the so-called deflagration mode of operation. In this mode, the discharge quickly distributes itself across the entire length of the electrodes, thus each probe picks up the magnetic signal very early in time after the current starts flowing in the system. This speed at which the discharge distributes itself within the gun should not be confused with that of the current sheath speed as in the snowplow case. In the snowplow operation, the speed measured by the time of arrival of the magnetic signal at each probe is equal to the speed of the plasma and the speed of the current sheath which is the carrier of the plasma. On the other hand, the situation is completely different in the deflagration mode. For this case, the speed of the magnetic front as measured by the probes is equal to the speed of the plasma, but is not equal to the speed of the current sheath. In fact, as will be shown later, the current sheath in this case becomes somewhat stationary inside the coaxial electrodes. The three B7 signals show that the current distribution is not as symmetric as in the snowplow mode. These three signals start at about the same time with comparable magnitude initially, but later grow to different amplitudes. The order of the signal size of the three signals is preserved from shot to shot, but the absolute values vary. This may be due to some preferred discharge spots within the gun barrel or interaction of the plasma with the probes (such as probe ablation). The transition from

snowplow to deflatration is neither a well-defined nor a smooth one. The only shot in the series of data presented here whose data shows the characteristics of both the snowplow and the deflagration modes is the one depicted in Figure II.14(e). In this shot, the data shows that the gun starts off in the snowplow mode, but quickly changes into the deflagration mode of operation.

In Figures II.13(a-d), and most other sets of measurement, the B-dot probes monitored are those designated B1, B2, B3, B4, B5, B6 and B7, which are respectively 4, 6, 10, 12, 14, and 16 cm from the insulator at the breech of the gun. The delay time for the set of data presented in Figures II.13(a-d) has been set relatively long. Nevertheless, both modes of operations have been observed. This implies that the time delay is not the only factor dictating whether or not the gun will operate in which of the two modes. The data presented here is for argon, but similar phenomenon has been observed for hydrogen. Other factors such as the initial gas distribution, gas flow velocity and the path of the initial discharge may be of great importance in determining the mode of operation of the plasma gun.

The Snowplow Mode

This mode of operation is normally accomplished by prefilling the vacuum chamber with the propellant gas to a uniform pressure before discharging the capacitor bank through the gun. In the case of a puff system, a long delay time (long enough for the gas to fill up the entire gun barrel) will result in a situation similar to the snowplow case.

During the snowplow mode of operation, the barrel is uniformly filled with gas when the capacitor bank is fired, therefore the preferred path for the initial discharge to occur is through the minimunm inductance path which is on the surface of the breech insulator. There is usually a time lapse between

the onset of current and the lift off of the current sheath from the surface of the insulator. For the snowplow shots in Figures II.13(a) and (b), at the time lapse between the onset of current flow in the system and the arrival of the sheath at the first probe B1 (4 cm from the breech) is about 3.5 μs. Since the only preferred path for the initiation of the discharge is on or near the surface of the insulator, the snowplow mode tends to be the most reproducible mode of operation.

By measuring the time of arrival of the signal at the various B-dot probe positions, the speed of the current sheath can be easily computed. In the case of an argon puff, the average snowplow velocity ranges from 2 to 5 cm μs^{-1}. The velocity for hydrogen puffs is somewhat higher; it ranges from 5 to 15 cm μs^{-1}. The velocity of the current sheath and hence the velocity of the plasma is dependent on the amount of gas in the gun and the total initial energy stored in the capacitor bank. A series of static filled discharges has been carried out for hydrogen at different prefilled pressures. The result is presented in Table II.2.

Table II.2

Hydrogen Snowplow Velocity
at 15 μF and 18 kV

Pressure (Torr)	Velocity (cm/μs)
8.0	4.6
6.0	5.0
4.0	5.9
2.0	8.0
1.0	10.3
0.5	14.3

By fitting the data in Table II.2 to a power curve, it was found that the plasma sheath velocity scales as $p^{-0.41}$, where p is the prefilled pressure in the gun. This relation falls between the results obtained by Dattner [9] and Wilcox [10]. Their results predict a scaling law of $p^{-1/3}$ and $p^{-1/2}$, respectively. Wolf, Sorrell and Nakagawa [11] however, found in their computation results that the velocity should scale as $p^{-1/4}$ if the current sheath takes on a parabolic shape, and if they assume a constant inductance for the system, then the velocity scales as $p^{-1/2}$.

The B-dot signal recorded on each oscillogram shows only the evolution of the magnetic field at their respective probe positions in time. The signals from the various axial positions can be combined to give a picture of the distribution of the magnetic field over the entire length spanned by the probes. To do this for any particular time of interest, one just needs to sample the data points from each B-trace corresponding to the same time and plot them against the z-position for each probe. A series of such cross-plots at different time values can be plotted to trace the behavior of the magnetic field distribution in the coaxial plasma gun during the discharge. Each of these plots can then be differentiated to yield the distribution of the current density, J_r, over the entire length of the electrode. To illustrate this mathematically, consider two consecutive probe positions n and (n+1), where the magnetic fields are B_n and B_{n+1} respectively. The currents corresponding to the measured magnetic field strength are:

$$I_n = \frac{2\pi r B_n}{\mu_o}$$

and

$$I_{n+1} = \frac{2\pi r B_{n+1}}{\mu_o}$$

where r is the radial position of the probes (assuming that both are at the same radial position) and μ_o is the magnetic permeability. If the probes are separated by a distance Δz, then the current density at that point is given by

$$J_n(z,t) = \frac{I_{n+1} - I_n}{2\pi r \Delta z} = \frac{B_{n+1} - B_n}{\mu_o \Delta z}$$

or

$$J_n(z,t) = \frac{1}{\mu_o}\left(\frac{\Delta B}{\Delta z}\right)$$

A typical set of data for the snowplow analysed as described above is presented in Figures II.15(a), (b), and (c). Figure II.15(a), similar to the plots presented earlier, shows the seven integrated B-dot signals and the Rogowskii signal overlayed on the same plot. All these traces have been aligned with respect to the common time fiducial mark (not shown) incorporated into each of the signals. It is obvious that there is a rather long time delay between the Rogowskii signal and the first magnetic signal. A possible explanation for this is that when the gun is fired, it has already been uniformly filled to a high pressure (> 10 Torr), so the breakdown threshold of the gas is high, and the lift-off time may be long. Once the current sheath lifts off of the insulator, it has to plow into a dense background; therefore it will be moving slowly. The current sheath remains very well-defined even by the time it reaches probe B7. This is an indication that there are no secondary discharges behind the main current sheath. It can also be observed that the magnetic field

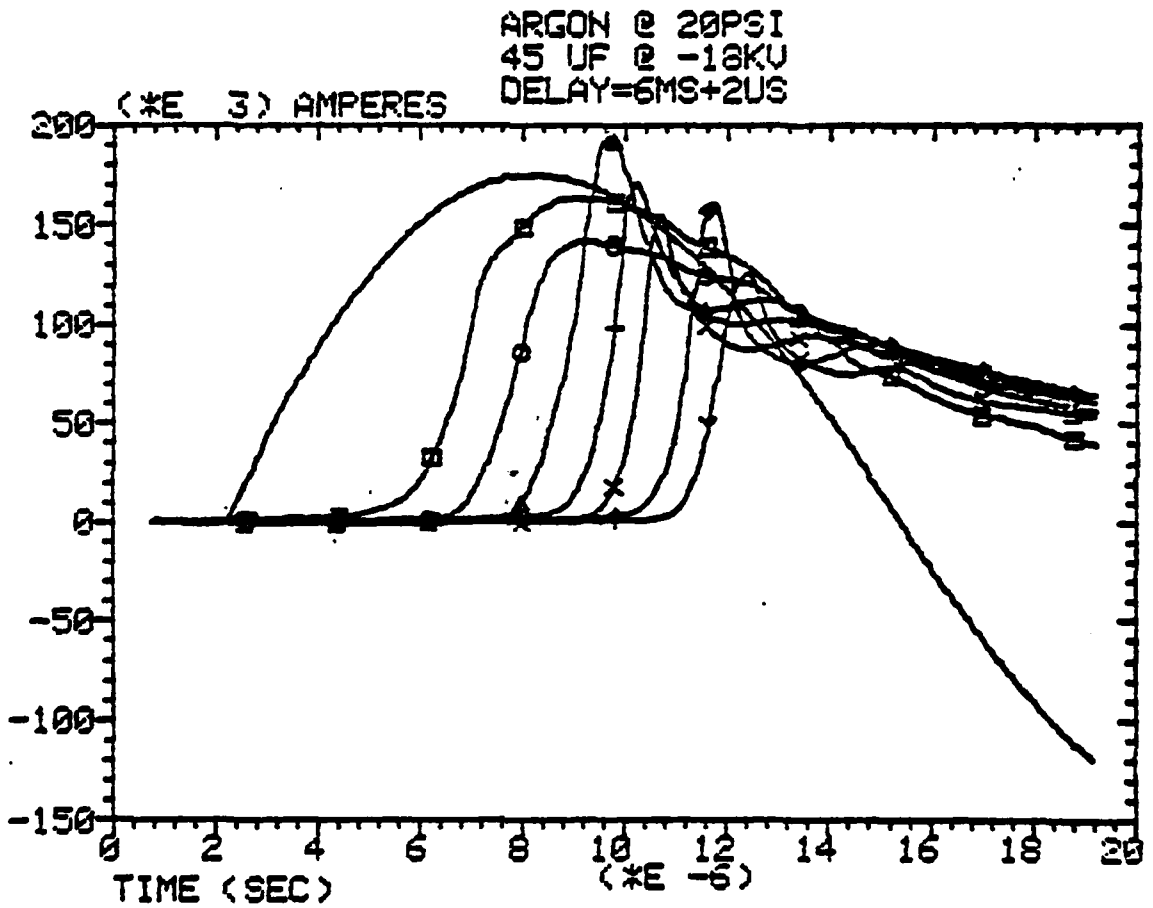

Figure II.15(a)

Current and B Traces for Snowplow

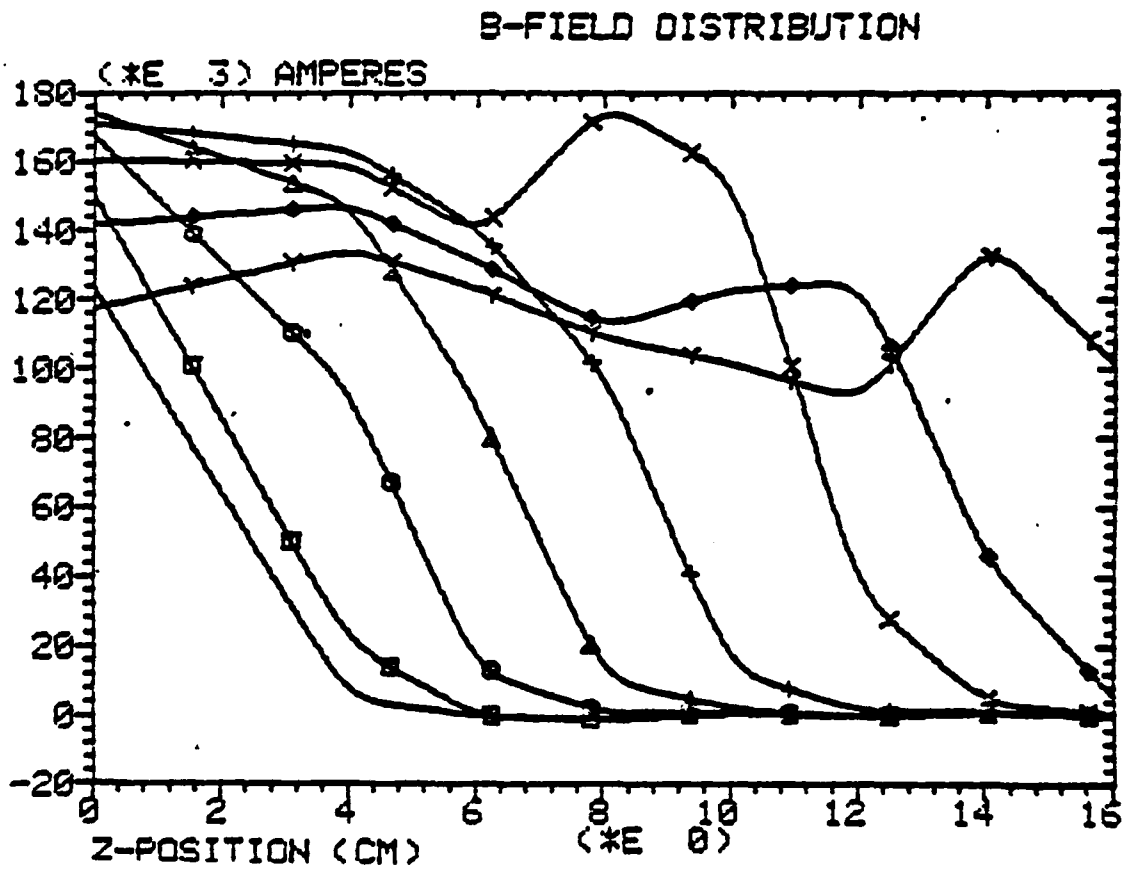

Figure II.15(b)

Magnetic Field Distribution for Snowplow.

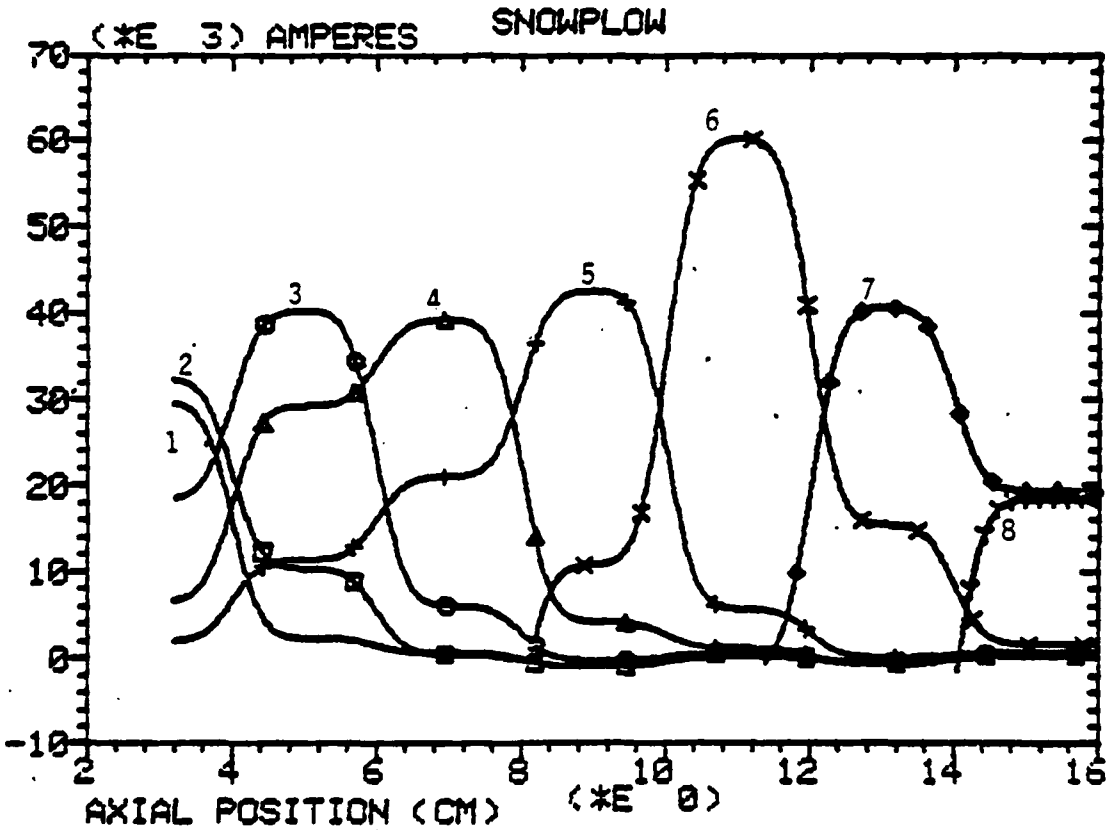

Figure II.15(c)

Current Distribution for Snowplow.

does not vanish even when the Rogowskii coil is registering a zero current. This is typical of the operation of coaxial plasma guns (see, for instance, ref. 8 and 9). This may be due to some transient magnetic field being frozen within the electrodes, due to high conductivity.

Figures II.15(b) is an overlay of a number of cross-plots showing the magnetic field distribution in the gun at different times during the discharge. The sampling times are at 1 μs intervals after the arrival of the sheath at the first probe. The symbols on each trace are for trace identification purposes only. It can be seen from these plots that there is an obvious magnetic front advancing from the breech towards the muzzle end of the gun at a nearly constant velocity. Differentiating these traces yields the current density within the electrodes. These are plotted in Figure II.15(c) showing the current distribution in the gun at 1 μs intervals. It is very clear from these plots that there is a current sheath about 2 cm in width, starting from the breech and moving outward at an average velocity of about 3 cm μs^{-1}. The gas used in this shot is argon.

The Deflagration Mode

In contrast to the snowplow mode of gun operation, the deflagration mode can only be achieved in a puff system. The most assured way of getting the plasma gun to operate in this mode is to connect the capacitor bank directly across the electrodes with no external switches. The gun itself acts as a switch for the system. Discharge is initiated when the puff of gas enters the inter-electrode region. If an external switch is present in the system, it should be triggered just before the puff of gas enters the inter-electrode region. If the switch is triggered very early, before the arrival of the gas, the gun will not fire until enough gas has been admitted to reach the breakdown threshold. The waiting time is the intrinsic time delay of

the gun. It varies from shot to shot depending on the time at which the switch is triggered and the condition of the gas feed. Intuitively, one would expect to observe deflagration type discharge only at small time delays; nevertheless, this has also been observed in some cases where the delay time has been set relatively long. In such cases, factors other than the time delay between puffing the gas and firing the bank may be influencing the operation of the plasma gun. Other factors that can possibly affect the operation of the gun are contamination of the vacuum system (especially from the diffusion pump and exposure to the atmosphere if the system is opened to air regularly), accumulation of debris (especially if the gun has been operated for an extended period of time), gas feed condition, uniformity of initial neutral gas density, and the initial gas breakdown position.

A set of deflagration data is analysed in the similar manner as the snowplow case in the previous section. The plots are presented in Figure II.16(a), (b), and (c). From these plots, it is easy to see that the operation of the plasma gun is different from the snowplow mode. We recall for the snowplow case that the gun is fired after a long time delay; therefore the gas puff will have sufficient time to fill the plasma gun to a relatively high pressure (> 10 Torrs) and distribute itself uniformly. In the deflagration mode however, the capacitor bank is fired early in time, just as the puff of gas is entering the system through the four injector ports at the breech of the gun. Here again, the preferred path for the initial breakdown to occur is at the breech where the gas is admitted. There is probably insufficient time for the gas to spread out uniformly so the initial gas distribution is very non-symmetric; hence there is a high probability of spoke formation as observed in the open shutter photographs. The current distribution in the plasma sheath will also

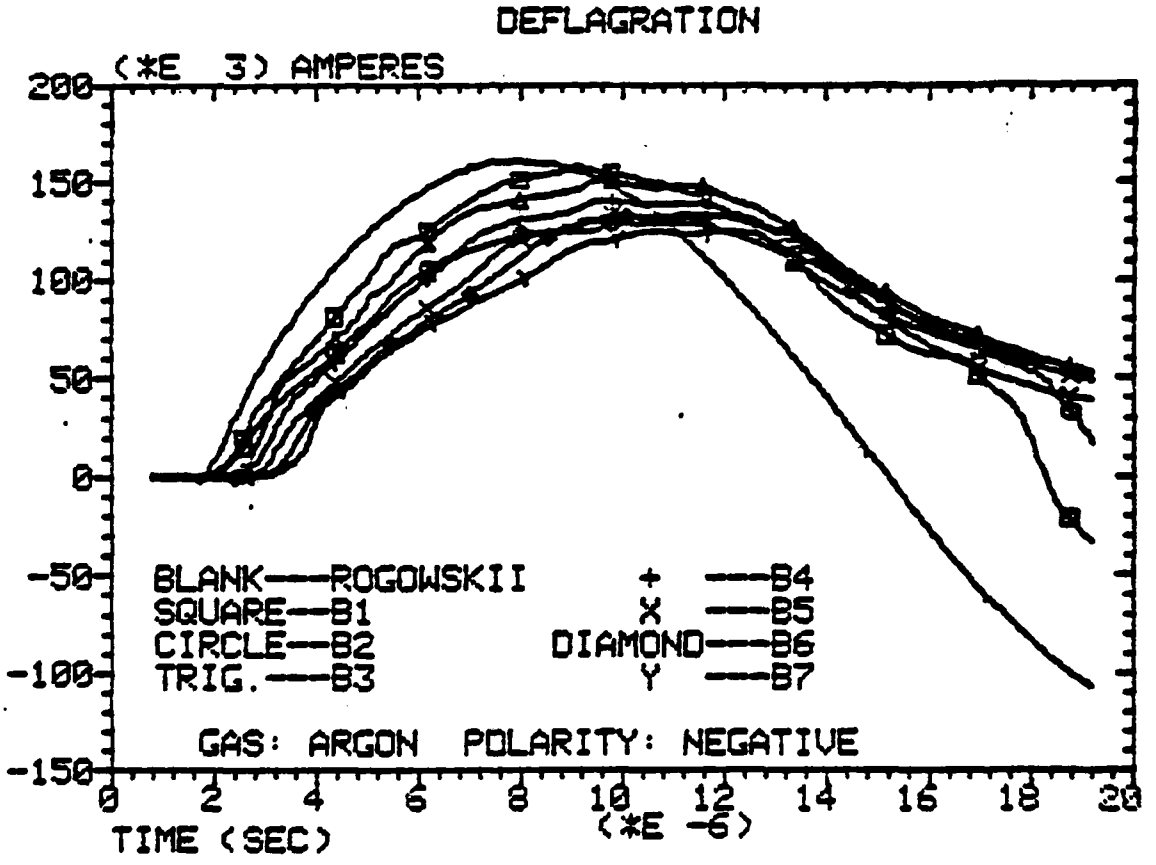

Figure II.16(a)

Current and B_9 Traces for Deflagration.

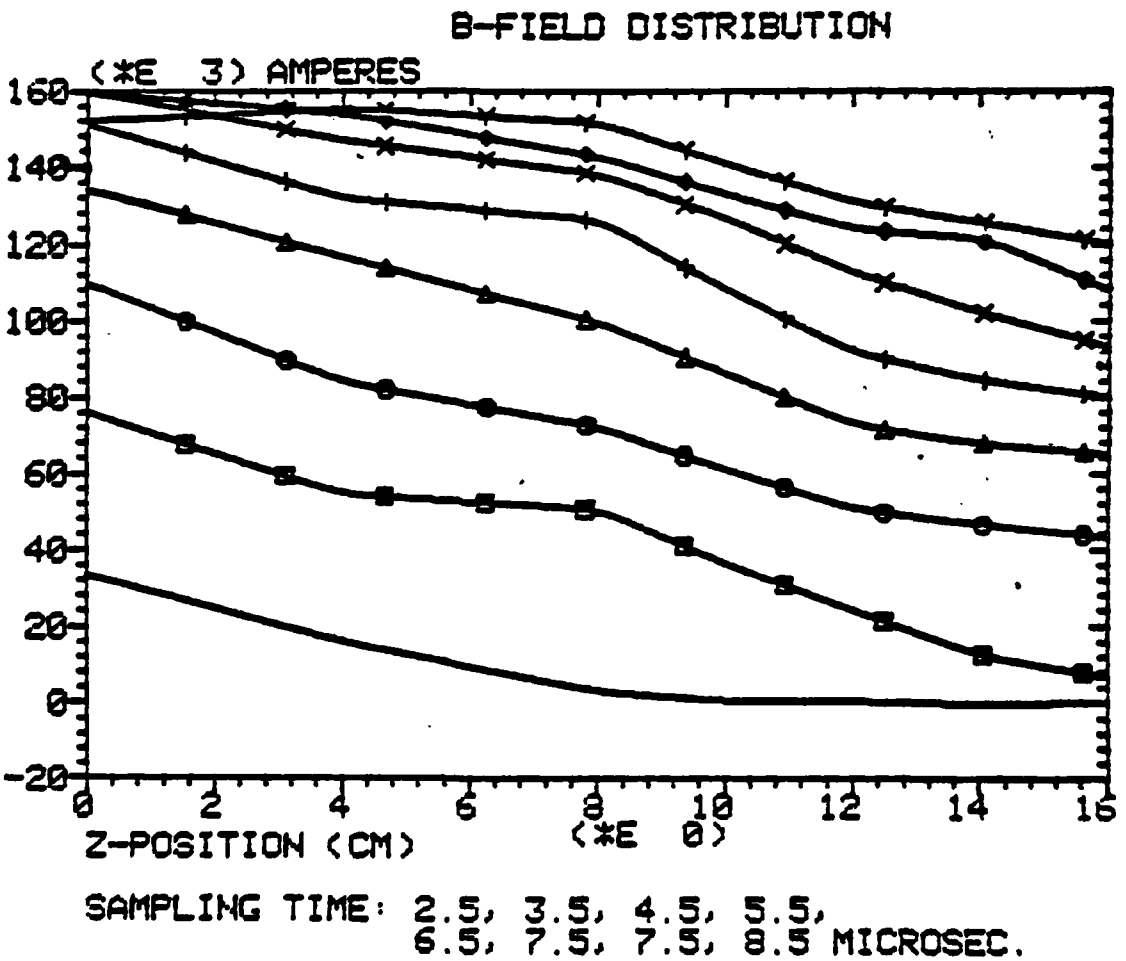

Figure II.16(b)

Magnetic Field Distribution for Deflagration.

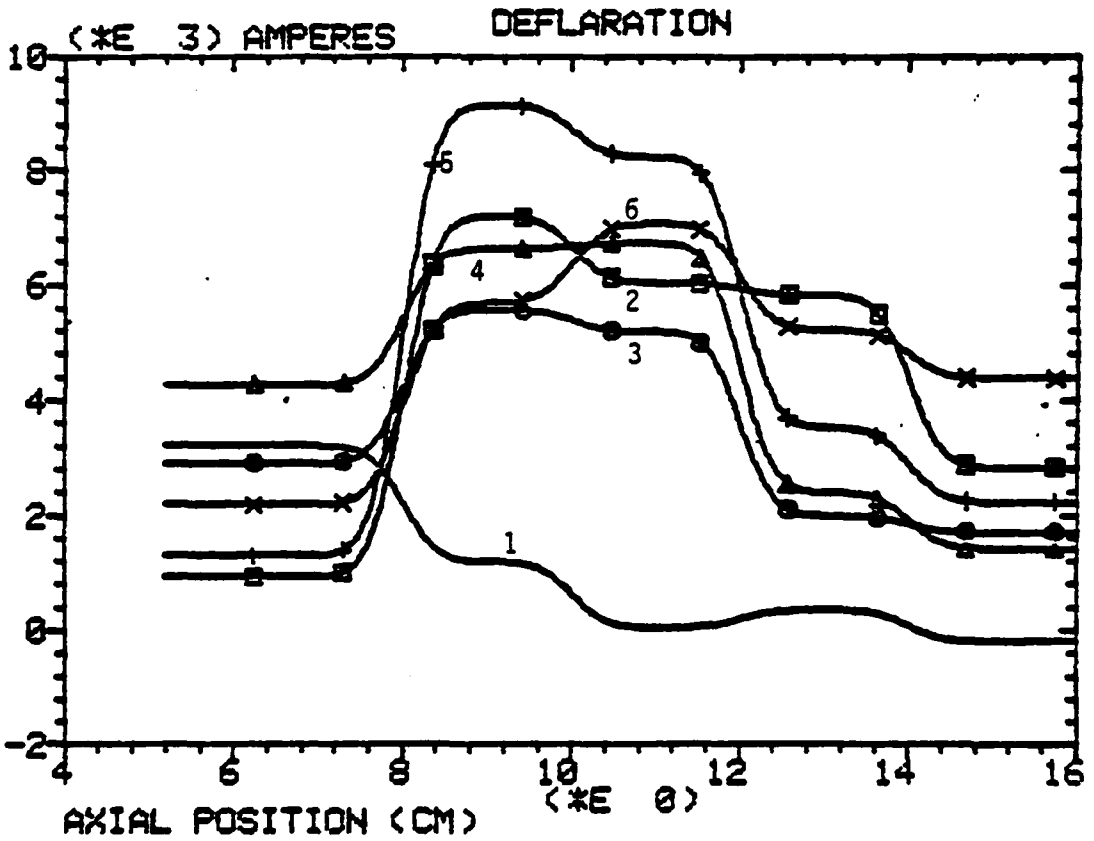

Figure II.16(c)

Current Distribution for Deflagration.

be non-symmetric. This indeed is the case as shown in earlier sections. Another significant difference for the deflagration mode is that there is a vacuum in front of the discharge. No shock waves are generated, so the plasma temperature and hence the electrical conductivity of the plasma remains low. As a result, the current is very diffused, as is the magnetic field. The ions and electrons formed in the discharge region are accelerated outwards via the $\underset{\sim}{E}x\underset{\sim}{B}$ interaction. The plasma accelerates and expands into the vacuum region in front of the discharge, providing current carriers which quickly spread the current across the entire length of the electrodes. This can be easily deduced from Figure II.16(a) which shows that each probe picks up its magnetic signals very quickly. The speed of the deflagration plasma is much faster than the snowplow plasma, as is evident by the closeness of the B_θ-traces in Figure II.16(a). For the shot analysed here, the axial speed of the discharge is about 11 cm μs^{-1} as opposed to 3 cm μs^{-1} for the snowplow data in the previous section. As a new supply of neutral gas continuously enters the gun at the breech, new discharge current channels are continuously formed there and spreading downstream.

Formation of new discharge channels at the breech is possible in the deflagration mode because of two reasons. First, the puff of gas travels about 40 cm from the pulse valve to the injector ports. As a result, the density gradient at the leading edge is no longer steep by the time it reaches the gun. In fact the gas density at the leading edge will have developed a finite spatial gradient which allows for the selection of the optimum (Paschen minimum) breakdown point in the density profile. Second, the electrical conductivity of the plasma in the discharge region is low; consequently, the impedance of the path near the breech of the gun will be the lowest. The combination of these

two effects makes the continuous formation of new discharge at the breech possible. This discharge process thus produces a current sheath that is broad and quasi-stationary within the electrodes. Since we do not have a thin sheath carrying all the current and moving downstream, we do not have a sharp rise in the B_θ-signals as observed in the snowplow case.

The variation in time of the B_θ-signal is shown in Figure II.16(a). Figure II.16(b) shows the magnetic field distribution in the gun at 1 μs intervals. Unlike the snowplow case, there is no steep front propagating away from the breech. The profile of the magnetic field distribution remains almost unchanged as the magnitude varies in accordance with the current flowing through the gun. The derivative of the field distribution yields the distribution of the current density. Figure II.16(c) shows the current distribution inside the gun at 1 μs intervals. As expected, there is no evidence of any moving current sheath. On the contrary, the current is distributed over a broad region and it remains stationary within the electrodes as its magnitude changes in time. The slight irregularities in these plots are the result of low spatial resolution measurements using only a few probes (2 cm apart).

As mentioned earlier, the deflagration-type discharge is sometimes observed even at long delay times. A possible explanation rests on erratic behavior of the gas puff valve system which occasionally malfunctions. Regular gas front evolution measurements could not be made on the discharge shots because of the destructiveness of the energetic plasma to detection components.

The Transition Mode

The transition from snowplow to deflagration is very difficult to study because the result is not reproducible and the transition process does not occur very frequently. In practice, the gun usually operates in either the snowplow or the

deflagration mode, seldom in the transition mode. In studying the transition region, the delay time is set such that the gun is only partially filled with gas when the capacitor bank is fired. In this situation, the distribution of the gas inside is still not uniform. The minimum impedance (not inductance) path is not fixed, but depends on the initial condition of the distribution of the gas. We know that the minimum inductance path is the one over the breech insulator while the Paschen minimum for gaseous breakdown is most likely to be located at the middle of the electrode where the gas front is. These two positions will be competing for the initial breakdown, which will take whichever path that has the minimum impedance (the combined inductance and resistance).

When the capacitor is discharged through the gun, one of two processes will occur depending on the initial position of the discharge. If the initial breakdown occurs at the front of the gas puff, then the gun will operate in the deflagration mode. On the other hand, if the initial discharge strikes at the breech of the gun, then we will have a situation quite similar to the snowplow initially. The only differences are that the gas density is lower and less uniform, and the gas feeding rate is lower. The shock wave that results from the discharge is moving into a decreasing density; hence it is not as strong. Thus the electrical conductivity of the plasma should be relatively low. As the current sheath plows forward, fresh supply of neutral gas is fed into the gun. The current sheath in this case is still being fed at a lower rate by the leading edge of the gas puff which has a gentle density gradient. Thus the electrical breakdown threshold is low because of low gas density. As the current sheath plows forward, secondary discharges will occur behind it, spreading through diffusion of magnetic field to fill up the region between the breech insulator and the snowplow current sheath. As

more and more current flows near the breech region (where the inductance is lower), the snowplow becomes less and less effective. By the time it reaches the position of the probe B7, it is not much of a sheath any more. The set of data that exhibits these characteristics has been presented in an earlier section in Figure II.14(e). It can be seen very clearly that the B_θ-traces exhibit both snowplow and deflagration features. The data is analysed and shown in Figure II.17(a) and (b).

If the region behind the snowplow current sheath is not filled with secondary discharges, then we will have a very interesting situation in which the initial gas in the gun (constant mass) will be accelerated by the $\underset{\sim}{J}x\underset{\sim}{B}$ force outwards. It will be a classic example of the so-called slug model [12, 13]. In that case, the B_θ-signals should look exactly like the snowplow mode and the current sheath should move at a faster speed. Further details of the work presented in this section are given in reference [14].

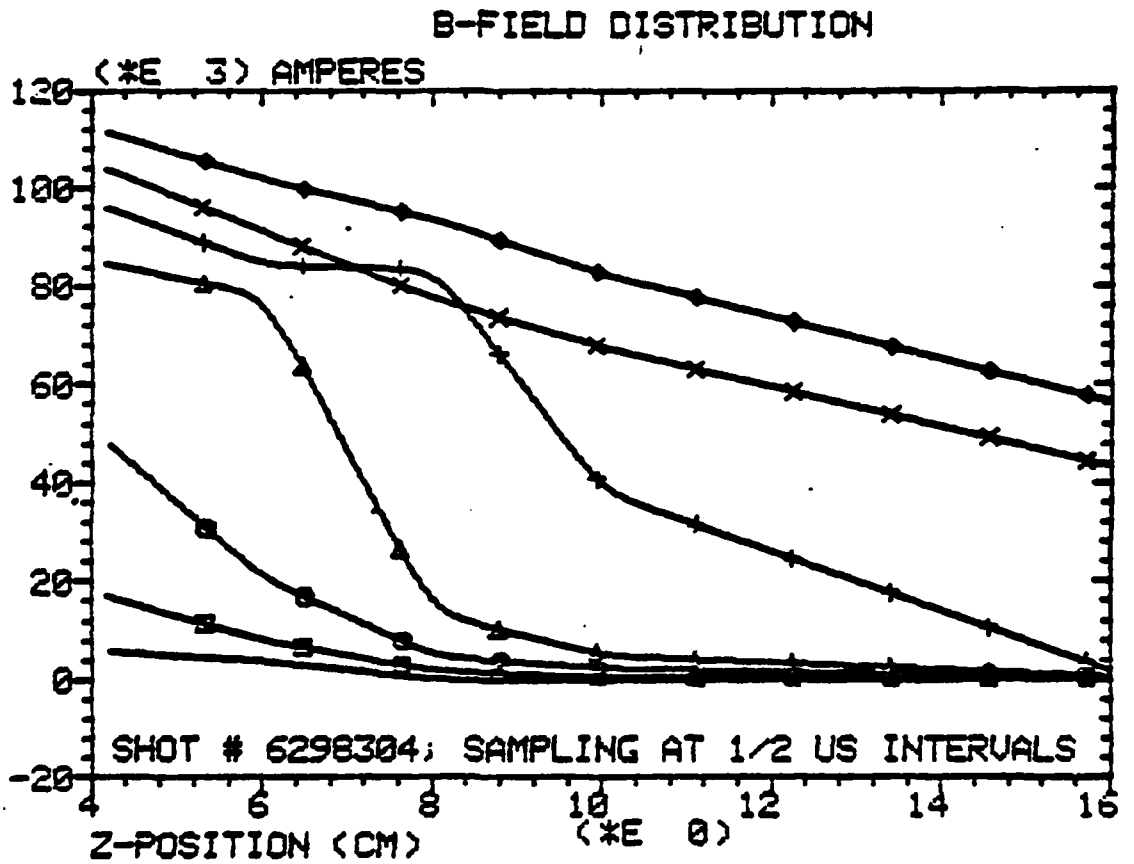

Figure II.17(a)

Magnetic Field Distribution for the Transition from Snowplow to Deflagration. (for Fig. 62(e))

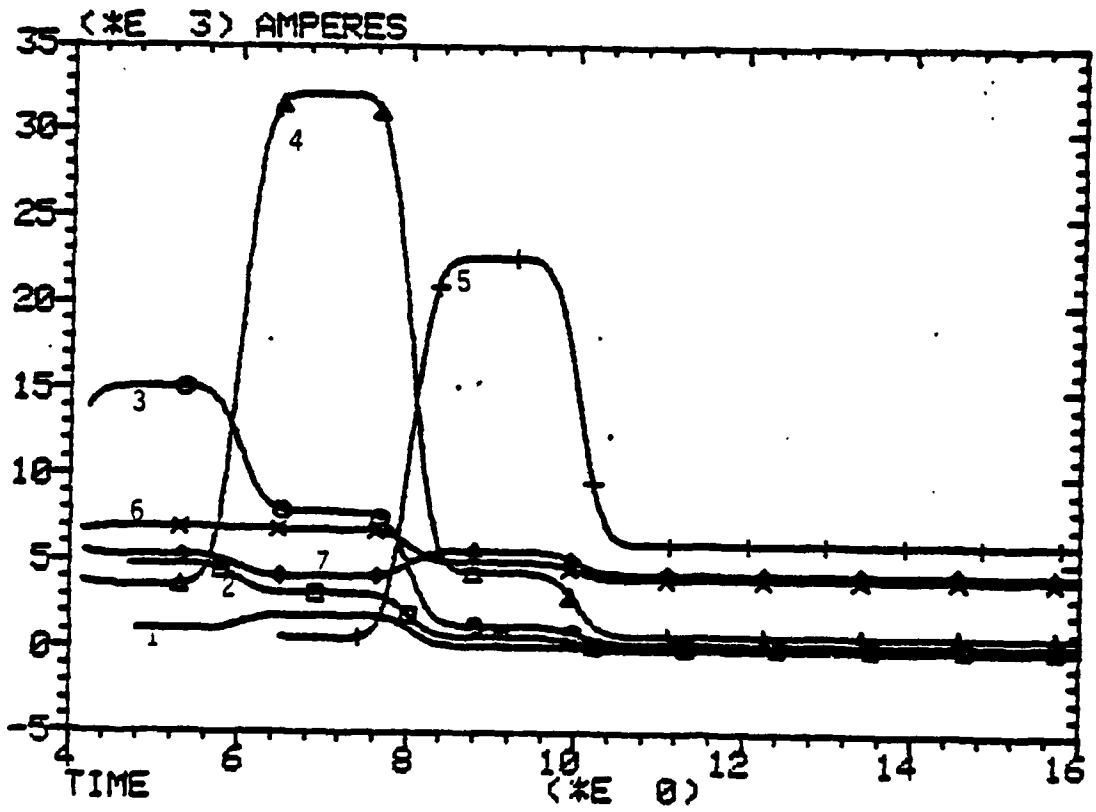

Figure II.17(b)

Current Distribution for the Transition.

SECTION II REFERENCES

II. 1. Thode, L. E. and Sudan, R. N., Phys. Fluids 18, 1552 (1975) and Phys. Fuids 18, 1564 (1975).

II. 2. Thode, L. E., Phys. Fluids 19, 305 (1976).

II. 3. Thode, L. E., Phys. Fluids 20, 2121 (1977).

II. 4. Sethian, J. D. and Ekdahl, C. A., Phys. Rev. Lett. 42, 711 (1979).

II. 5. Clark, M. C., "Foilless Diode Operation on a 7 MeV, 80 kA Electron Beam Machine," Bull. Am. Phys. Soc. 74, 1085 (1979).

II. 6. Cheng, D. Y., Nuclear Fusion 10, 305 (1970).

II. 7. Cheng, D. Y., "The Application of a Deflagration Gun to Fusion Systems," Proc. of High Beta Workshop, Los Alamos (1975), p. 681.

II. 8. Mather, J. W., "Investigation of the High-Energy Acceleration Mode in the Coaxial Gun," Phys. Fluids, Suppl., S28, (1964).

II. 9. Dattner, A. and Eninger J., "Studies of a Coaxial Plasma Gun," Phys. Fluids, Suppl., S41, (1964).

II. 10. Wilcox, J. M., Pugh, E., Dattner, A. and Eninger, J., "Experimental Study of the Propagation of an Ionizing Wave in a Coaxial Plasma Gun," Phys. Fluids, Suppl., S51 (1964).

II. 11. Wolf, R. J., Sorrell, F. Y., and Nagakawa, Y., "Computation of Current Sheet Speeds in Plasma Acceleration," AIAA Journal, 8(4), 807, (1970).

II. 12. Michels, C. J., Heighway, J. E., and Johansen, A.E., "Analytical and Experimental Performance of Capacitor Powered Coaxial Plasma Gun," AIAA Journal, 4(5), 823, (1966).

II. 13. Mostov, P. M., Neuringer, J. L., and Rigney, D.S., "Electromagnetic Acceleration of a Plasma Slug," Phys. Fluids, 4(9), 1097 (1961).

II. 14. Len, L. K., "The Snowplow and Deflagration Modes of Operation in Coaxial Plasma Guns," Ph.D. dissertation, University of New Mexico, 1984.

Appendix to Section II
MAGNETIC PROBE CONSTRUCTION AND CALIBRATION

Each of the magnetic probes used in this experiment has an average diameter of 2 mm and consists of 4 turns of 32 AWG copper wire protected by a ceramic tube. The size of the ceramic tube is 2.5 mm ID by 4.8 mm OD by 2 inches. One such probe is shown in Figure A-1. These probes are calibrated in a Helmholtz coil, which is comprised of two coils separated at a distance equal to the radius of the coils. For the Helmholtz coil constructed for the present experiment, there are two turns in each current loop. The coils are wound on a lucite structure as shown in Figure A-2. It is driven by a 1- F capacitor, charged to 5 kV. The magnetic field in such a device is given by

$$B_z = B_{zo}\left\{1 - \frac{18}{125}\left[3\left(\frac{x}{R}\right)^4 - 24\left(\frac{x}{R}\right)^2\left(\frac{z}{R}\right)^2 + 8\left(\frac{z}{R}\right)^4\right] + \ldots\right\} \quad \text{(A-1)}$$

$$B_x = B_{zo}\left\{\frac{72}{125}\frac{xz}{R^2}\left[4\left(\frac{z}{R}\right)^2 - 3\left(\frac{x}{R}\right)^2\right] + \ldots\right\} \quad \text{(A-2)}$$

$$B_{zo} = \frac{\mu_o NI}{R} \times 0.715 \text{ Tesla} \quad , \quad \text{(A-3)}$$

where N is the number of turns in each loop, R is the loop radius, x and z are the perpendicular and axial displacements from the mid-point of the Helmholtz coil. The magnetic field is very uniform in the vicinity of the axis. The field inside is plotted in Figure A-3.

In-situ B-dot Probes Calibration

It has been found in the course of these experiments that installing the probes at the exact radial position and θ-orientation is very difficult. These probes are all hand-made by inserting the coil into the ceramic tube and then sealed with

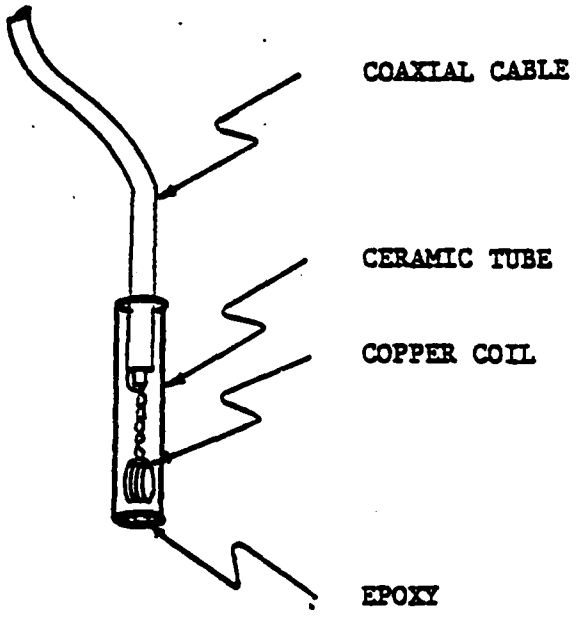

Figure A-1

B-dot Probe.

For our device, the field should have a deviation of less than 1 %. Since N = 2, I = 2937 A, and R = 5 cm, we should have B_z = 1056 gauss.

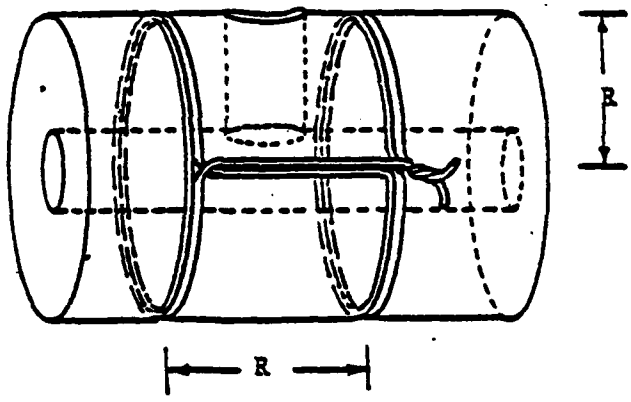

Figure A-2

Helmholtz Coil.

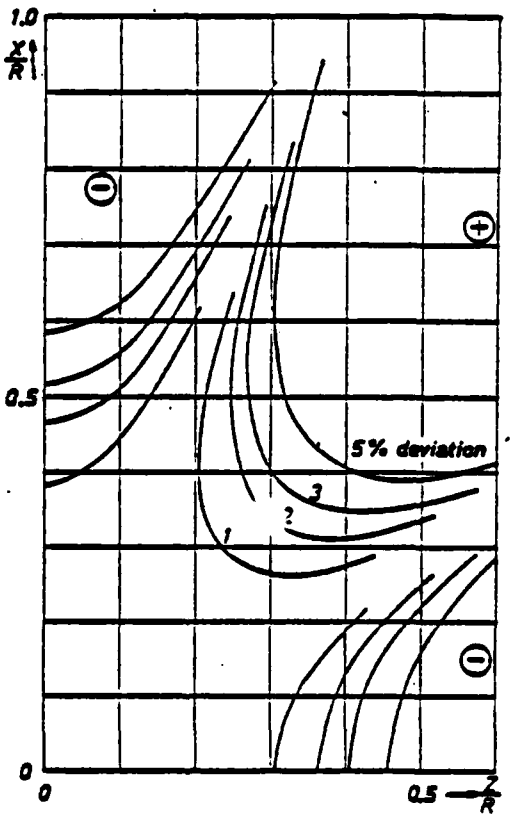

Figure A-3

Field Inside a Helmholtz Coil.

epoxy. The position of the coil within the ceramic tube may vary slightly from one probe to another. Even after all the probes have been carefully installed in the gun, the positions may still be disturbed slightly when the signal cables are attached and the vacuum system is assembled. To get an idea of how much error can be introduced, let's take a 2 mm and 20° error in probe position. The current and B-field relation is given by

$$I = \frac{2\pi r B}{\mu_o} \tag{A-5}$$

so

$$\frac{\Delta I}{I} = \frac{\Delta r}{r} + \frac{\Delta B}{B} \tag{A-6}$$

$$= \left\{ \frac{2 \text{ mm}}{22.2 \text{ mm}} + (1 - \cos 20°) \right\} \cdot 100\%$$

$$= 9\% + 7\% = 16\%.$$

The error is more important still when probe data is correlated to obtain the current distribution over the length of the gun, since adjacent signals are subtracted.

A simple way to overcome this problem is to calibrate the probes in situ after installation is completed prior to the experiment. This is done by shorting the gun at the muzzle end with symmetrically placed grounding straps which are connected to the electrodes by means of hose clamps as shown in Figure A4. The plasma gun chamber is evacuated to prevent any electrical discharge inside the gun barrel which would most definitely spoil the calibration. The capacitor bank is charged to an appropriately low voltage and switched onto the shorted gun. Since the gun is under high vacuum, there can be no plasma discharge within the gun barrel. This is verified by monitoring with an open shutter camera. Thus the current will only flow through the electrodes and through the grounding straps at the

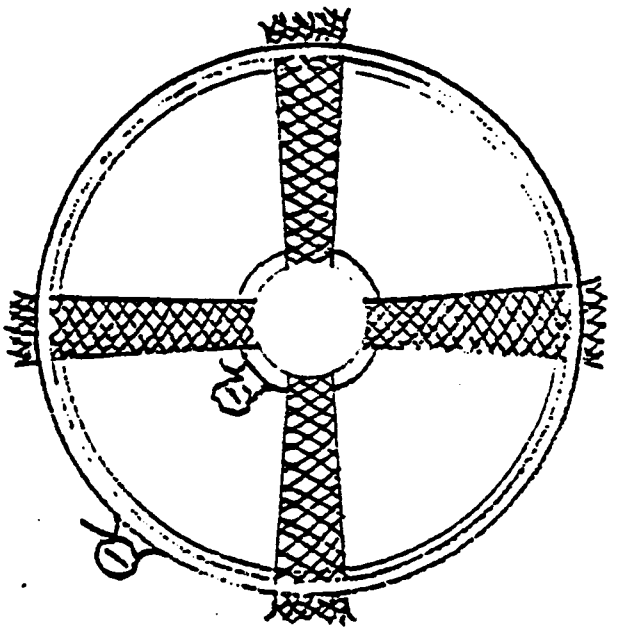

Figure A4

Short-Circuiting at the Gun Muzzle
Using Grounding Straps.

muzzle end. The signals from the B-dot probes are integrated at the oscilloscopes and are then calibrated against a standard current monitor (PI CM-1-T). The procedure must be repeated whenever the probes are disturbed or reshuffled. A set of calibration data is shown in Figures A5 and Figure A6. The data from different probes has been overlayed in one graph and the peak values of each plot used for computing the calibration factors. These calibration factors allow us to scale the oscillogram signals directly to current without having to calculate the magnetic field first.

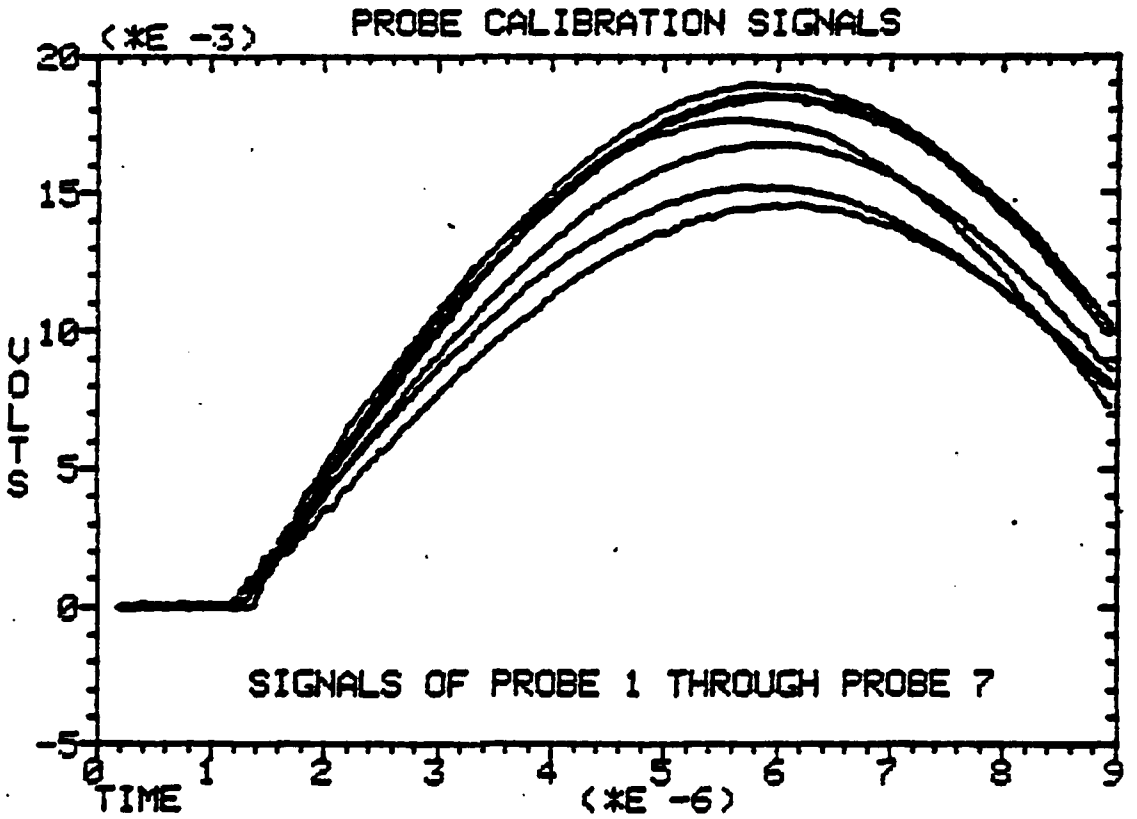

Figure A-5

Typical B_θ-dot Probe Calibration Traces.

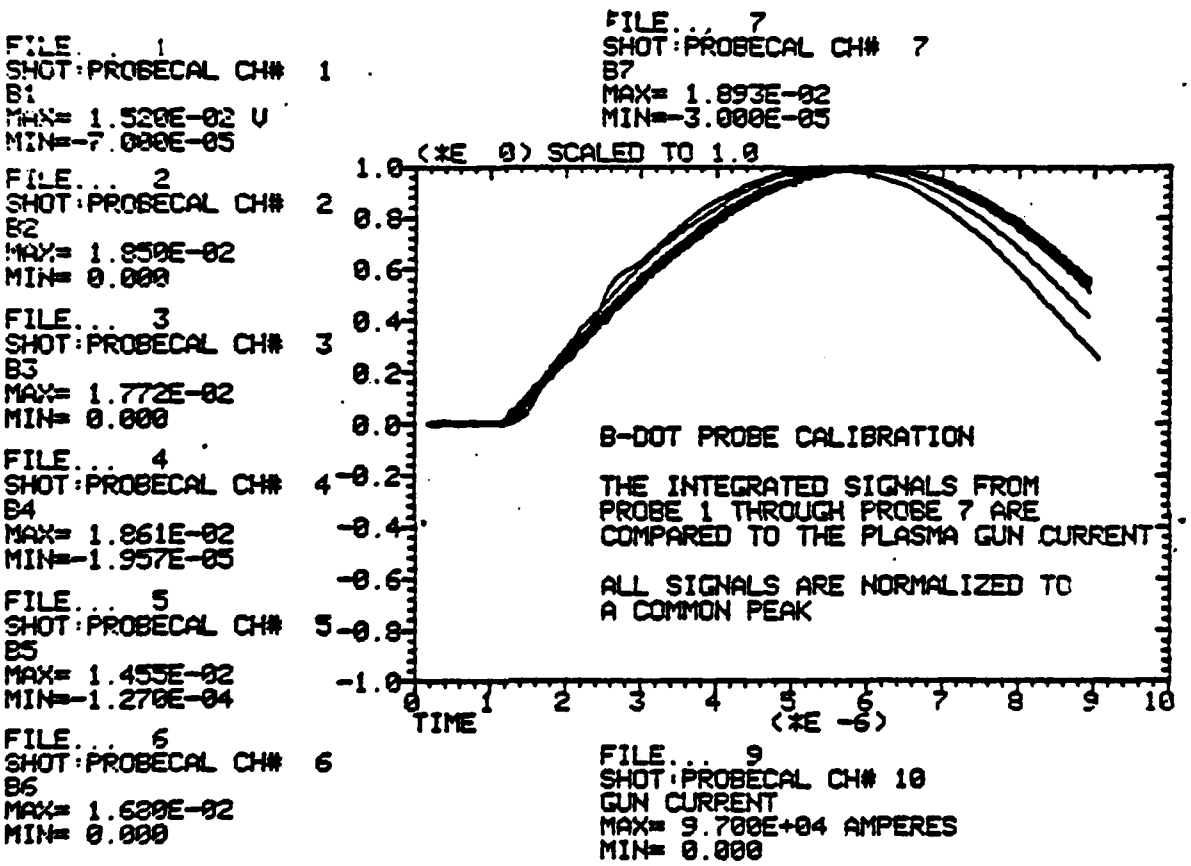

Figure A-6

Typical B_θ-dot Calibration Traces
Normalized and Compared to Current Standard.

LIST OF FIGURES

LIST OF FIGURES (Continued)

LIST OF TABLES

III. Intense REB-Neutral Gas Heating Experiments

G. F. Kiuttu and D. Woodall

As a prelude to studying the interaction of a Relativistic Electron Beam with a plasma, we examined the results of beam injection into a neutral gas [1]. This section will describe those experiments, with primary emphasis on the diagnostics which were developed to examine the resulting plasma. In particular, we wished to investigate the measurement of the Stark-broadened hydrogen H_β spectral line as a beam-plasma electron-density diagnostic.

For most of these experiments, the PR 1590 (REB machine) was configured with a 5 cm diameter solid cylindrical cathode tip, a 2 to 5 cm vacuum diode gap, and a carbon-coated 25 μm thick Kapton anode foil. The polycarbonate anode foil permitted injection of the 6 MeV, 100 KA beam into a 30 cm diameter, 3 m long stainless steel drift tube, backfilled with neutral hydrogen gas at pressures of one torr to several hundred torr. The low effective Z of the foil kept anode scattering, and hence beam temperature, low. In addition to the usual Rogowski coil current monitors and diode voltage monitor, a carbon calorimeter and 0.5 m visible spectrometer were routinely employed to measure transported beam energy and H_β profiles, respectively.

Stark-broadening theory for the hydrogen Balmer spectral lines is well understood [2,3] and has been verified in arc discharge experiments [4]. In particular, the H_β (2s - 4p) transition exhibits a FWHM which scales as $n_e 3/2$, essentially independently of temperature, over the range 10^{14} - 10^{17} electrons/cm^3 and a fraction of an eV to several eV (Figure III.1).

Furthermore, this line lies in the blue region of the visible spectrum (4861 A) and is relatively well isolated, making it an attractive candidate for an electron-beam plasma-density diagnostic. To measure the H_β linewidth a Jarrell-Ash stigmatic 0.5m

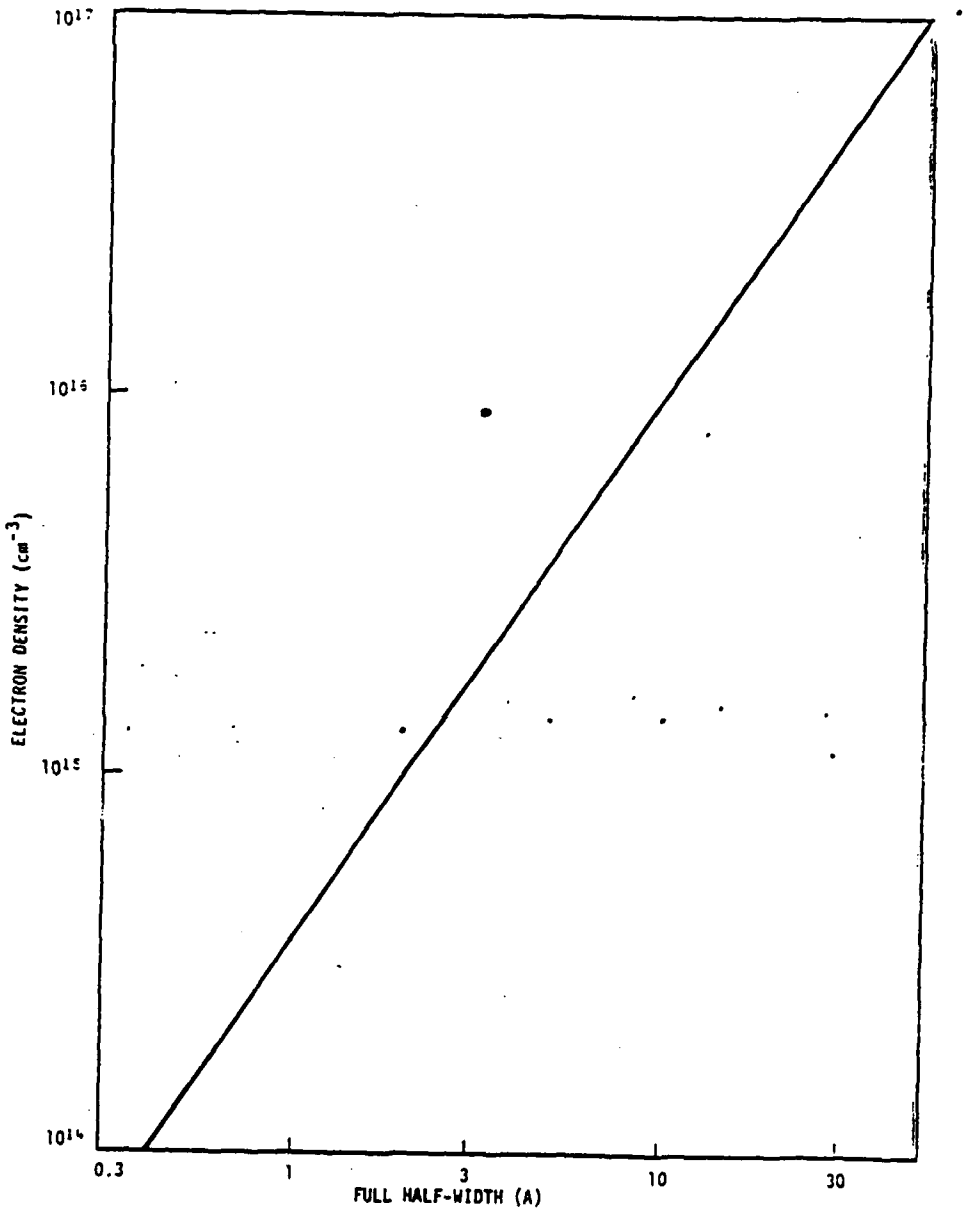

Figure III.1. Calculated half-width of the Balmer line H_β as a function of electron density for the temperature range from 5000 to 40,000 K. (from Ref. 5).

spectrograph was set up to view the beam propagation channel perpendicular to the drift tube axis (Figure III.2). The spatially-resolved H_β profiles obtained were converted to radial profiles via an Abel inversion [6], and the half-widths used to determine radial electron-density distributions.

1. Spatially-Resolved Stark-Width Measurement Technique

Preliminary to taking data, the spectrograph was aligned according to the procedures outlined in the factory manual. In addition to adjusting the focus and optimizing the resolution, the variable entrance slit width was calibrated using the diffraction pattern produced by a He-Ne laser. For most experiments, the slit was set at 200 μm, giving an instrument resolution of approximately 3 Å. Kodak Royal X-Pan 4 x 5 in. cut film was selected to record the spectra because of its high sensitivity. The film speed was pushed by development for 4 min in the Kodak D-19 developer. The spectrograph exit plane dispersion and relative film response were measured in situ using a neon calibration lamp at several wavelengths near hydrogen H_β. The instrument dispersion was found to be 16.06 Å/mm in the vicinity of 4861 Å. To determine the relative film response, the calibration spectra for different exposure times were scanned with a diffuse microdensitometer (Perkin-Elmer). The relative exposures, in optical density units above background fog, were found to obey the simple empirical relationship

$$D = a + b \ln t , \qquad (1)$$

where D is in optical density units, t is the exposure time in seconds, and the parameters a and b were determined from linear least-squares fitting of the data. Table 1 shows the values of the fitting parameters obtained at selected Ne wavelengths. From these values, a and b for the H_β line at 4861 Å were estimated to be -0.43 and +0.2, respectively.

To match the f/8 numerical aperture of the spectrograph, external optics consisting of two 45° mirrors and an apertured

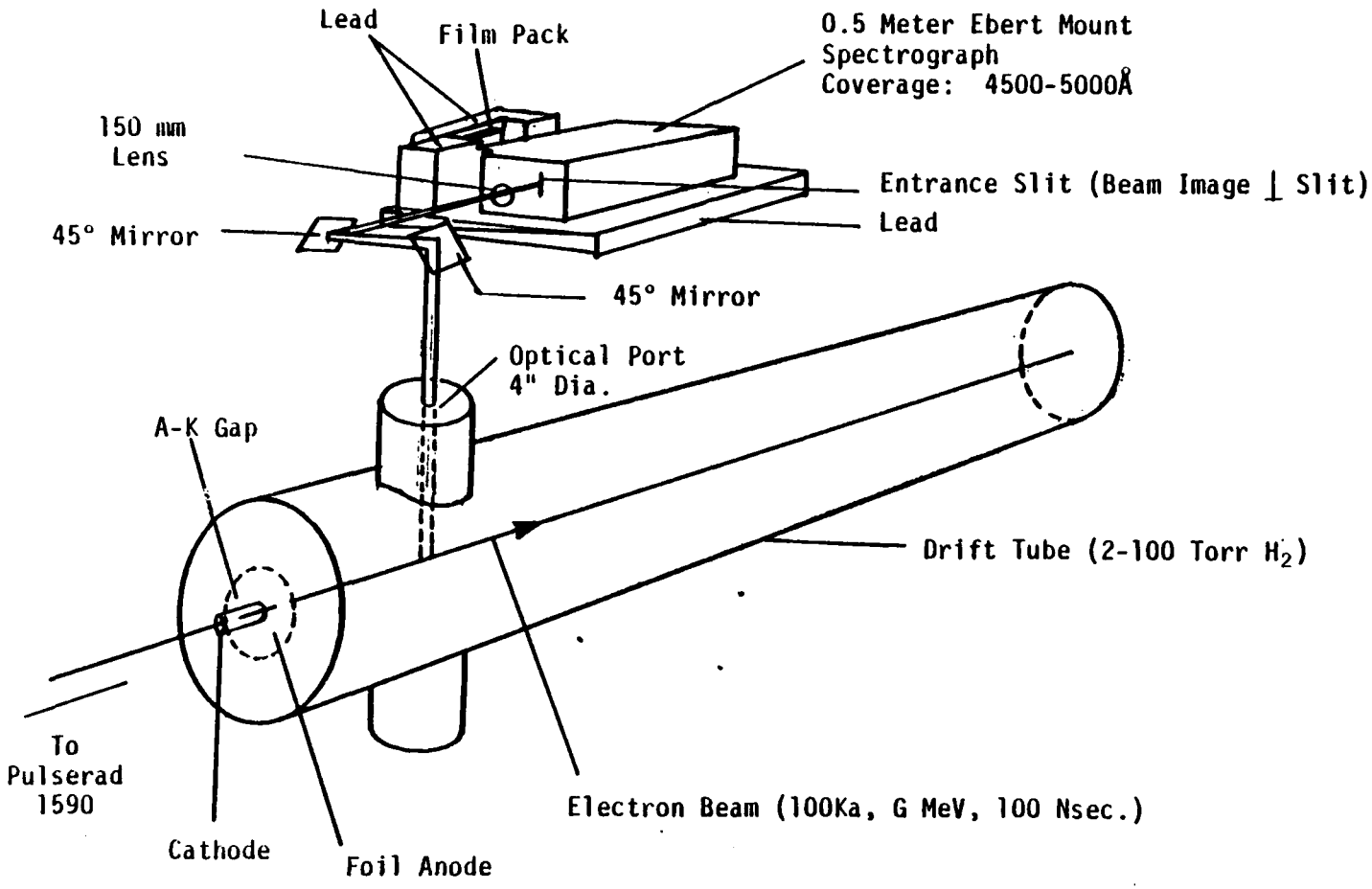

Figure III.2. Spectrograph Setup

Table III.1

Fitting parameters for Kodak Royal X-Pan relative film response at selected wavelengths.

λ (Å)	a	b
4715	-.2207	+.2284
4837	-.3438	+.2243
4876	-.4826	+.1964
4914	-.3775	+.2426
5031	-.3609	+.2728
5037	-.1290	+.4460

150 mm focal-length lens were used to image a 1.5 mm long section of the plasma channel onto the entrance slit with a magnification of 0.14.

A carbon calorimeter located at the end of the drift tube and Rogowski coils mounted along the inside of the tube measured transported beam energy and net beam current, respectively. Additionally, for several shots, a plastic witness foil was taped to the anode to record the injected beam intensity pattern.

H_β spectra were recorded at fill pressures of 1, 2, 5, 10, 20, 50, 100, and 200 torr. A typical record is shown in Figure III.3. Determining the radial electron density profile from such a record involved the following steps. First, the record was microdensitometered and the optical density stored as a function of position in a 200 by 100 array on magnetic tape. The microdensitometer spot size was 100 μm square, and the resulting image field was 2 cm in the spatial (x) direction and 1 cm in the dispersion (y) direction. Next, the data was transferred to a PDP 11 data file for interactive analysis performed by a sequence of processing subroutines. The first of these scanned the data field and subtracted out the background fog density. The next converted optical densities to relative spectral intensities, I(x,y), using the film response calibration information of Equation (1). At this point it was necessary to transform the spatial intensity profiles to radial emissivity profiles by Abel inversion. Since the H_β line is an optically thin transition, the intensity of the line at the detector (entrance slit) is the line integral across chords of emitting disk as shown in Figure III.4. If the emissivity is assumed to be azimuthally uniform, the intensity is given by

$$I_y(x) = 2\int_0^{(r_o^2-x^2)^{1/2}} \varepsilon(r)\, dz = 2\int_x^{r_o} [r\varepsilon(r)/(r^2 - x^2)^{1/2}]\, dr ,$$

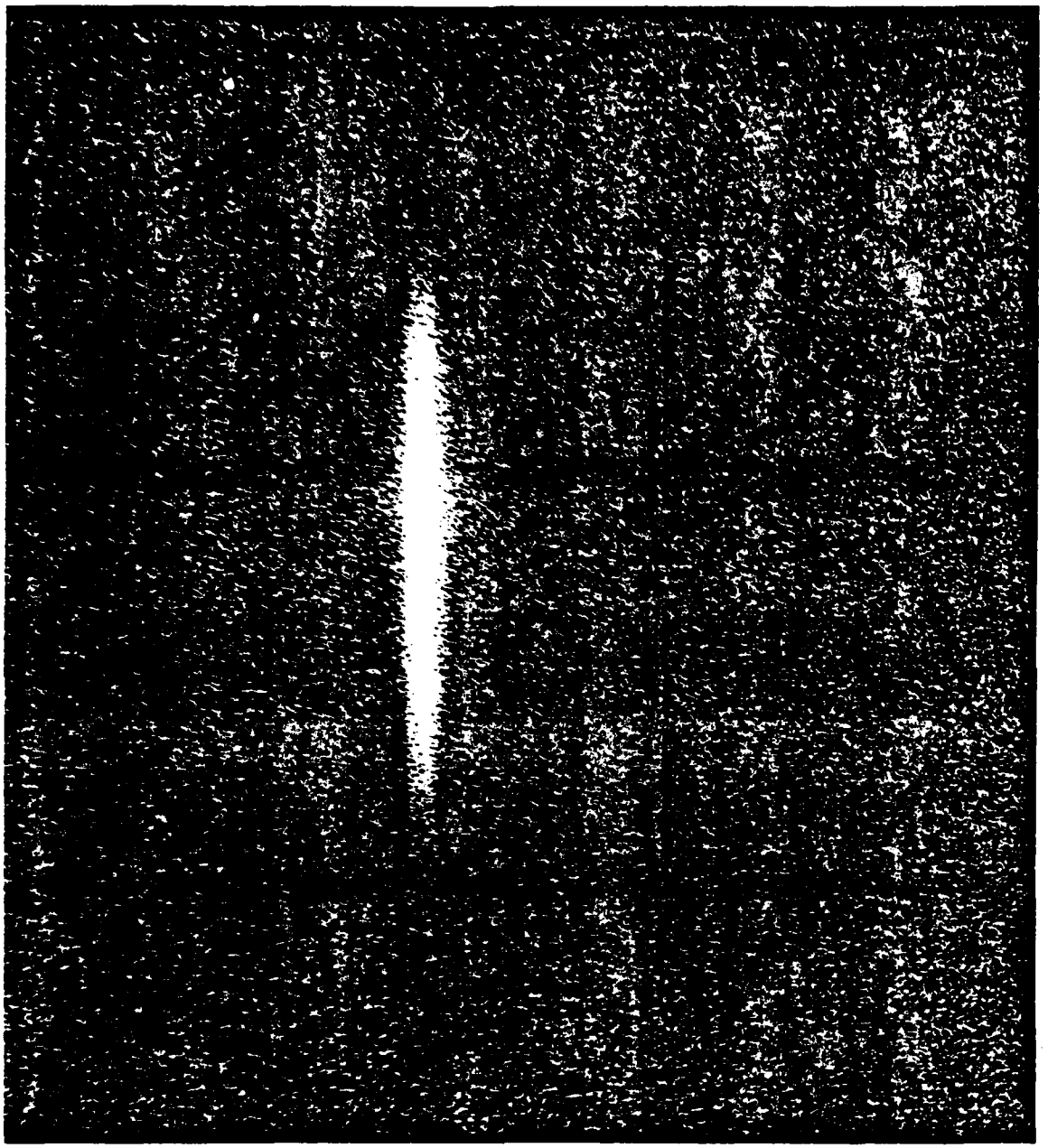

Figure III.3. Typical H_β record.

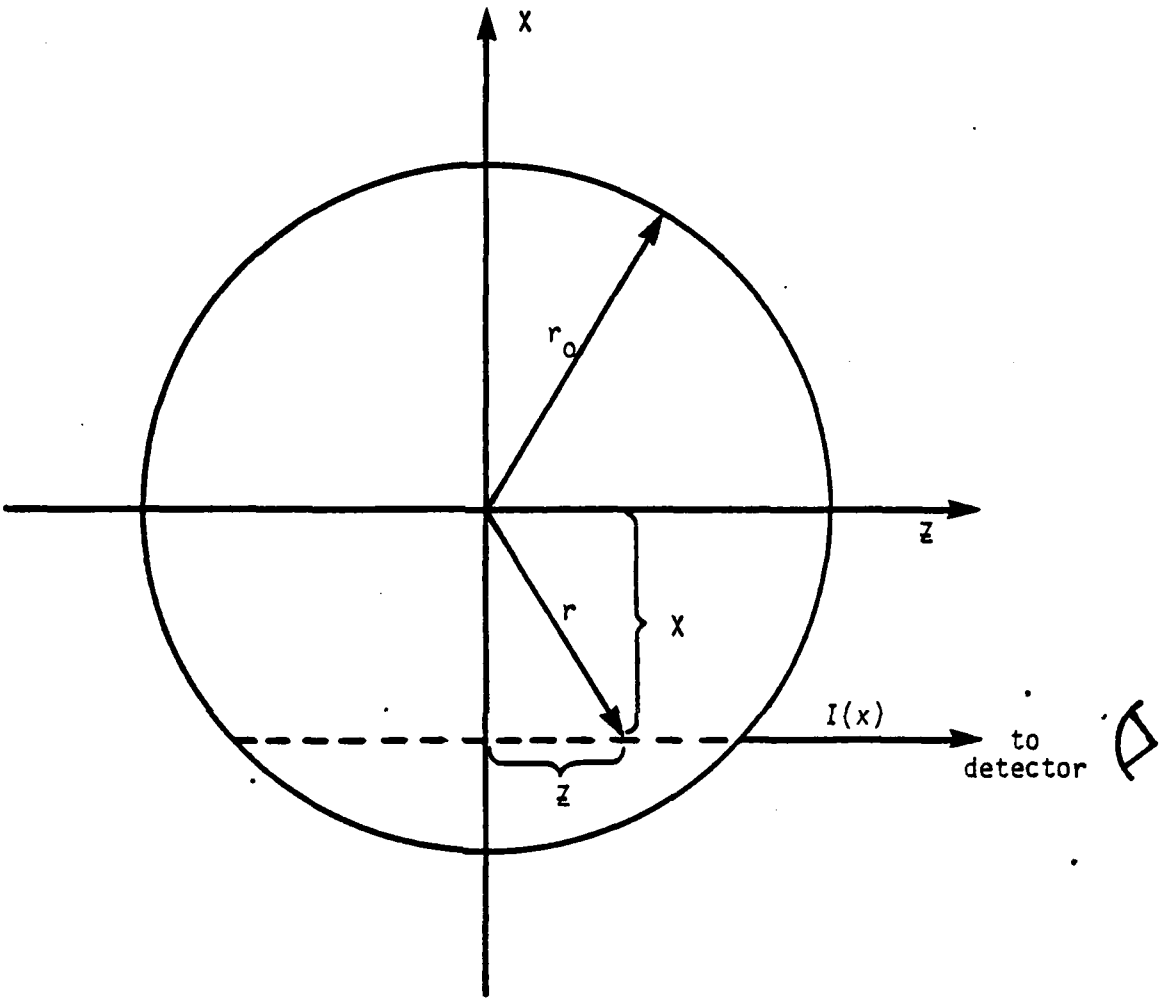

Figure III.4. Geometry for Abel inversion integrals

where ε is the emissivity, r_o is the plasma radius, and the plasma is observed in the z direction. The radial emissivity profile is then given by the Abel inversion integral,

$$\varepsilon(r) = -\frac{1}{\pi}\int_{r}^{r_o} \frac{dI(x)/dx}{(x^2 - r^2)^{1/2}}\, dx \ . \tag{3}$$

Thus, at each wavelength location (y location on the film), the spatial (x) intensity distribution had to be inverted according to equation (3). This was accomplished by first calling a subroutine which fits a polynomial to the data $I_y(x)$,

$$I_y(x) = \sum_{k=0}^{N} c_k x^k \ , \tag{4}$$

where N was determined by minimizing the reduced chi-squared value of the fit for $1 \leq N \leq 10$ [7]. To ease the job of fitting, the $I_y(x)$ data was split into two halves, $I_A(x)$ and $I_B(x)$, and each fit separately, as shown in Figure III.5. By comparing the two halves, we were able to check for azimuthal uniformity in a gross fashion. With $I_y(x)$ represented by polynomials, the inversion integrals were performed analytically by another subroutine which made use of formulae from tables of integrals [8]. Finally, the resultant $\varepsilon_A(r)$ and $\varepsilon_B(r)$ were reconstituted as wavelength profiles at different radii and plotted as in Figure III.6. From these profiles, the half-widths were estimated and corresponding electron densities determined and plotted.

2. Results of Measurements

Figure III.7 shows a plot of net beam current and total transported energy versus fill pressure. I_{net} is monotonically increasing with pressure, whereas energy transport is peaked at 20 torr, with significant energy transported up to 100 torr. The increasing net current indicates a decreasing plasma current

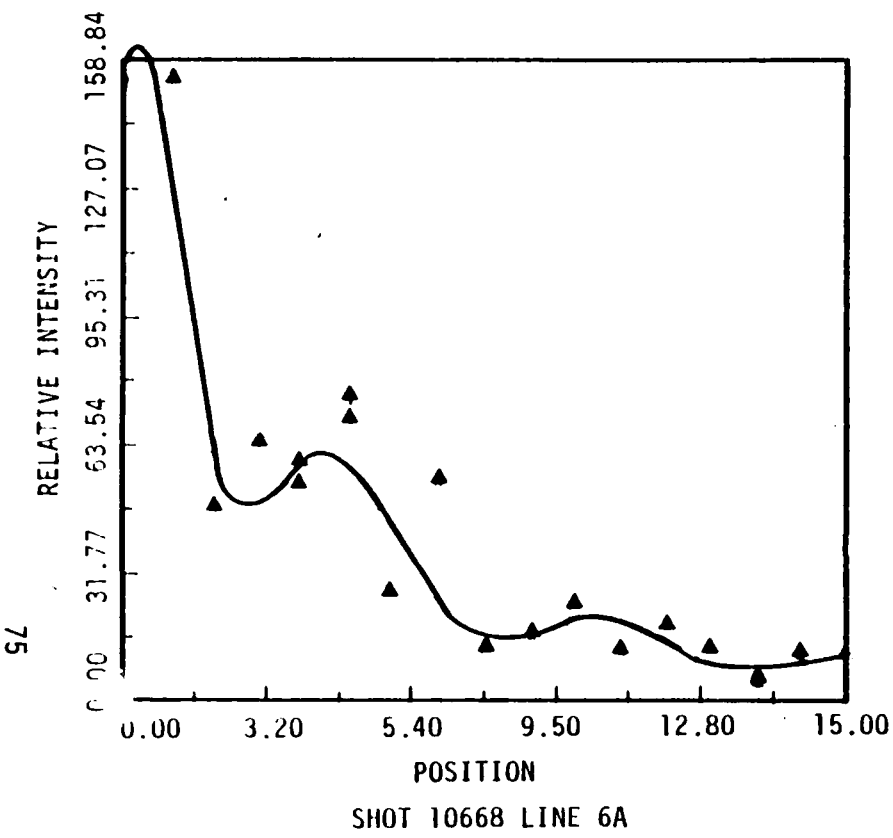

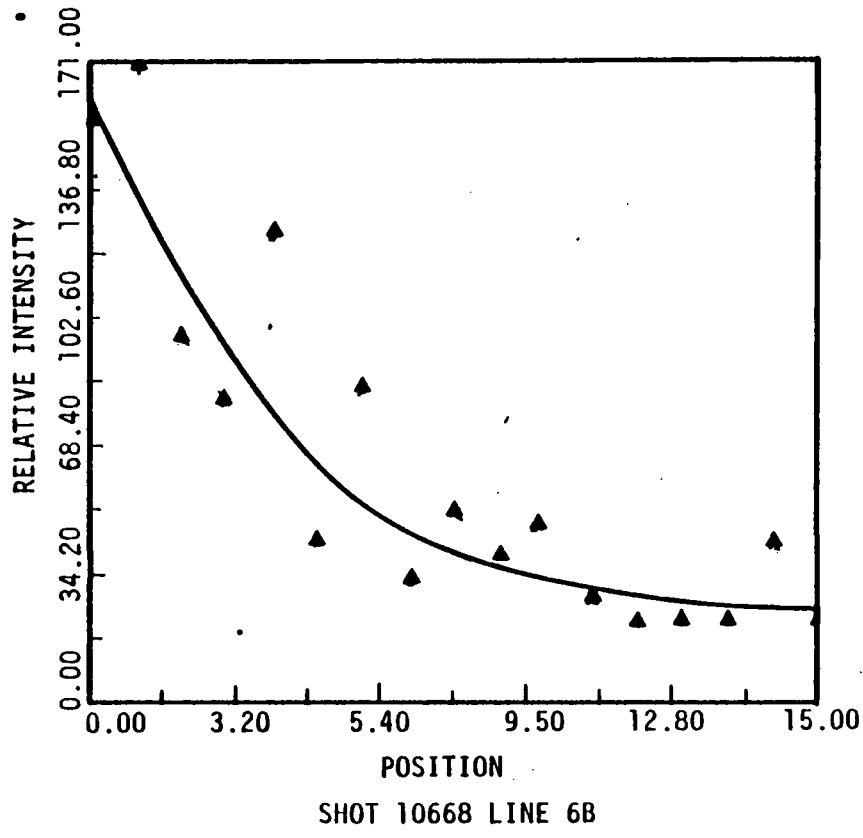

Figure III.5. Top and bottom relative intensity data and polynomial fit to data

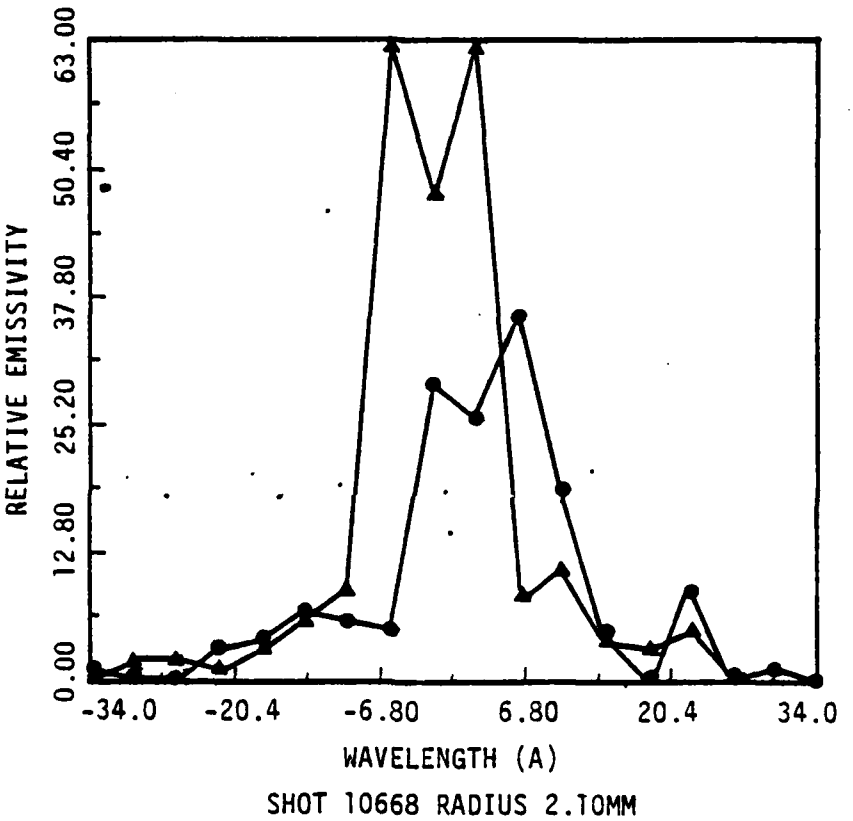

Figure III.6. Results of Abel inversion depicting line profiles for top and bottom at a radius of 2.1mm.

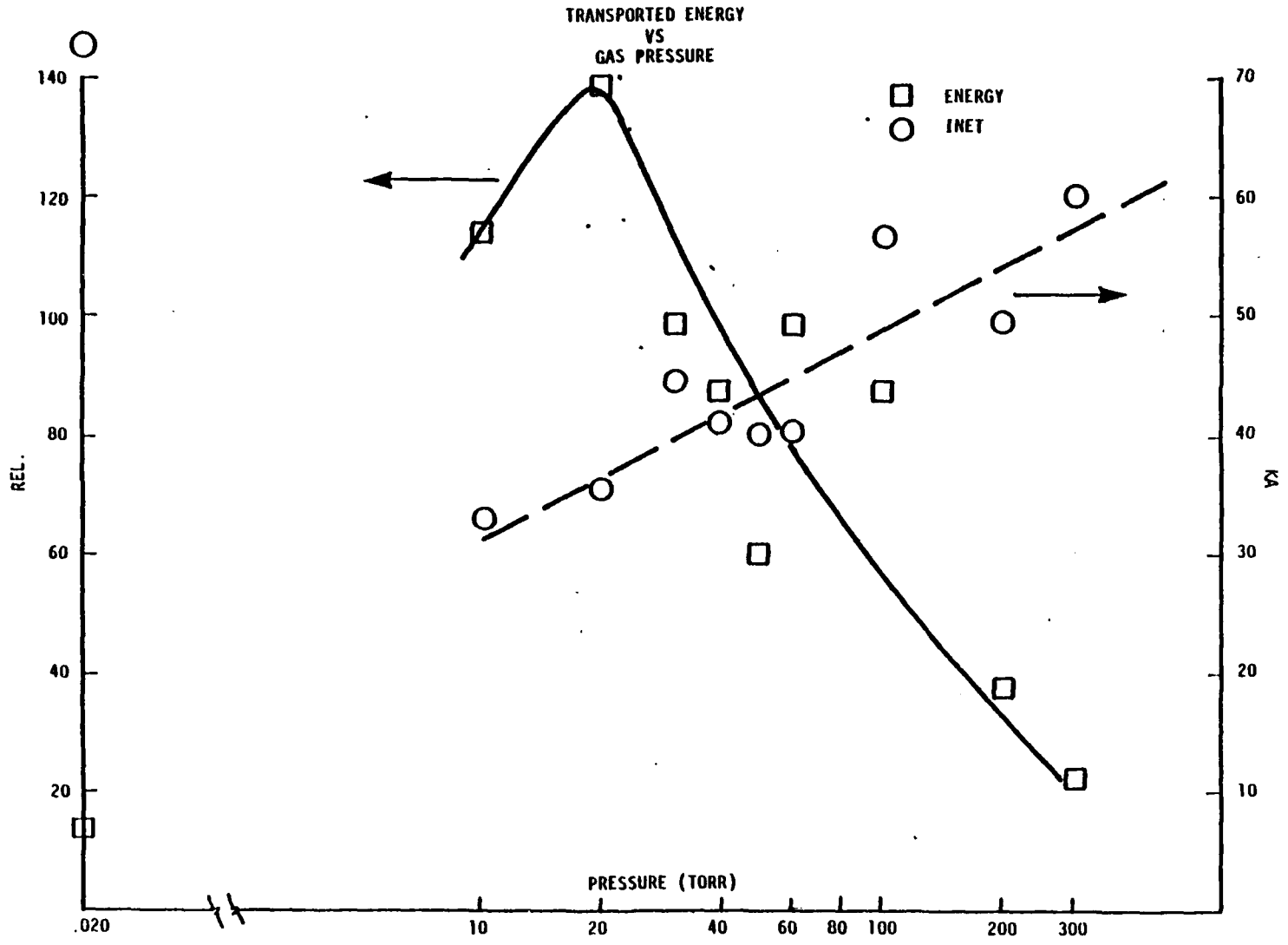

Figure III.7. Transported energy and net current as functions of H_2 fill pressure

neutralization, as one would expect, since collision rates (and therefore, resistivity) are increasing with density. The peak in transported energy is consistent with the physical picture of a transition to quasi-stable pinched beam propagation as the current neutralization falls below the charge neutralization, allowing self-fields to create radial forces. This interpretation is substantiated by the H_β records, which show plasma diameters of approximately injection size (Figure III.8) for pressures below 20 torr, and diameters less than 1 cm for pressures of 20 torr and higher.

Finally, the results of the Stark-broadened profile analysis for the 20 torr shot are shown in Figure III.9. Although there is significant scatter in the interpreted densities, one may infer a peak density of slightly greater than 10^{16} electrons/cm^3, or about 1 percent of the hydrogen atom number density for a room temperature fill of 20 torr. Similar values of peak n_e were obtained up to 100 torr, after which the line intensities were too low to allow quantitative analysis.

Although the analysis technique described above usually produced believable electron density estimates, there were cases for which the Abel-inverted H_β line profiles bore little or no resemblance to any realistic profile. This was especially true in the line wings and plasma boundaries where intensities were low and signal-to-noise ratios poor. It has recently been suggested that an improvement in the Abel inversion can be achieved by using a cubic spline fit minimizing variations in the first derivative for the spatial intensity data rather than using a polynomial fit [9]. It may be, however, that these experiments are inherently azimuthally nonuniform and, therefore, inappropriate for Abel inversion at all [10]. Perhaps, in this case, the superposition of data from many cumulative shots could be used to obtain average density profiles. Further details of the work in this section are presented in Reference [11].

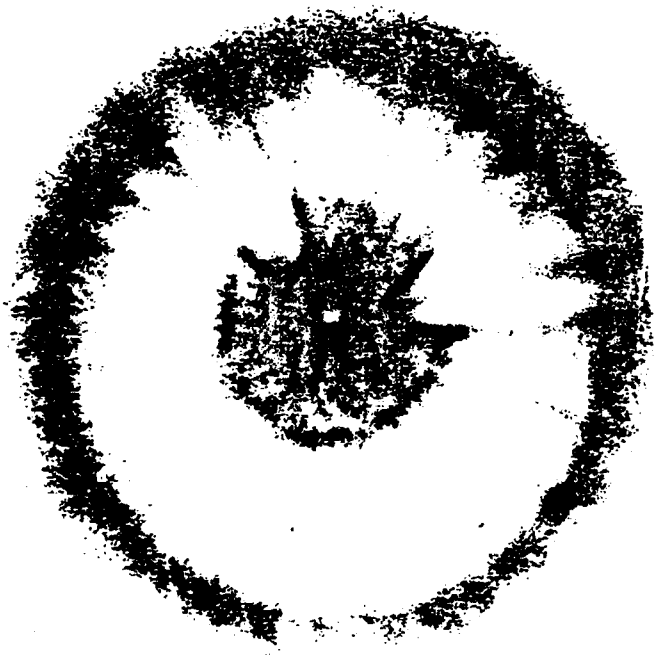

Figure III.8. Contact print of anode witness f il.

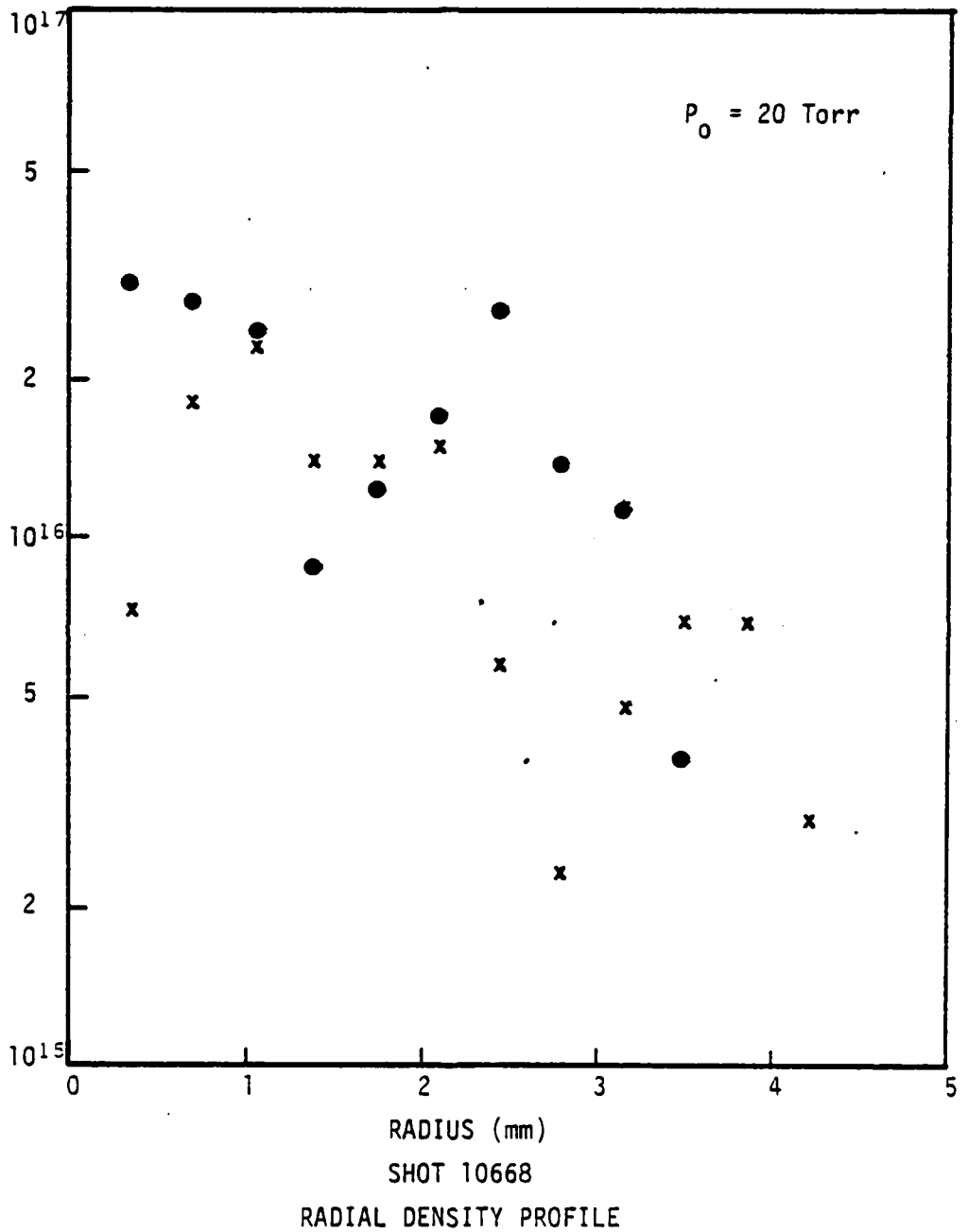

Figure III.9. Top (x) and bottom (●) radial density profiles interred from Abel inverted relative H_3 intensity data for 20 torr shot.

SECTION III REFERENCES

III. 1. Clark, M. C., "Transport and Stability of a Magnetized Electron Beam Propagating through Neutral Gas," Bull. Am. Phys. Soc. 25, 913 (1980).

2. Griem, H. R., Plasma Spectroscopy, McGraw-Hill, Inc., New York, (1964).

3. Griem, H. R., Spectral Line Broadening of Plasmas, Academic Press, New York, (1974).

4. Wiese, W. L., Pagnette, D. R., and Solarski, J. E., Phys. Rev., 129, 1225 (1963).

5. Huddlestone, R. H., and Leonard, S. L., editors, Plasma Diagnostic Techniques, Academic Press, New York, (1965).

6. Lochte-Holtgreven, W., editor, Plasma Diagnostics, North-Holland Publishing Company, Amsterdam, (1968).

7. Bevington, P. R., Data Reduction and Error Analysis for the Physical Sciences, McGraw-Hill, Inc., New York, (1969).

8. See, for example, integrals 190 and 191 in Standard Mathematical Tables, 18th Student Edition, published by the Chemical Rubber Company.

9. Kuthy, A. Nucl. Inst. and Meth., 180, 7 (1981).

10. Kuthy, A. P. G., J. Appl. Phys., 50, 6139 (1979).

11. Kiuttu, G. F., "Spectroscopy of High Density Plasmas," Ph.D. dissertation, University of New Mexico, 1984.

LIST OF FIGURES

LIST OF TABLES

IV. Space and Time Resolved Spectroscopy of High Energy Density Aluminum Plasmas

G. F. Kiuttu and D. Woodall

A. Introduction

Development of a laboratory source of intense x-rays suitable for nuclear weapons effects simulation is a high priority for Air Force sponsored research. Such a source must be a very high energy density plasma. It has become increasingly evident that a thorough understanding of the complex nature of plasmas is required to assemble them in a fashion which results in a high-power radiation burst.

Although theoretical models of plasma behavior have been developed from physical principles, they have had limited success in predicting laboratory plasma behavior. As a result, plasma diagnostics have become indispensable, both as a means of obtaining empirical information about real plasmas and as a means of substantiating or disproving theoretical and calculational models.

Plasma radiation diagnostics, especially, have evolved to a position of paramount importance, since they involve measurements of the plasma at a distance. Other diagnostics either require insertion of a perturbing probe directly into the plasma (clearly unacceptable for physically small, highly transient) or yield only electrical information, such as current through, voltage across, or magnetic field near the plasma.

For inertial confinement, or simulation, plasmas with peak temperatures of about 10^6 to 10^7 K, much of the radiation is emitted at wavelengths corresponding to the characteristic plasma energy, placing it in the soft x-ray portion of the spectrum (~1 Å to 100 Å, or ~100 eV to 10 keV). With a suitable model for radiation emission and transport, x-ray spectroscopy can yield estimates of the temperature and density of the plasma source. These two quantities are of fundamental importance in evaluating the effectiveness of any plasma assembly scheme.

Fortunately, much effort has been concentrated in the area of plasma spectroscopy. Relatively sophisticated collisional-radiative (CR) models have been developed [1-19] to account for experimentally observed spectra in a consistent manner. As the calculations have become more refined, the degree of consistency has improved, but only to a limited extent. Whereas, ideally, one would integrally couple the radiation model to a detailed magnetohydrodynamic (MHD), particle-in-cell (PIC), or other complete temporal and spatial simulation of the plasma, the magnitude of such an endeavor with existing computing capability renders it impossible. Instead, instantaneous, or steady-state, radiated power spectra are usually calculated assuming a uniform temperature and density for a single elemental species in a simplified (usually one-dimensional) geometry. The shortcomings of this approach are obvious, as the laboratory plasmas of interest cannot be described in such a simplistic fashion.

Another reason for the differences between theoretically predicted and experimentally observed spectra is that because ICF (inertial confinement fusion) and simulation plasmas are physically small (<1 cm^3, and usually < 1 mm^3) and highly transient (<1 μsec, and often $\leq$ 1 nsec), the experimental spectra have necessarily been recorded time- and space-integrated. That temporal and spatial variations of temperature and density will significantly affect the spectral signature of a plasma can be seen by the following heuristic argument. Consider a blackbody radiator. The spectral output is given by the Planck function,

$$I_\lambda(\lambda) = 2\ hc^2\lambda^{-5}[\exp(hc/\lambda kT) - 1]^{-1}\ , \qquad (1)$$

where I_λ is the energy radiated per unit time t, per unit area A, per unit solid angle Ω, per unit wavelength λ. h is Planck's

constant; c is the speed of light; and k is Boltzmann's constant. If one assumes that temperature is an arbitrary function of time, T(t), the time-averaged spectral output over the time interval $\Delta t = t_2 - t_1$ is given by

$$\bar{I}_\lambda = \frac{1}{\Delta t} \int_{t_1}^{t_2} dt' \; I_\lambda(\lambda, t')$$

$$= \frac{2hc^2}{\Delta t \lambda^5} \int_{t_1}^{t_2} dt' \{\exp[hc/\lambda kT(t')] - 1\}^{-1} . \qquad (2)$$

In general, Equation (2) represents a different spectral (λ) dependence from the original Planck function, and there is no <u>a priori</u> reason to believe that the time-averaged function

$$\frac{1}{\Delta t} \int_{t_1}^{t_2} dt' \; I_\lambda(\lambda, t')$$

will resembly $I_\lambda(\lambda, t)$ for any "average" value of T.

K-shell spectra of highly-ionized (one and two electron) aluminum (Z = 13) plasmas have routinely been recorded [20-25] on photographic film (Figure IV.1) using convex curved crystal (de Broglie spectrographs [26-28]. Dispersion relations for radiating point sources have been derived by Henke and Tester [29] and Burns [30], and for extended sources by Kastner [31], Kiuttu [32], and Gersten and Rauch [33]. For aluminum K-shell measurements (5 to 8 A), KAP (potassium acid pthalate) crystals (2d = 26.6 A) are normally used. Their reflectivity and rocking curve (spread in reflected angle from a point source) [34,37] have been measured. Recording films have been Kodak Medical No Screen [38], Kodak RAR 2490 [39], and, more recently, Kodak RAR 2497 [40] and Kodak RAR 2492 [41].

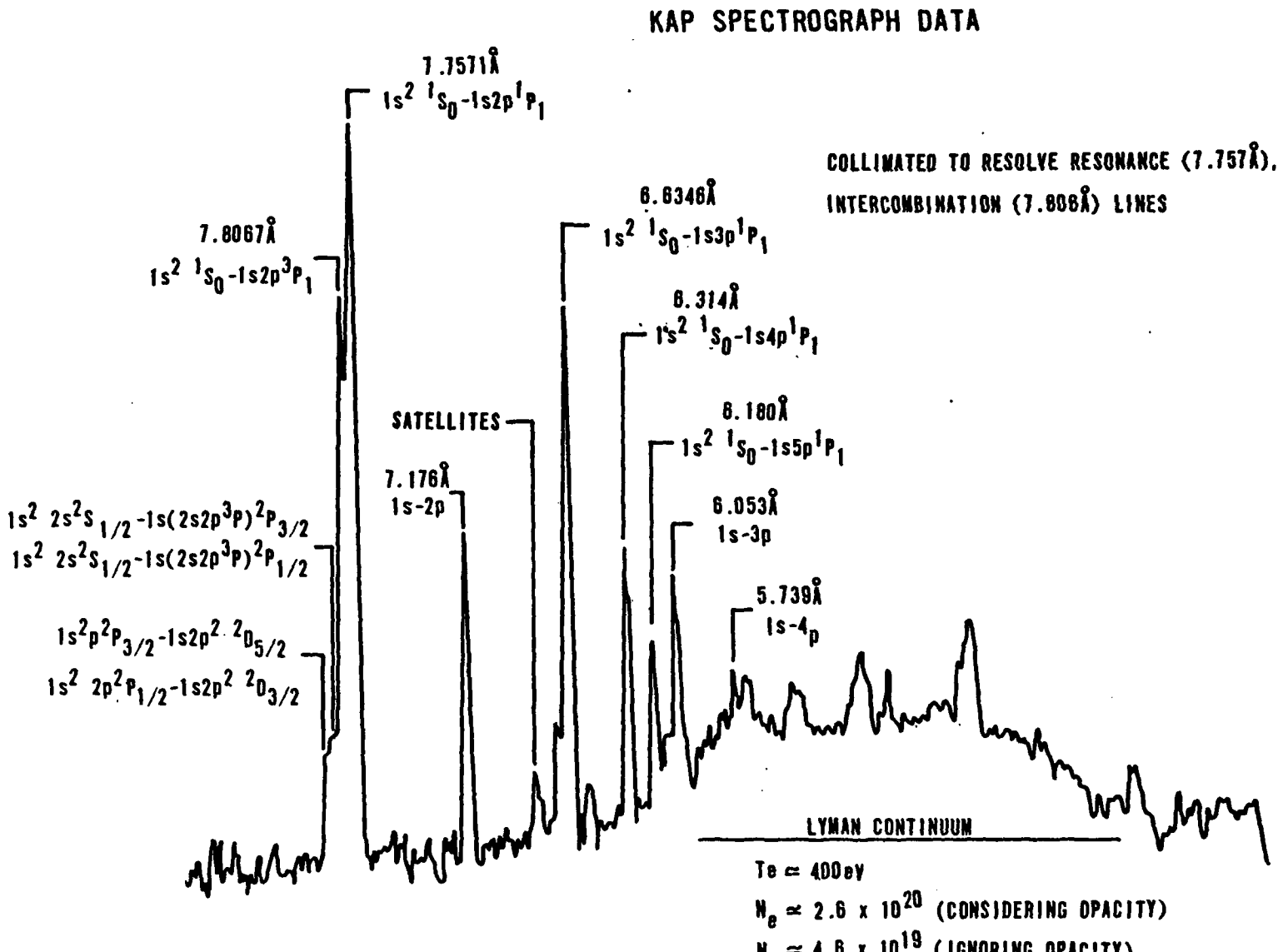

Figure IV.1. KAP curved crystal spectrograph record.

Recently, Duston, et al. [17], have shown that temperature and density estimates from the slope of the recombination continua and various line ratios for plasma with spatial gradients are suspect. They have also shown [13] that density estimates based on the ratio of the helium-like intercombination line ($1s^2$ - $1s2p\,^3P$) to resonance line ($1s^2$ - $1s2p\,^1P$) intensities are highly sensitive to opacity effects [42,43]. It may be concluded, then, that to correctly diagnose plasma temperatures and densities, the spectroscopy must be performed with both temporal and spatial resolutions. In addition the plasma radiation model calculations must be able to include plasma attenuation of its radiation (opacity) and arbitrary temperature and density distributions in realistic geometries.

The objectives of the present study were to demonstrate two-dimensional space-resolved soft x-ray spectroscopy of hot, dense, aluminum plasmas formed in the Air Force Weapons Laboratory's SHIVA electromagnetic implosion device [42-44], and to evaluate methods of obtaining detailed time-resolved spectra of these plasmas. The remainder of this report is organized as follows. In Section B, we describe the "dispersion imaging" technique [33,45-47]; we present data and results employing this technique in Section C; we describe several approaches to time-resolved spectroscopy in Section D; and finally we summarize in Section E.

B. Two-Dimensional Space-Resolved Spectroscopy

Conventional diffraction for a monochromatic point source and convex curved Bragg crystal, such as used to generate the spectrum of Figure IV.1, is shown in Figure IV.2. Diffraction for crystals is governed by the familiar Bragg relationship,

$$n\lambda = 2d \sin \theta \,, \tag{3}$$

where $n = 1,2,3,\ldots$ is the diffraction order, λ the wavelength, d the lattice spacing of the crystal ($2d = 26.6$ Å for KAP), and θ is the angle of incidence and reflection with respect to the surface tangent.

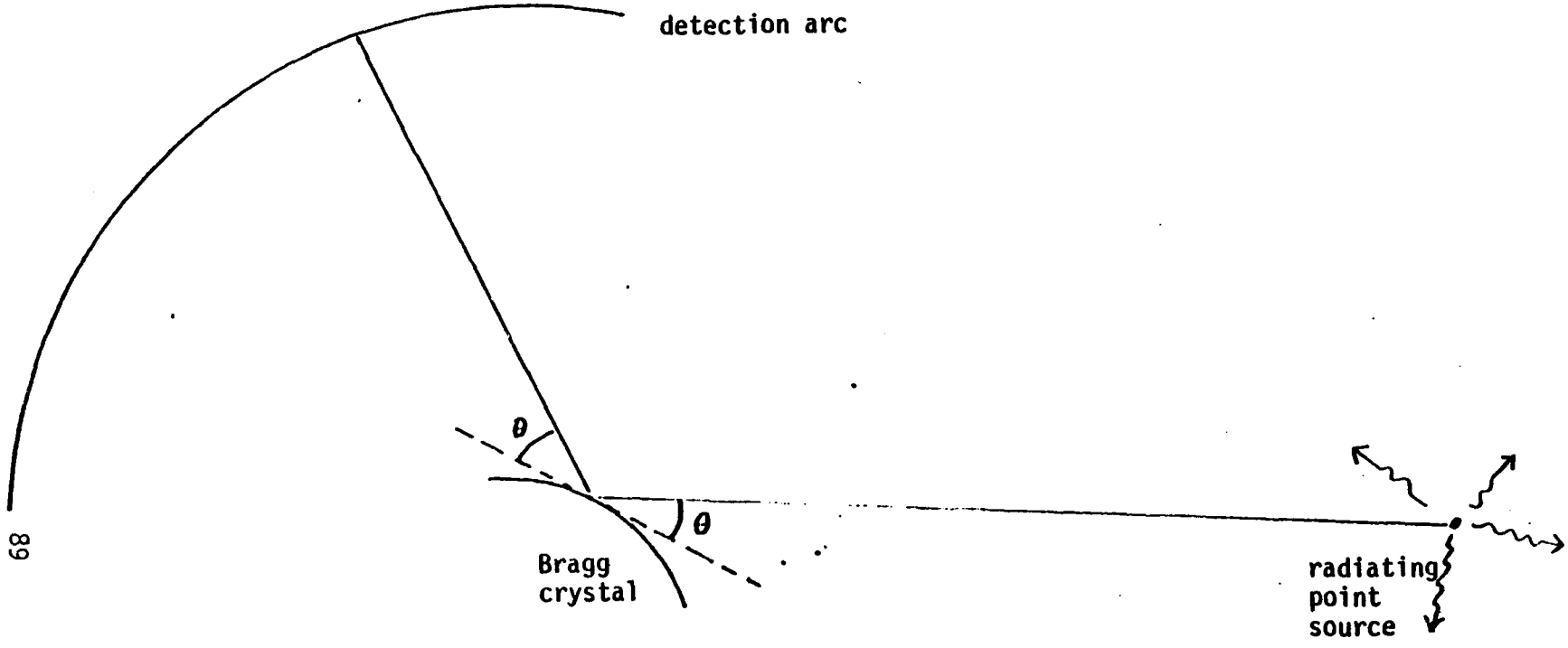

$$n\lambda = 2d \sin\theta$$

Figure IV. 2. Monochromatic point source, curved crystal Bragg diffraction.

If the monochromatic source is finite in extent, application of Equation (3) for the appropriate geometry results in a spreading of the image in the dispersion direction, as shown in Figure IV.3. Whereas this finite source size broadening is deleterious for line profile analysis [48] and density estimation from series mergence [33,49-54], it can be used advantageously when all other broadening mechanisms (for example, Stark and Doppler effects) are comparatively small. Then, for monochromatic radiation, the source emissivity is mapped one-to-one in the dispersion direction along the film arc.

The derivation of the general dispersion relation for extended sources and convex curved crystals is found in Reference [32]. Figure IV.4, a plot of film image location versus source displacement for two different wavelengths and three source-to-crystal distances for a typical KAP spectrograph demonstrates the linearity of the mapping. The dispersion magnification ($\Delta\ell/\Delta a$) is plotted as a function of wavelength for a source-to-crystal distance of one meter in Figure IV.5. Figure IV.6 shows the film arc location as a function of wavelength for the special case of a point source with no transverse displacement. All three figures are plotted for a KAP crystal with 2.54 cm radius of curvature mounted tangentially to the line drawn between source center and film arc center. The film arc radius is 5.73 cm.

In order for dispersion imaging to work, the spectral line width due to dispersive mapping of the source must be much greater than the width due to all other broadening mechanisms: natural line width, crystal rocking curve broadening, Doppler (thermal) broadening, and Stark (pressure) broadening. Stark broadening of the aluminum lines of interest at plasma temperatures of about 100 eV and electron densities below about 10^{22} cm^{-3} is negligible [55], as is resonance broadening [56]. From

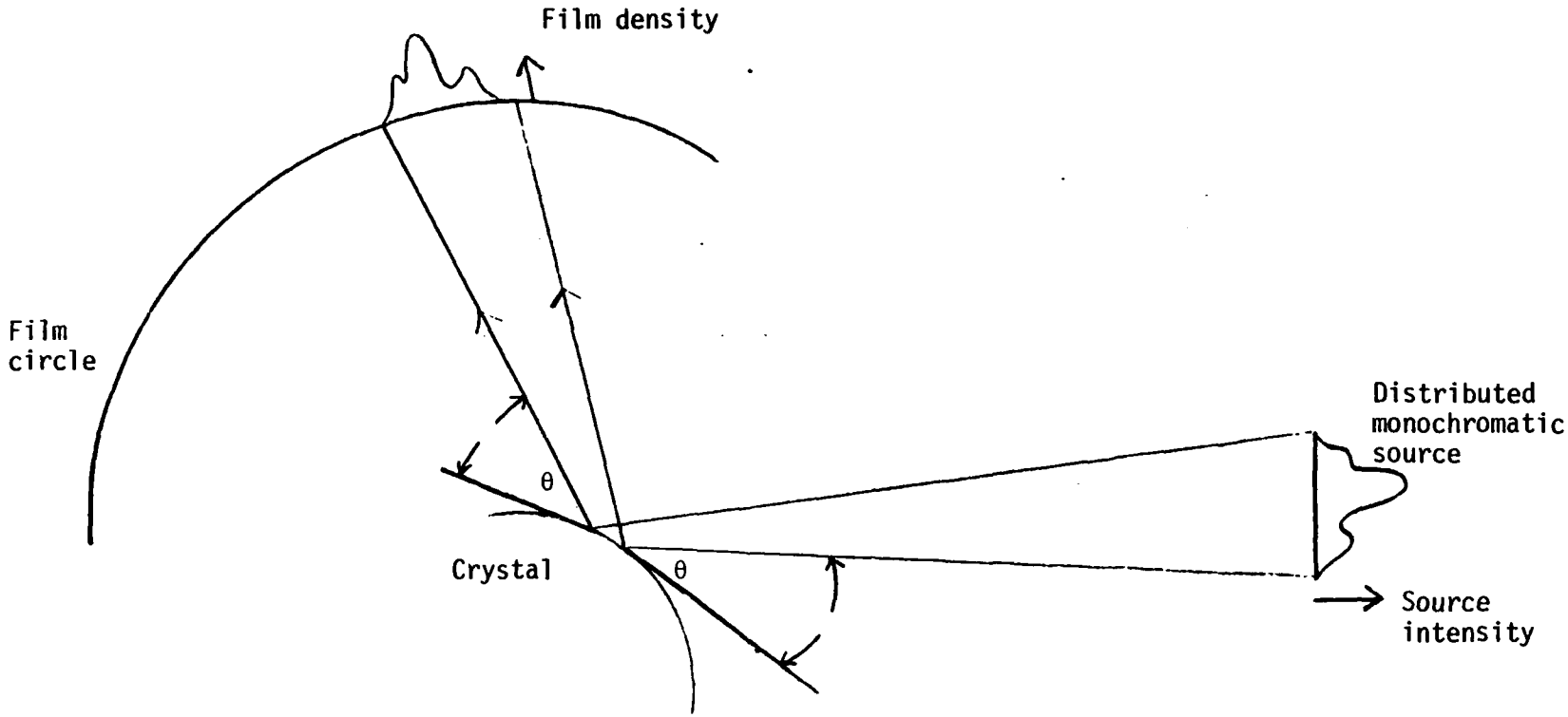

Figure IV.3. Curved crystal dispersion mapping.

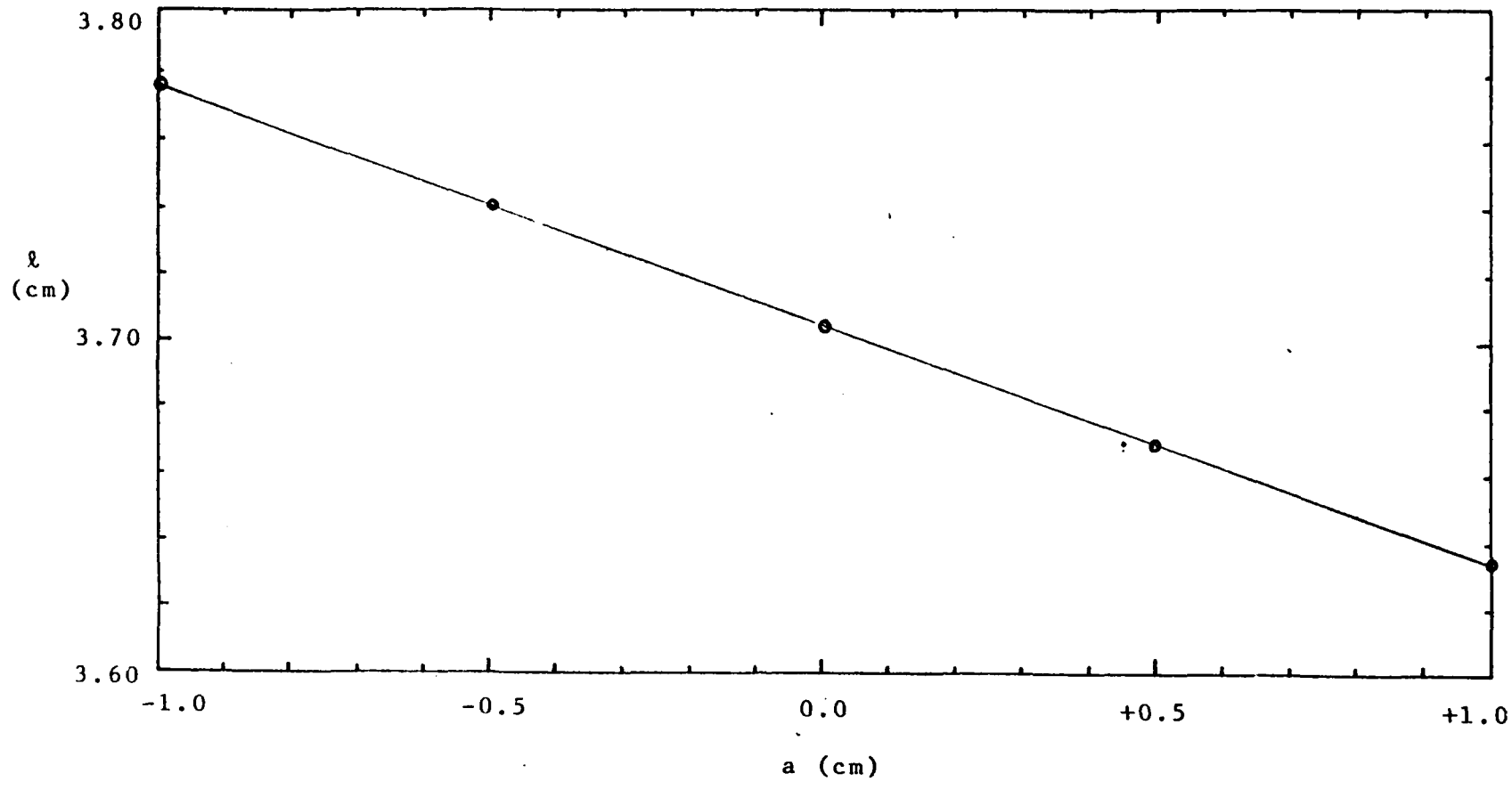

Figure IV.4. Film arc image location versus transverse source displacement for typical parameters.

AD-A138 872 PHYSICS OF HIGH TEMPERATURE DENSE PLASMAS(U) NEW MEXICO 2/2
UNIV ALBUQUERQUE DEPT OF CHEMICAL AND NUCLEAR
ENGINEERING D M WOODALL JAN 84 AFOSR-TR-84-0124
UNCLASSIFIED AFOSR-79-0060 F/G 20/9 NL

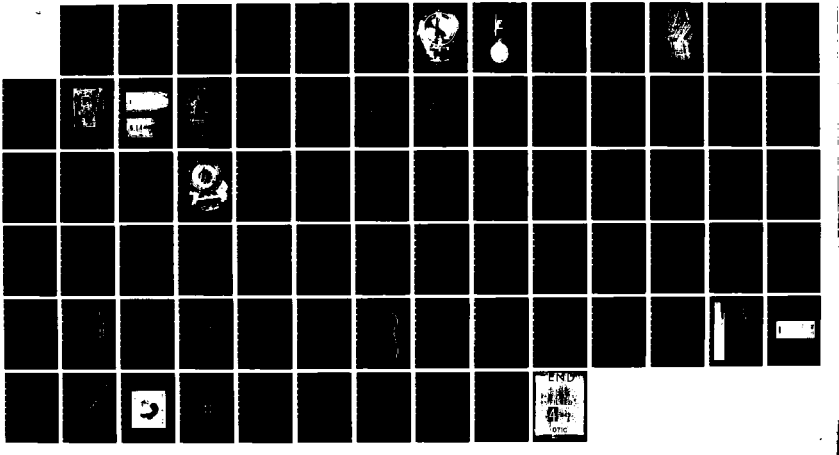

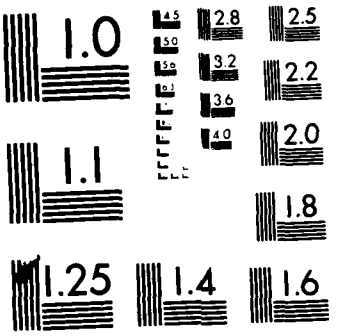

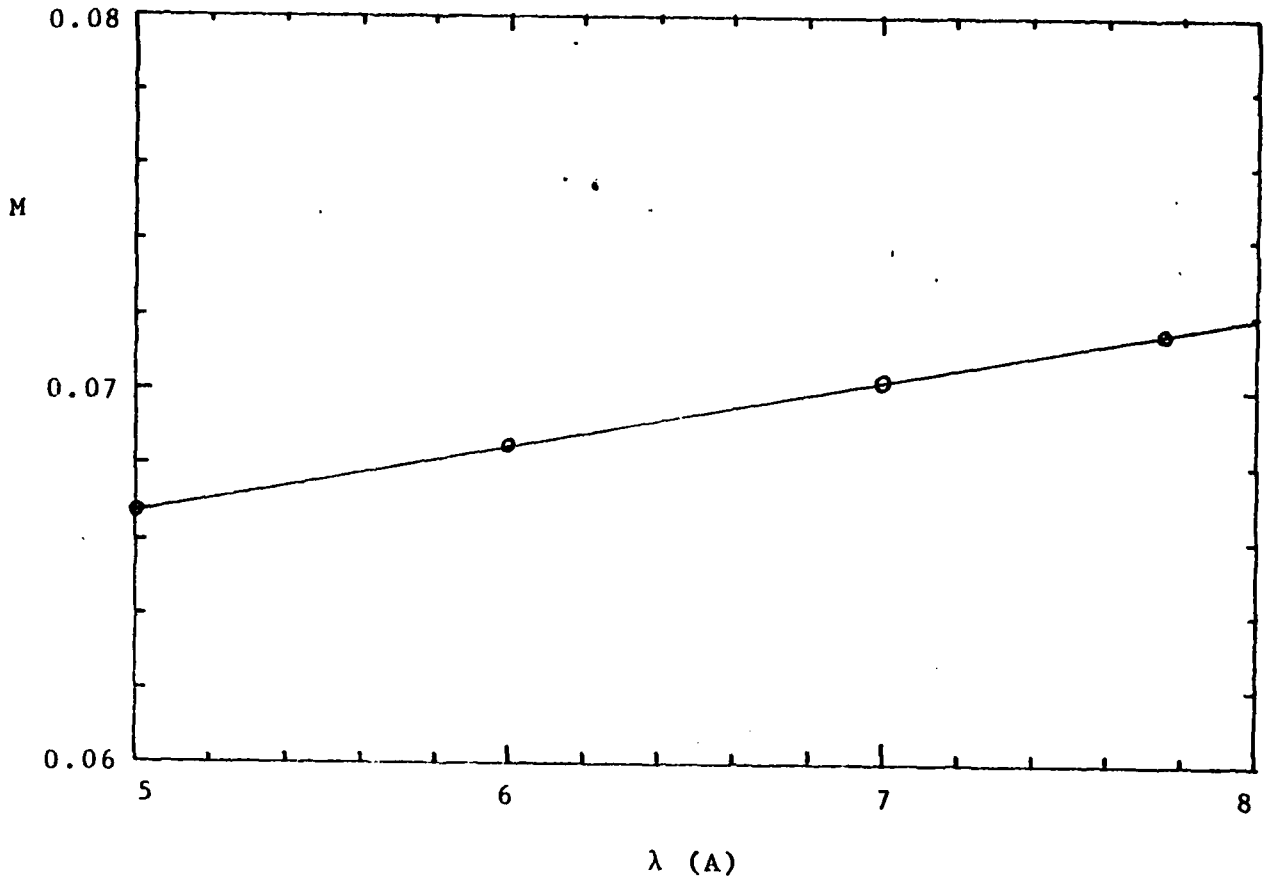

Figure IV.5. Dispersion magnification versus wavelength (L = 100 cm).

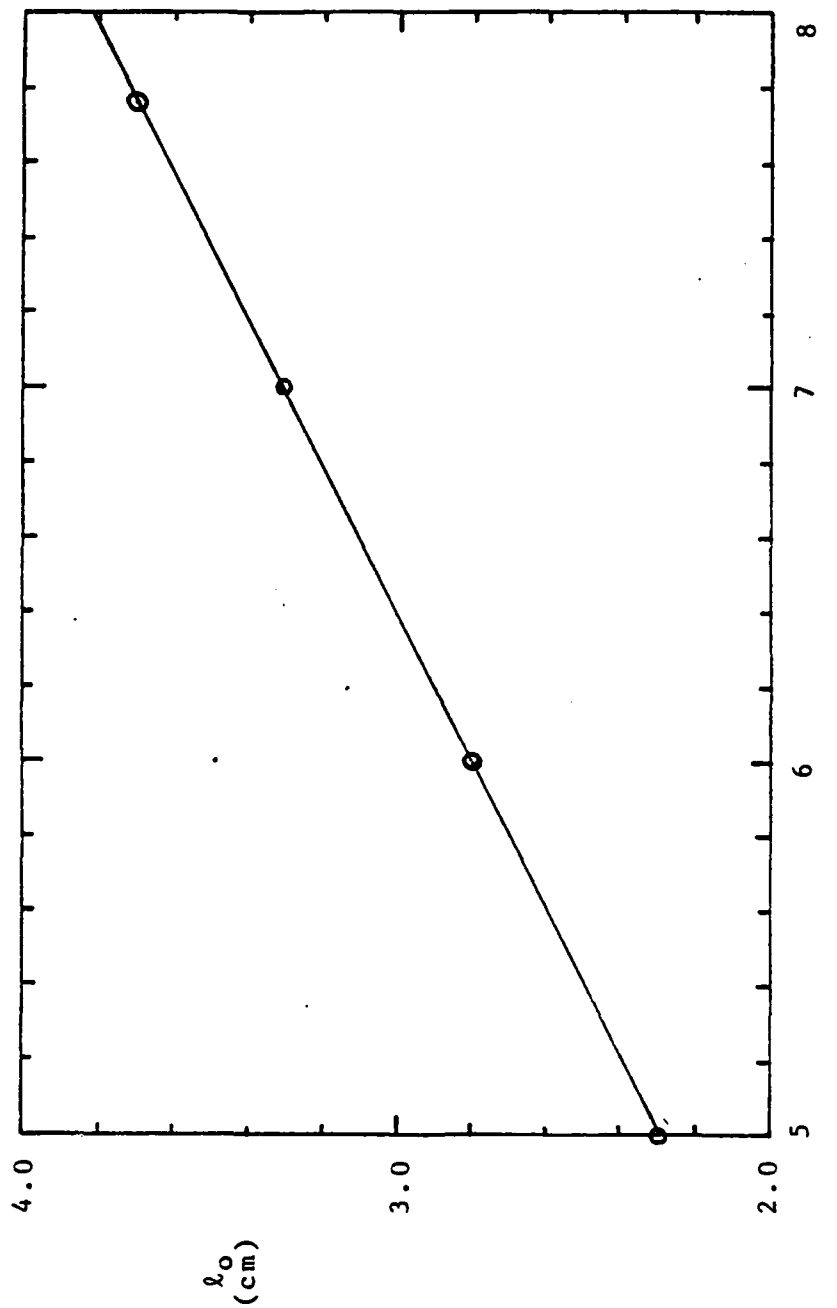

Figure IV.6. Film arc image location versus wavelength, no source displacement (L = 100 cm).

classical theory, the natural line profile is Lorentzian in frequency, with a FWHM in wavelength given by

$$(\Delta\lambda)_n = \frac{4\pi e^2}{3m_o c} , \tag{4}$$

or approximately 10^{-4} Å. Doppler broadening is Gaussian in frequency, and has a FWHM in wavelength given by

$$(\Delta\lambda)_D = \frac{2(\ln 2)^{1/2}}{c} \lambda_o \sqrt{\frac{2kT_i}{m_i}} , \tag{5}$$

where T_i and m_i are the ion temperature and mass, and λ_o is the central wavelength of the line. For a temperature of 100 eV and a wavelength of 8 Å, the FWHM is only about 10^{-3} Å, or from Figure IV.6, the film $\Delta\ell$ is about 5 μm. Opacity broadening results from self-absorption of a given spectral line by nonlocal ions of different temperature and/or density. Thus, the absorption profiles differ from the emission profiles. In particular for lines emitted in a hotter, denser core, the central portion of the line is preferentially absorbed by surrounding plasma, resulting in an effective broadening of the line [57]. No simple expressions exist for the magnitude of this effect, but high resolution spectroscopy suggests that for most lines of interest, it is not significant. Finally, the published value of the FWHM of the KAP crystal rocking curve [37], 3.4×10^{-4} radians, yields a spread of about 20 μm for a film arc radius of 5.73 cm. By comparison, a 1 cm diameter source at 100 cm would produce an image length on film of 714 μm at the helium-like resonance line wavelength 7.757 Å. Thus, the criteria for dispersion imaging are satisfied, and a spatial resolution of about 3 percent (due to the crystal rocking curve) is realized.

Spectrogaph image curvature aberration (due to path length differences for rays with components parallel to the crystal axis) has been evaluated and found to be insignificant. A derivation for a worst case (1/4-in. diameter crystal mounted concentric with the film arc) is presented in Appendix IV.B.

To achieve spatial resolution orthogonal to the dispersion direction, a simple imaging slit (one-dimensional pinhole) is placed between the source and crystal and oriented normal to the crystal axis. The slit-imaging optics are illustrated in Figure IV.7. The slit magnification, M_s, is seen to be

$$M_s = \frac{\ell_2}{\ell_1} , \tag{6}$$

and the relative geometrical resolution given by

$$\sigma_s = \frac{d}{a} \left(1 + \frac{1}{M_s}\right) . \tag{7}$$

For a slit width, d, of 100 μm, source size, a, of 1 cm, and M_s = 0.1, a resolution of 11 percent results, and can be reduced by decreasing the slit width or increasing the magnification. Note that at the wavelength of interest and slit widths >100 μm, diffraction effects are negligible.

The imaging spectrograph used in the present experiments is shown in Figure IV.8, with its crystal and mount, and slit/filter assembly. In normal operation, the spectrograph housing is covered for operation in vacuo ($<10^{-5}$ Torr) to prevent attenuation of the soft x-rays by air in the system. A combination light-tight slit/filter assembly is mounted within the 5 cm diameter vacuum tube between the source and spectrograph housing. The filter consists of thin Kimfoil or Formvar plastic or

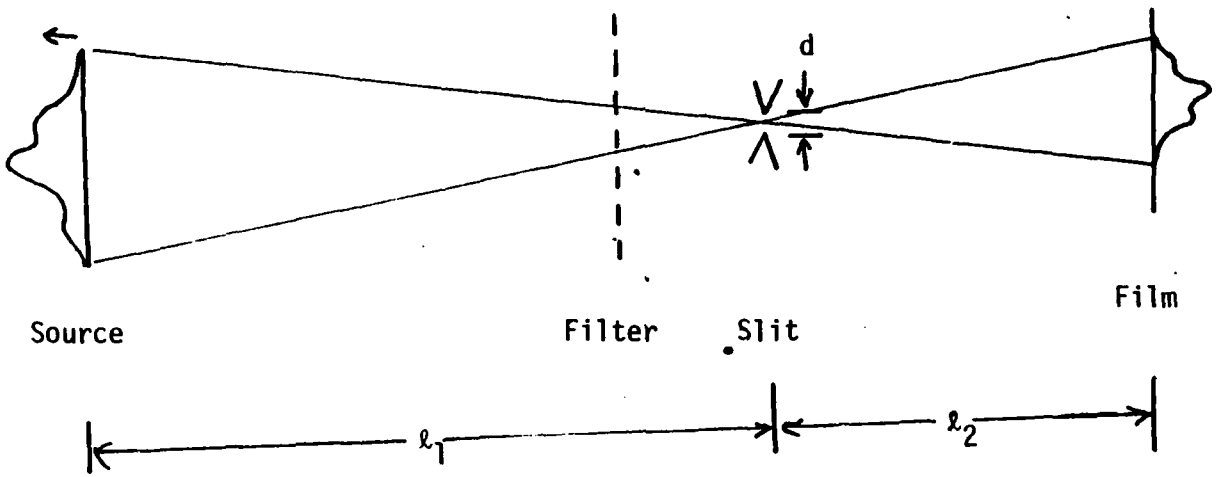

Figure IV.7. Slit-imaging optics.

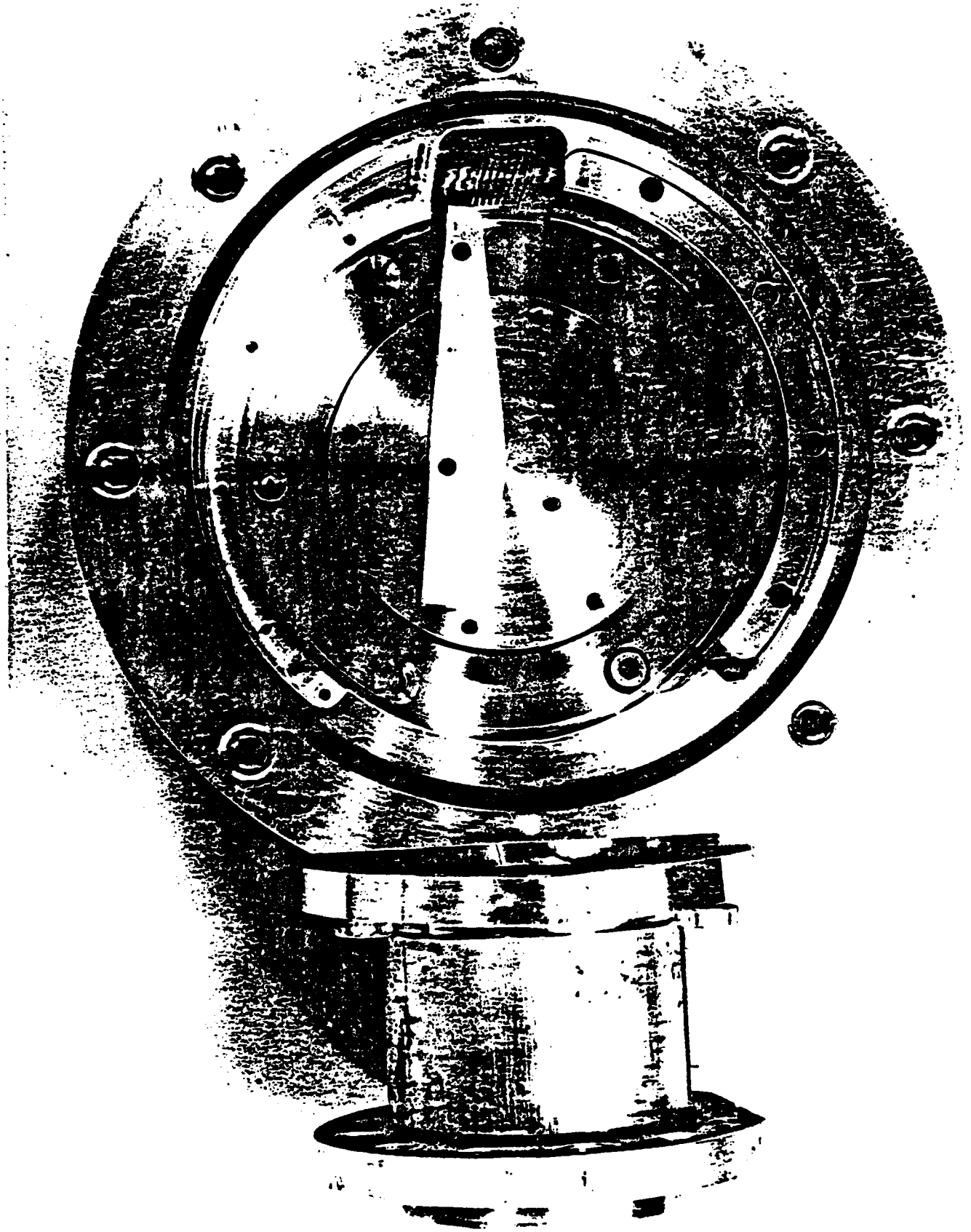

Figure IV.8(a). KAP curved crystal dispersion imaging spectrograph.

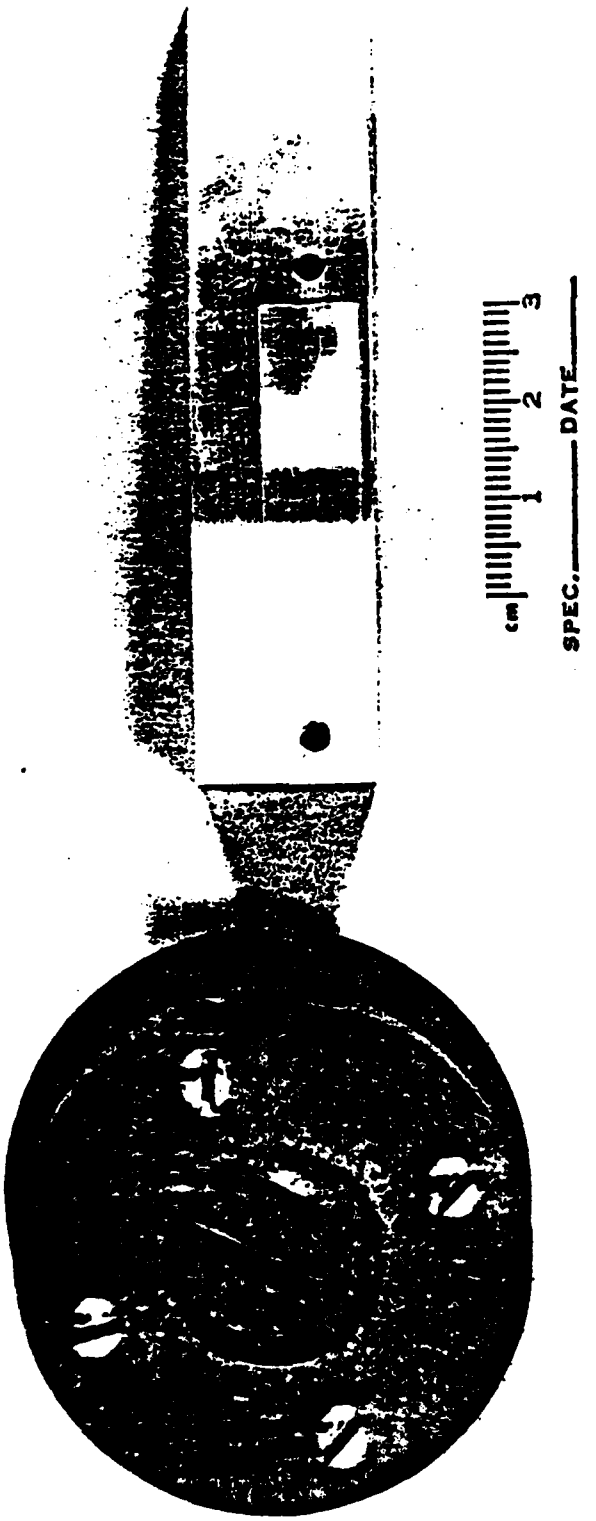

Figure IV.8(b). Imaging slit/filter assembly and mounted crystal.

polyamide (Kapton) with a 1000 thick vacuum vapor-deposited layer of aluminum to block visible light. A typical filter x-ray transmission function is shown in Figure IV.9. The KAP crystal is approximately 500 μm thick and 1 to 1.25 cm wide and is mounted on a 20° of arc 2.54 cm radius of curvature aluminum form. The recording film is either Kodak RAR 2490 or Kodak Medical No Screen, (35 mm format), which slides into the curved film holder cassette shown at the top of the spectrograph housing in Figure IV-8(a).

C. Analysis and Results

Using the spectrograph and technique described in the previous section, several two-dimensional space-resolved spectra of AFWL SHIVA I' plasma sources were recorded. The plasmas were produced by discharging a fast capacitor bank (Figure IV.10) through an initially solid central load via low-inductance parallel plate transmission lines. In the first phase of the discharge, axial current flowing through the thin cylindrical foil load causes it to vaporize and then ionize, forming a low-temperature plasma. In the second phase, strong radial JxB forces accelerate the plasma toward the axis, converting stored electrical energy into kinetic energy. In the final phase, the plasma collides with itself on axis, rapidly thermalizes and emits radiation, with approximately 1 percent in hydrogen-like and helium-like aluminum K-shell radiation. Parameters for the SHIVA I' experiments are summarized in Table I.

Diagnostics routinely incorporated include x-ray photodiodes [58], x-ray pinhole cameras [59], thermocouple calorimeters, a fast pulsed bolometer [60], grazing incidence spectrographs [61], and electrical diagnostics (voltage and current) in addition to curved crystal spectrographs [62]. A schematic of the SHIVA diagnostic geometry is shown in Figure IV.11. A photo of the curved crystal imaging spectrograph installed below the load

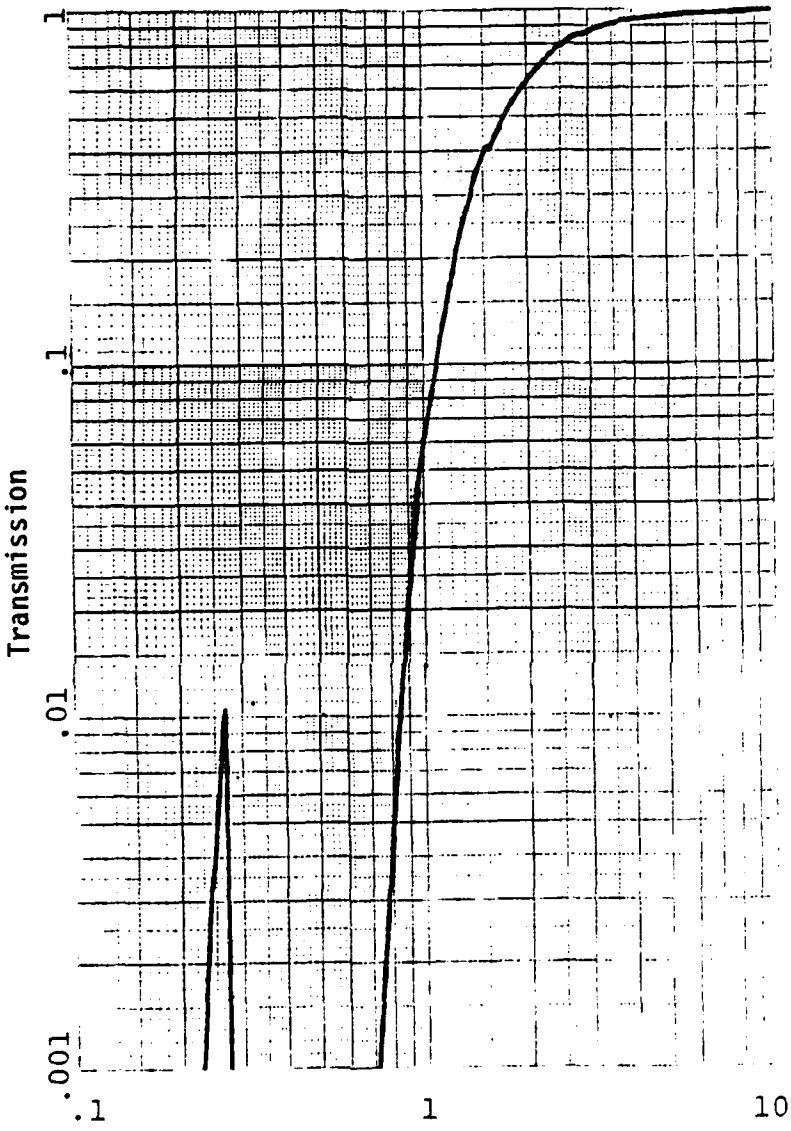

Figure IV.9. Al/Kapton filter transmission function.

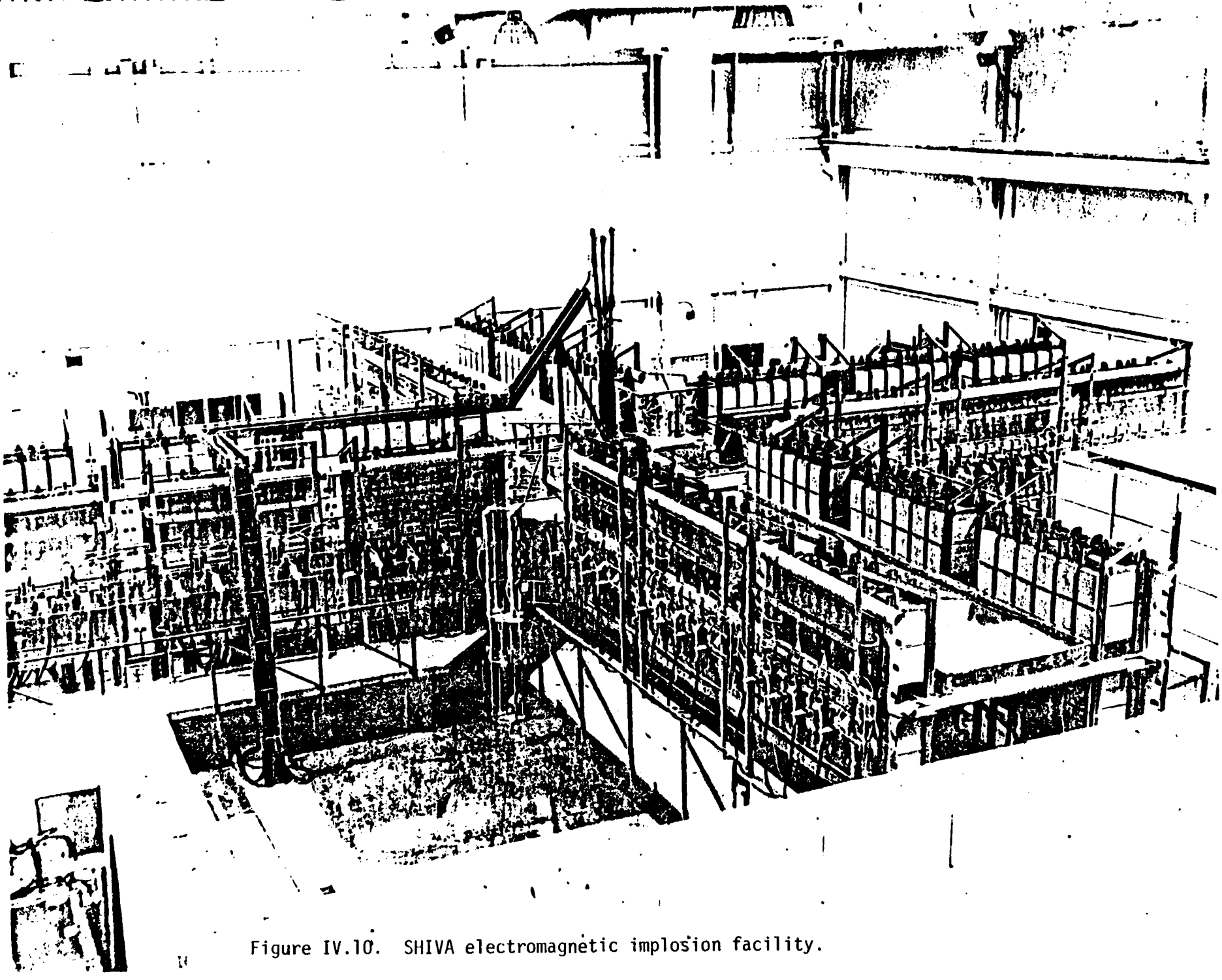

Figure IV.10. SHIVA electromagnetic implosion facility.

Table IV.1

SHIVA Parameters

Bank capacitance	266 f
Charge voltage	120 kV
Stored energy	1.9 MJ
Peak current	7-12 MA
Current risetime	1.4 sec
Load materials	aluminum, aluminum/plastic
Load radius	5-7 cm
Load height	2 cm
Load mass	30-300 $\mu g/cm^2$
Implosion time	1-1.5 μsec
Final velocity	15-22 cm/μsec
Kinetic energy conversion efficiency	15-25%
Radiation yield	100-240 kJ
Radiation pulse width	80-200 nsec
Peak radiated power	2 TW

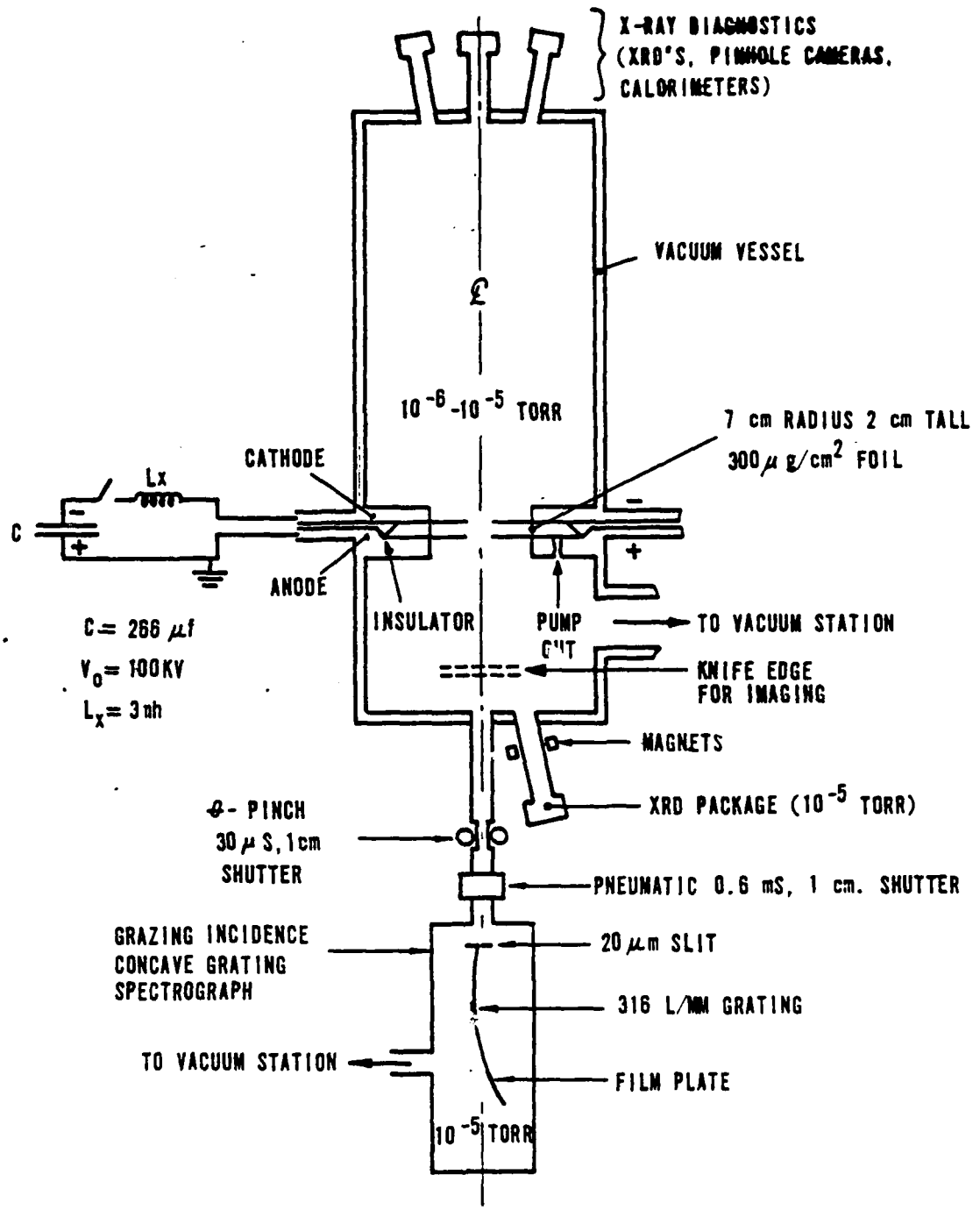

Figure IV.11. SHIVA diagnostic geometry with grating spectrograph.

chamber is shown in Figure IV.12. Because of the low inductance radial current feed geometry, diagnostic access was limited to the axial direction, and distances greater than about 1 meter.

Representative two-dimensional space-resolved aluminum K-shell spectra completely analogous to Figure IV.1 are shown in Figure IV.13. The plasmas, as viewed by the spectrograph, were roughly circular in shape. The elongated images are due to different magnifications (dispersion and slit) in the two orthogonal directions. Figure IV.13c, recorded on RAR 2490 film, shows overlapping of the helium-like resonance (1s - 1s2p P) and intercombination ($1s^2$ - $1s2p\,^3P$) lines and lithium-like satellite line. Also indicated by the figure is the annular emission pattern often observed in x-ray pinhole photos for these plasmas. Figure IV.14 shows a broadband (0.8 to 2 keV) x-ray pinhole photo of the plasma of Figure IV.13a. The maximum radius of the pattern is 1 cm, defined by the viewing holes in the planar implosion electrodes.

For the RAR 2490 records, the film was developed according to the recipe published by Benjamin, Lyons, and Day [39], and scanned with a microprocessor-controlled Perkin-Elmer diffuse microdensitometer. The optical density arrays were stored on magnetic tape and subsequently transferred to a PDP 11/60 disk file for interactive processing. The results of processing were estimates of time-integrated two-dimensional space-resolved temperatures and densities [63] of the plasma sources.

To obtain these estimates, the raw optical density arrays were first edited into separate files for each spectral line and recombination continuum, and corrected for background. Next, the optical densities were converted to areal energy densities at the film using the published film response [39]. Finally, relative source intensities were determined by correcting for wavelength-dependent crystal reflectivity (Figure IV.15) [64] and filter

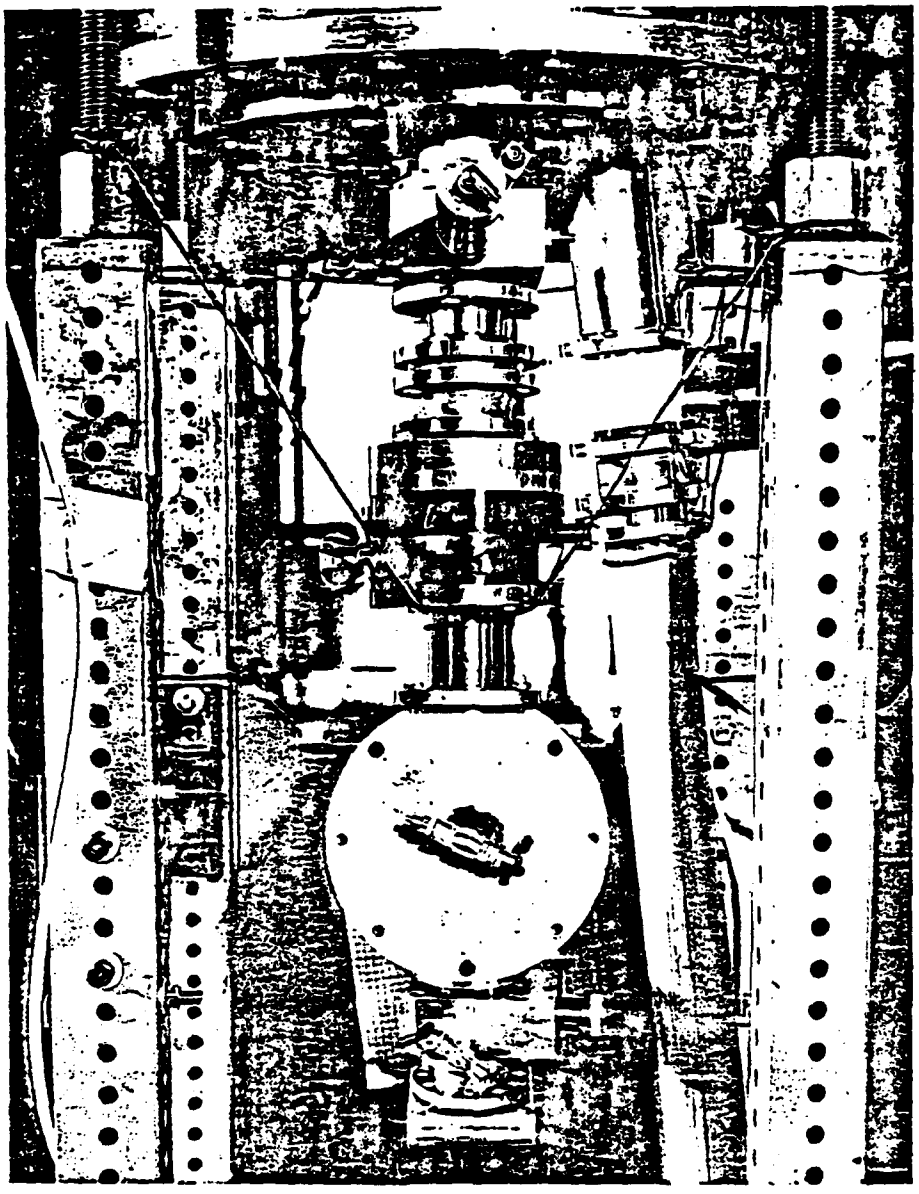

Figure IV.12. Installed curved crystal imaging spectrograph.

(a) Shot #4040

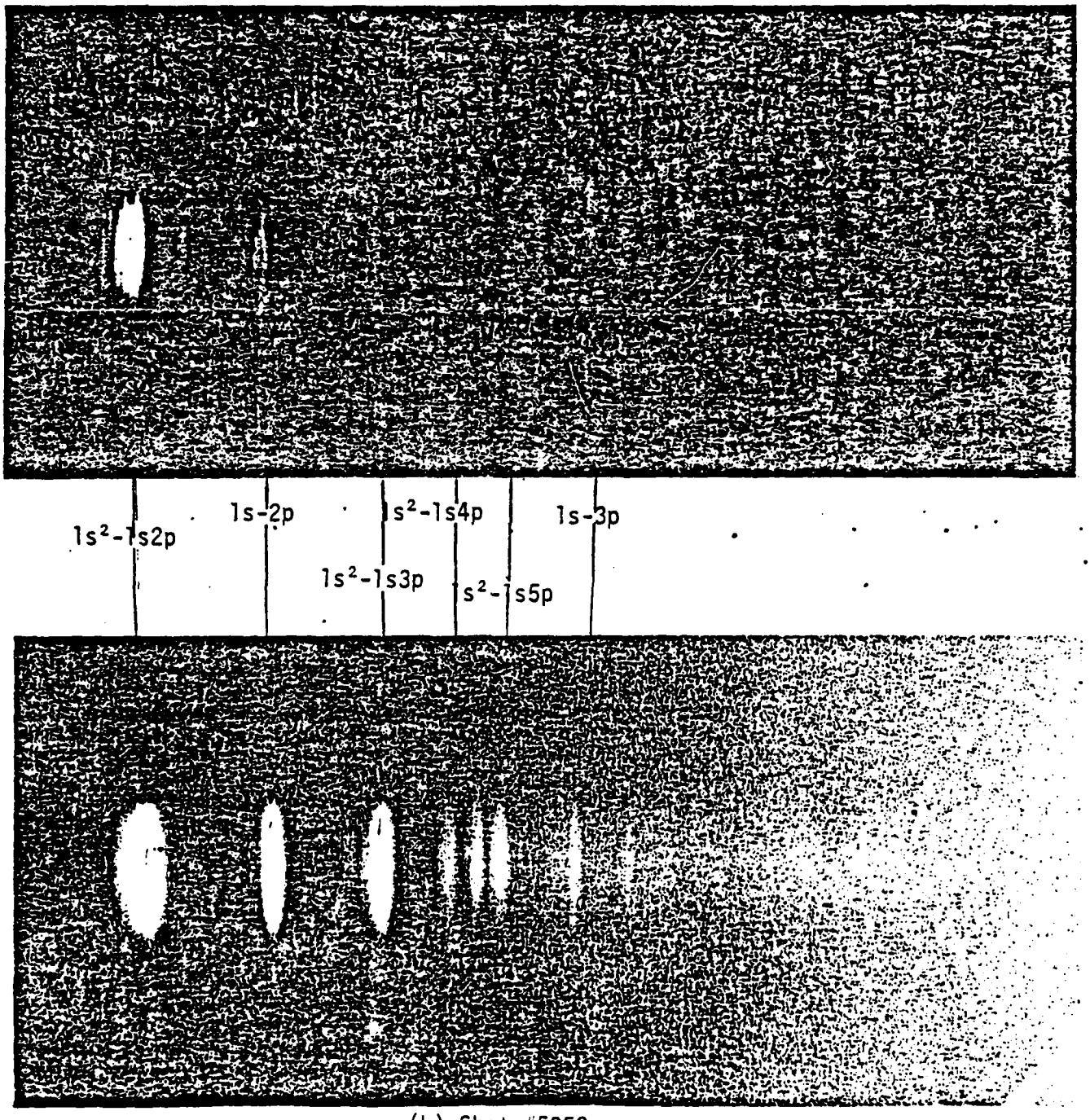

(b) Shot #5052

Figure IV.13. Space-resolved curved crystal spectrum: (a) Shot 4040 RAR 2490; (b) Shot 5052, Medical No Screen.

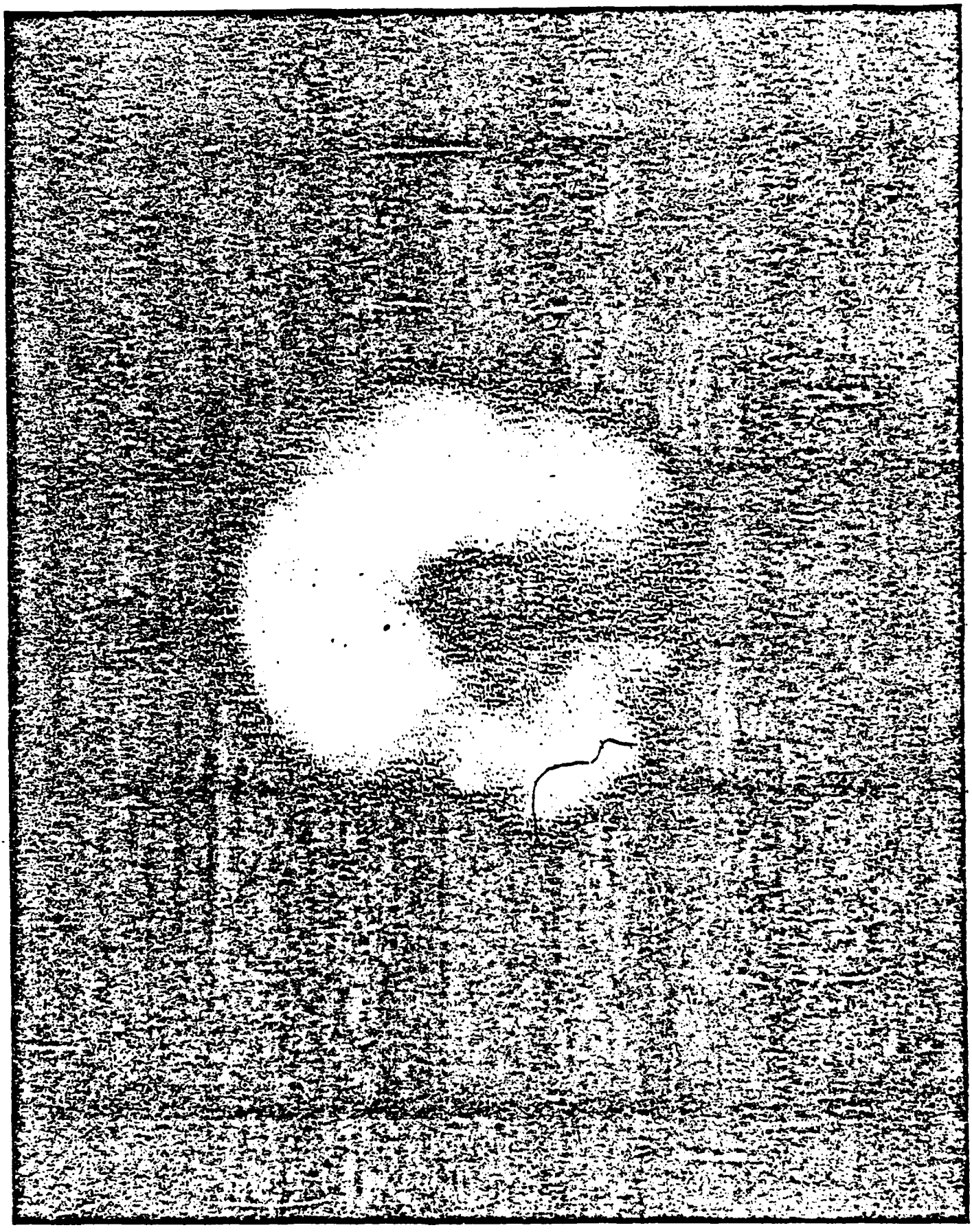

Figure IV.14. X-ray pinhole photo corresponding to Figure 13a.

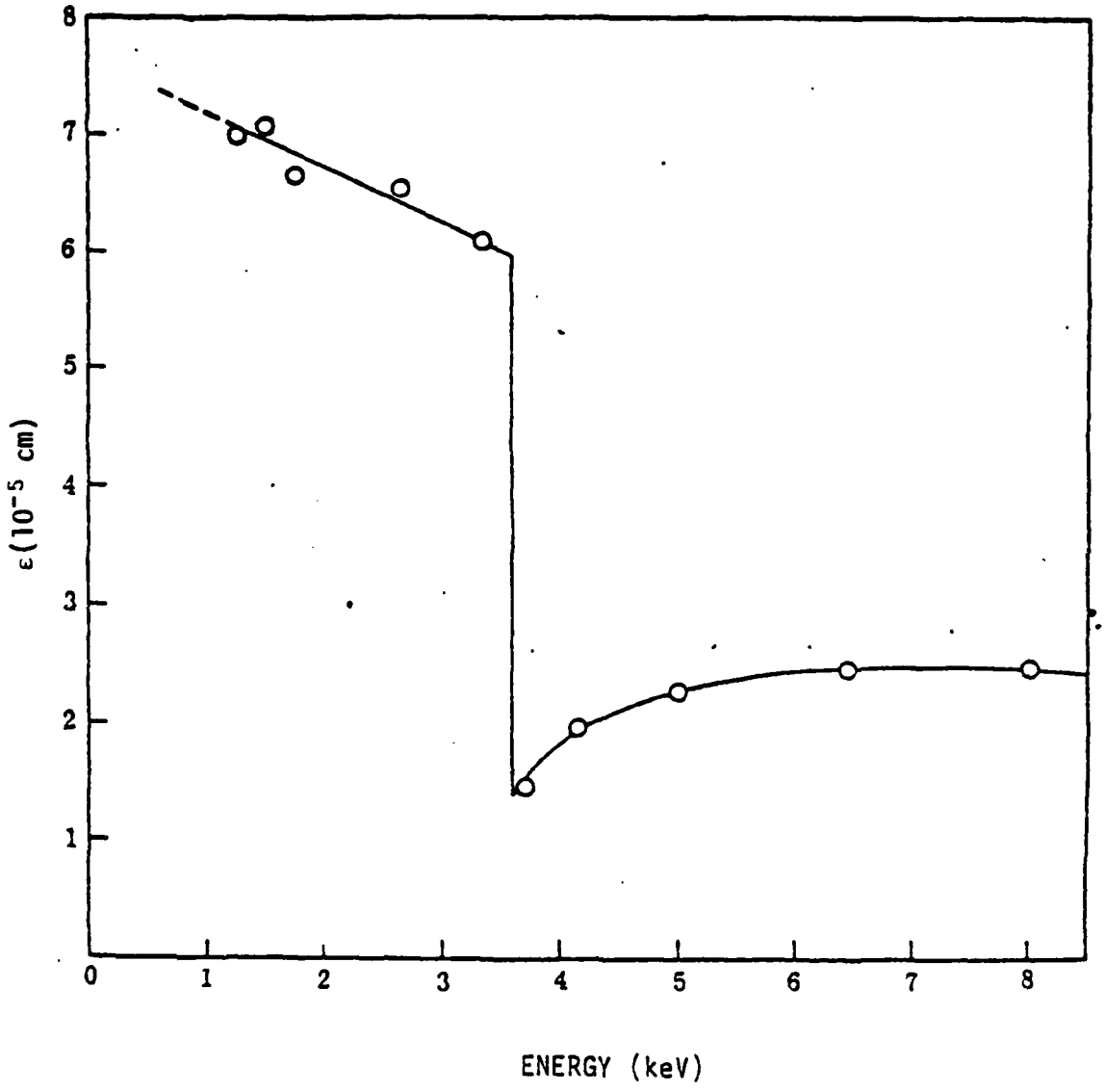

Figure IV.15. Curved KAP crystal integrated reflectivity [64].

transmissions. Relative source line intensities for the transitions $1s^2$ - 1s2p, 1s - 2p, and $1s^2$ - 1s3p of Shot 5052 are shown in Figures IV.16, IV.17, and IV.18, respectively. A one-dimensional representation of the overlap of the helium-like resonance line (7.757 Å), intercombination line (7.806 Å), and lithium-like satellite lines is shown in Figure IV.19; the lithium-like satellites are much lower in intensity than the resonance and intercombination lines.

If the helium-like intercombination and resonance lines are separated, or if the emission pattern is azimuthally symmetric or obtainable from other lines, one can estimate the plasma density from the intensity ratio [20,65]. By the latter technique, an "average" ion density for most of the data is in the range 10^{19} to 10^{20} cm^{-3} ($n_e \approx 10^{20}$ to 10^{21} cm^{-3}). It is possible to use the nonstandard 013 KAP diffraction planes [66] to completely resolve the resonance and intercombination lines.

As a first basis for evaluation, the lines $1s^2$ - 1s2p, 1s - 2p, $1s^2$ - 1s3p, and 1s - 3p were matched to the line ratios of Table II, supplied by D. Duston [67], based on optically thin CRE calculations. As expected, no consistent matching was possible, indicating that opacity effects must be important.

Next, the spectral line ratios versus density and temperature plots shown in Figures 6-14 of reference [11], which include opacity effects for uniform temperature and density spherical plasmas, were used. Due to the sparcity of these theoretical predictions for cases with nonnegligible opacity, we chose the predictions for one density ($n_i = 10^{20}$ cm^{-3}, or $n_e \approx 10^{21}$ cm^{-3} and thickness (500 μm) for the (1s - 2p)/($1s^2$ - 1s3p) and 1s - 2p)/($1s^2$ - 1s2p) ratios and compared these to our experimental line ratios. The temperature map obtained from the former ratio for Shot 5052 is shown in Figure IV.20. It is expected that a more realistic density distribution (peaked on axis with

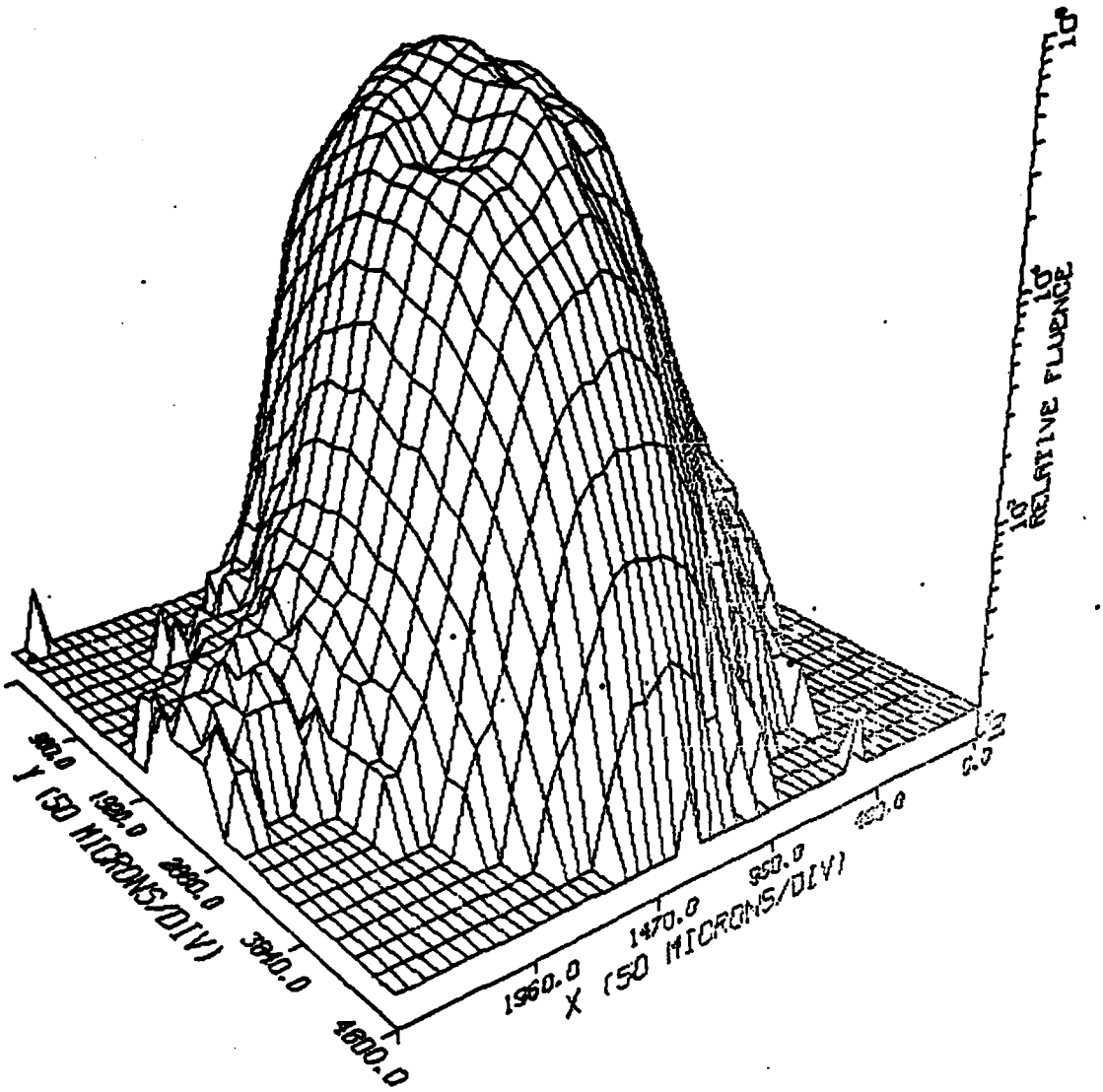

Figure IV.16. Shot 5052 helium-like resonance and intercombination lines ($1s^2$ - $1s2p(^1P)/1s^2$ - $1s2p(3p)$) with lithium-like satellites.

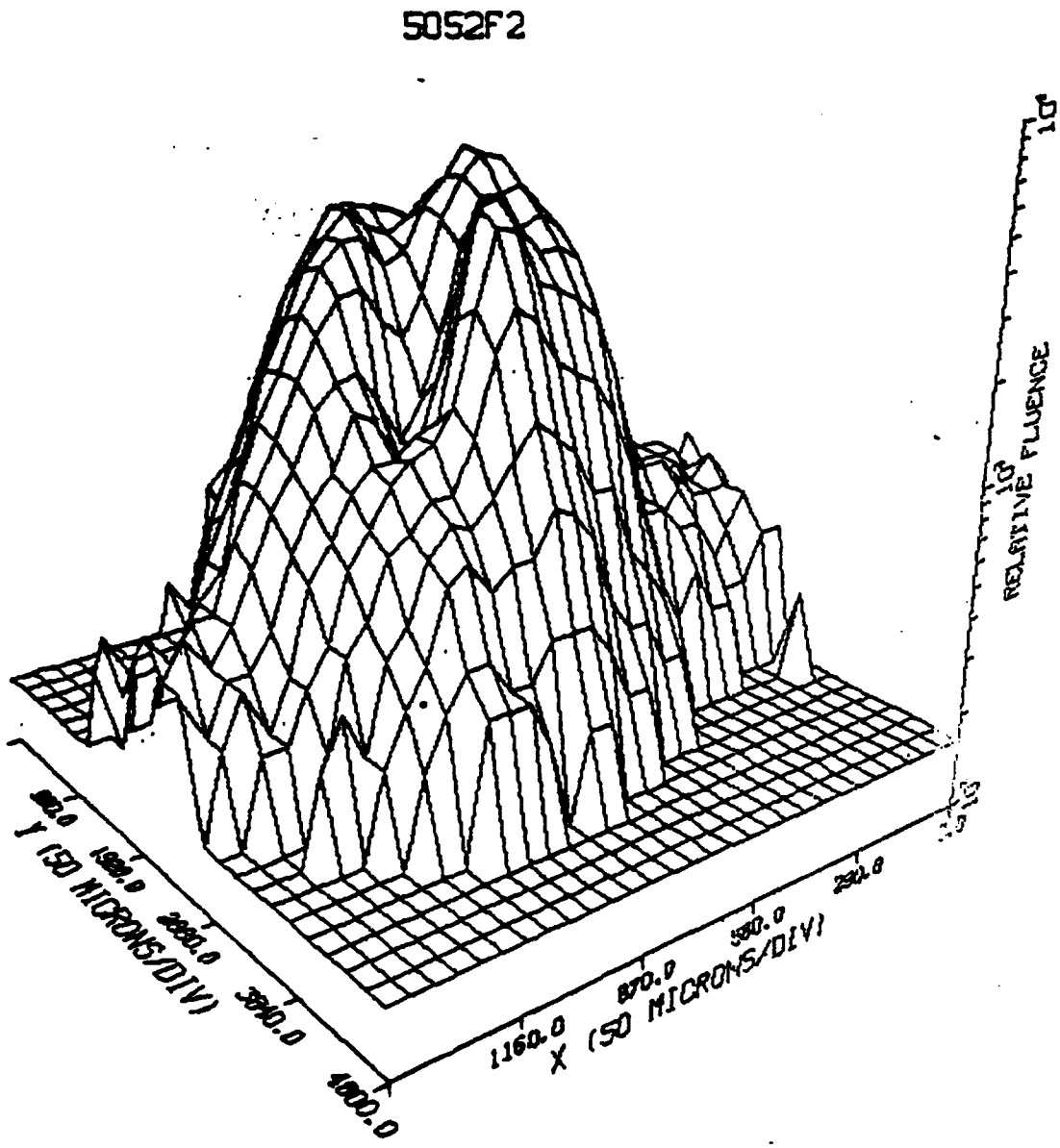

Figure IV.17. Shot 5052 hydrogen-like resonance line (1s - 2p).

5052F3

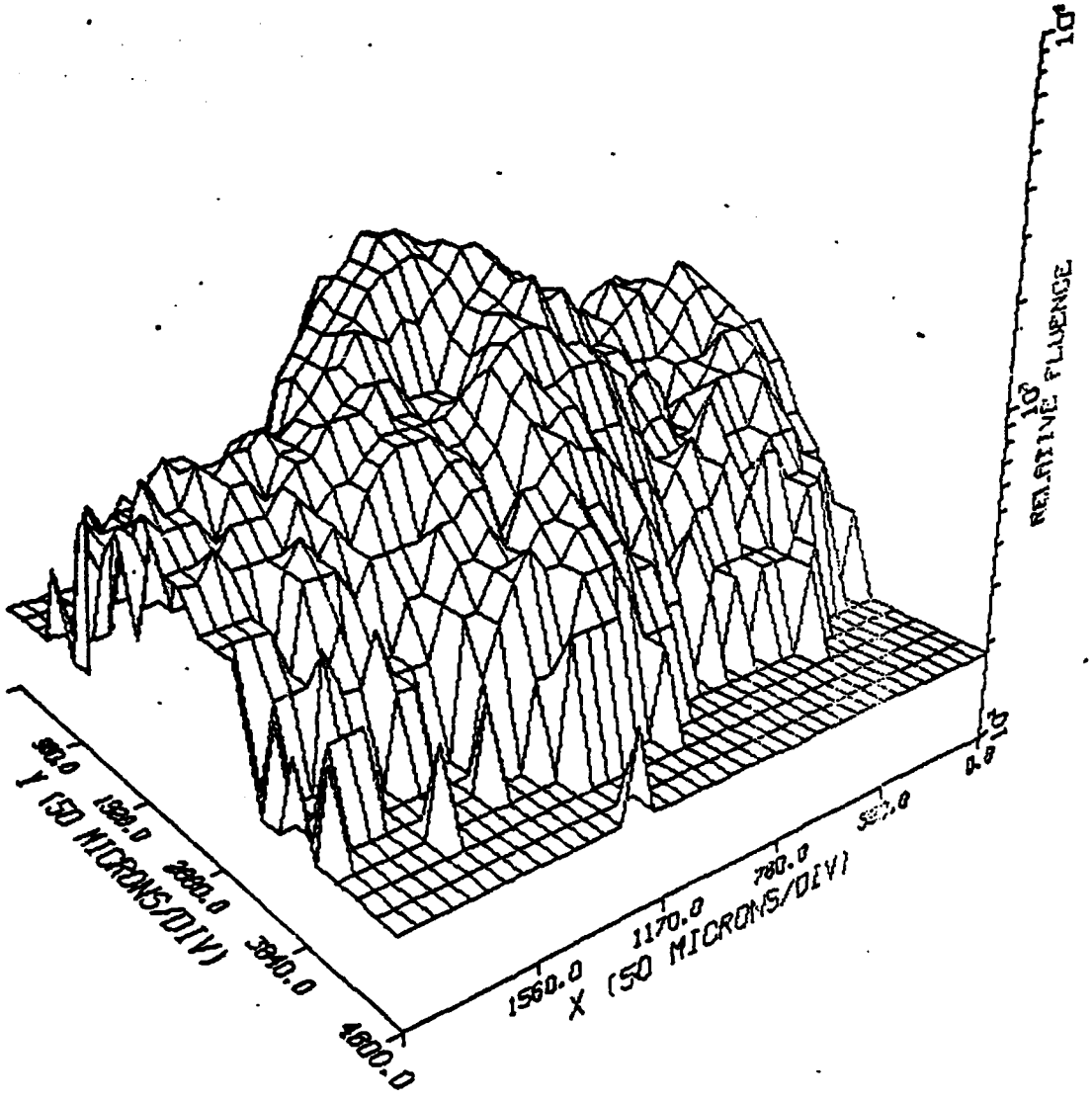

Figure IV.18. Shot 5052 $1s^2$ - 1s3p line.

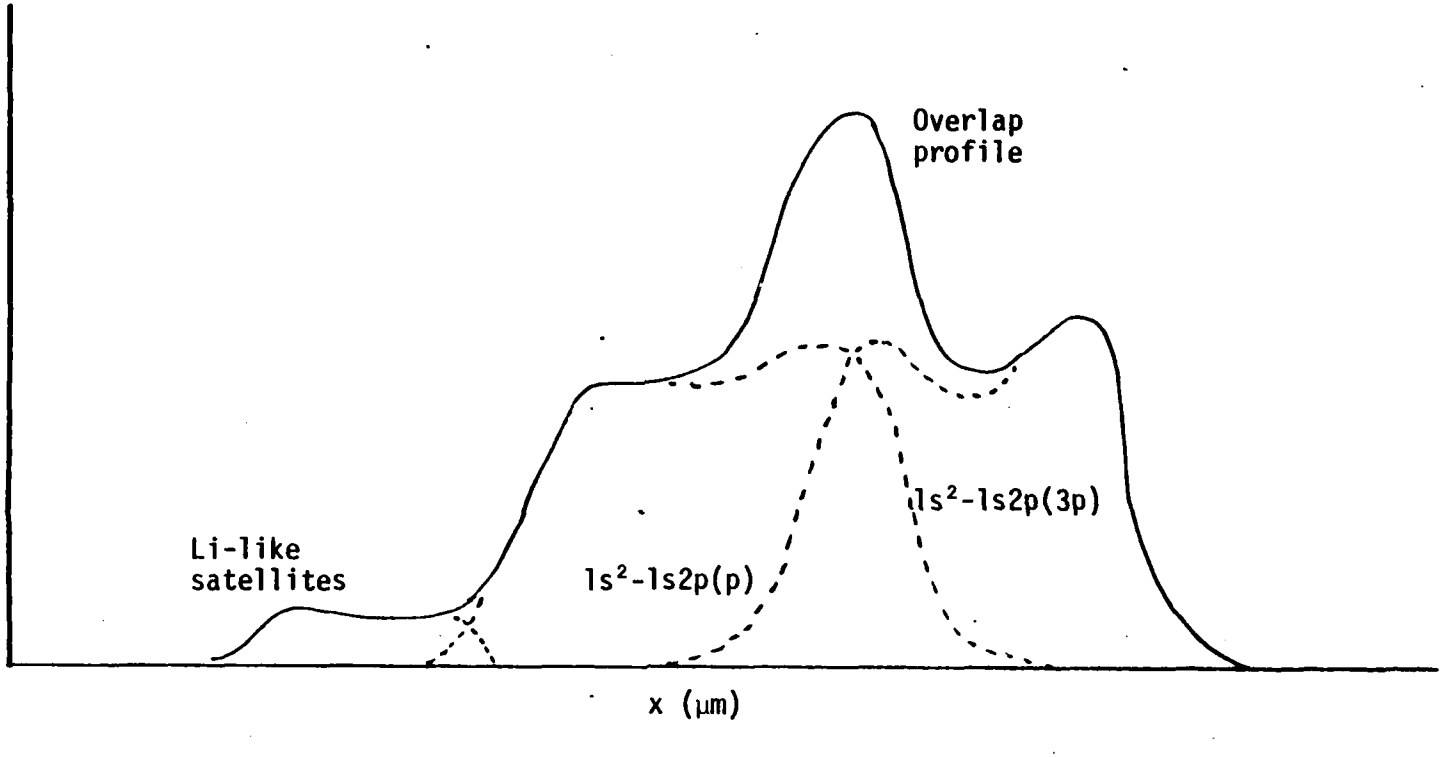

Figure IV.19. Resonance line, intercombination line reconstruction.

Table IV.2

Selected Helium-like and Hydrogen-like Aluminum Line Intensity Ratios from Optically Thin CRE Calculations

N_i (cm^{-3})	T_e (eV)	$\frac{1s^2 - 1s2p}{1s^2 - 1s^2p}$	$\frac{1s^2 - 1s2p}{1s^2 - 1s^3p}$	$\frac{1s^2 - 1s3p}{1s^2 - 1s2p}$	$\frac{1s^2 - 1s3p}{1s^2 - 1s2p}$
10^{1}	100	2.566×10^{-10}	1.676×10^{-8}	1.531×10^{-2}	6.006×10^{-3}
10^{18}	200	3.685×10^{-5}	5.818×10^{-4}	6.334×10^{-2}	3.082×10^{-2}
10^{18}	300	2.264×10^{-3}	2.420×10^{-2}	9.357×10^{-2}	5.613×10^{-2}
10^{18}	400	1.689×10^{-2}	1.473×10^{-1}	1.147×10^{-1}	7.389×10^{-2}
10^{18}	500	5.816×10^{-2}	4.444×10^{-1}	1.309×10^{-1}	8.745×10^{-2}
10^{19}	100	3.018×10^{-9}	1.365×10^{-7}	2.210×10^{-2}	6.035×10^{-3}
10^{19}	200	1.928×10^{-4}	2.256×10^{-3}	8.547×10^{-2}	3.060×10^{-2}
10^{19}	300	8.388×10^{-3}	6.964×10^{-2}	1.204×10^{-1}	5.539×10^{-2}
10^{19}	400	4.858×10^{-2}	3.479×10^{-1}	1.396×10^{-1}	7.259×10^{-2}
10^{19}	500	1.364×10^{-1}	8.999×10^{-1}	1.516×10^{-1}	8.559×10^{-2}
10^{20}	100	1.080×10^{-8}	2.424×10^{-7}	4.457×10^{-2}	6.645×10^{-2}
10^{20}	200	6.925×10^{-4}	5.080×10^{-3}	1.363×10^{-1}	3.016×10^{-2}
10^{20}	300	2.808×10^{-2}	1.757×10^{-1}	1.598×10^{-1}	5.081×10^{-2}
10^{20}	400	1.431×10^{-1}	9.243×10^{-1}	1.549×10^{-1}	6.383×10^{-2}
10^{20}	500	3.501×10^{-1}	2.396×10^{0}	1.462×10^{-1}	7.309×10^{-2}
10^{21}	100	6.378×10^{-9}	1.808×10^{-7}	3.527×10^{-2}	9.966×10^{-2}
10^{21}	200	5.927×10^{-4}	5.107×10^{-3}	1.161×10^{-1}	4.336×10^{-2}
10^{21}	300	3.163×10^{-2}	2.159×10^{-1}	1.465×10^{-1}	6.790×10^{-2}
10^{21}	400	1.933×10^{-1}	1.370×10^{0}	1.411×10^{-1}	8.114×10^{-2}

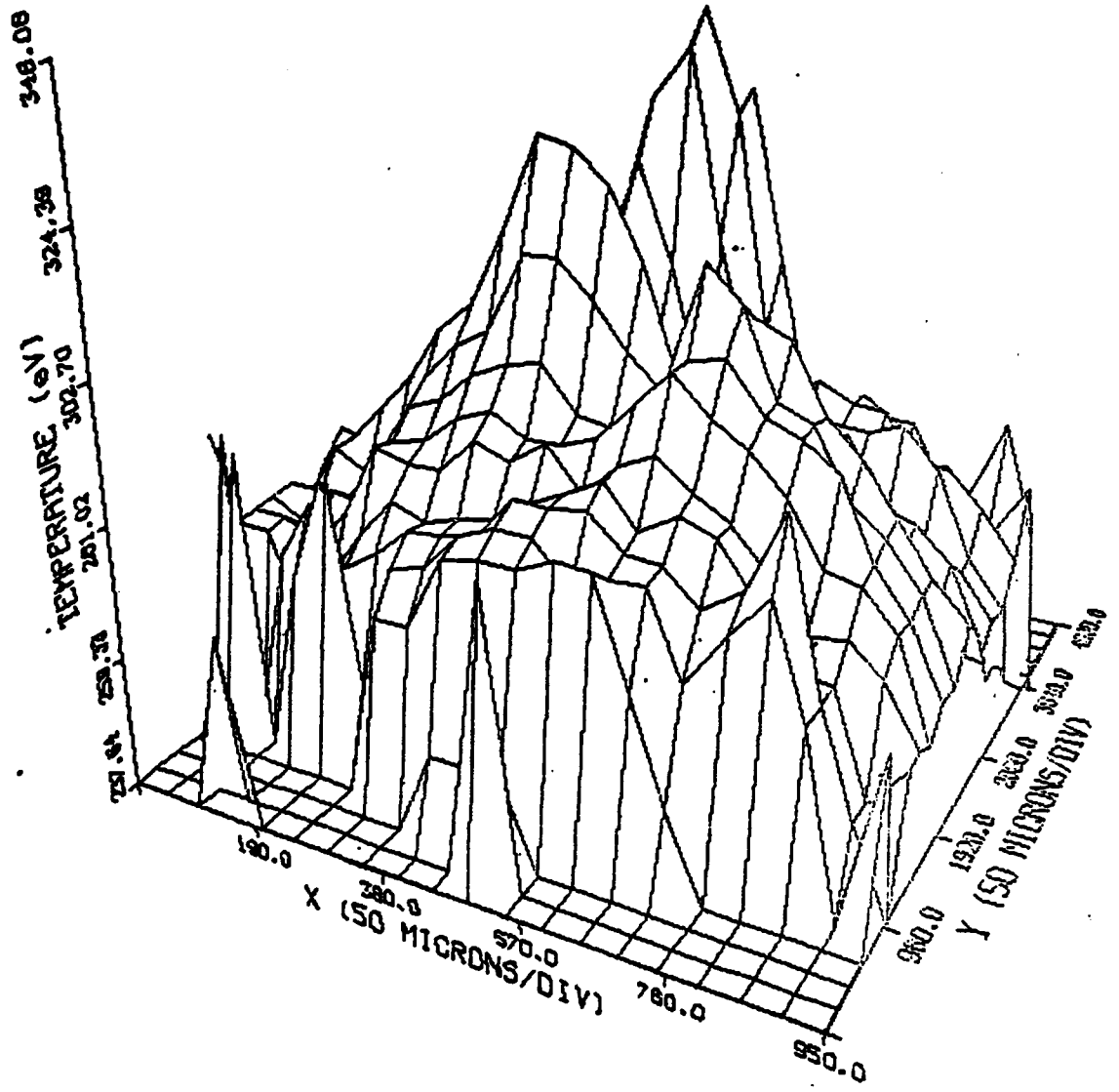

Figure IV.20. 2-D temperature map for Shot 5052, based on 1s - 2p/ $1s^2$ - $1s3p(^1P)$ line ratio assuming $n_i = 3 \times 10^{19}$ cm^{-3}, 500 μm radius.

$n_e \approx 10^{22}$ cm^{-3}) would yield a more pronounced dip in temperature on axis. The same procedure was used with the data from Shot 4040, resulting in the 2-D temperature plot shown in Figure IV.21.

For both shots (4040 and 5052), the inferred temperature range is about 300 to 450 eV. For Shot 4040, the recombination continuum film exposure was sufficiently dense to allow calculation of a 1-D map of temperature obtained from the continuum slope, as shown in Figure IV.22. From this analysis, the temperature map exhibited a local minimum of about 260 eV on axis, and maximum of about 500 eV at a radius of approximately 4 mm. These temperatures were, in effect, "chord averages", since only one degree of spatial resolution was obtained from the continuum. A better estimate of the azimuthally averaged radial temperature profile could have been obtained by an Abel inversion technique, but was not done.

It should be noted that the calculated line ratios including opacity were done for *homogeneous, steady-state plasmas*, and, therefore, did not include effects due to temporal and spatial gradients. The latter problem has been addressed by Duston, et al., to a limited extent [17,19], but much more work needs to be done. In general, the integrated spectra emitted by plasmas with spatial and temporal temperature and density distributions are weighted, and estimates of temperature such as we have presented tend toward those for which the lines used are strongest. Thus, we expect that our estimates are closer to peak temperatures in time and axial position, since for these ranges, the Al^{11+} and Al^{12+} lines are increasing in strength with temperature. Clearly, simultaneous radial-azimuthal and radial-axial space- and time-resolved spectrograph data are needed to yield more detailed information about the internal structure of these plasmas. Nevertheless, the results we have obtained are

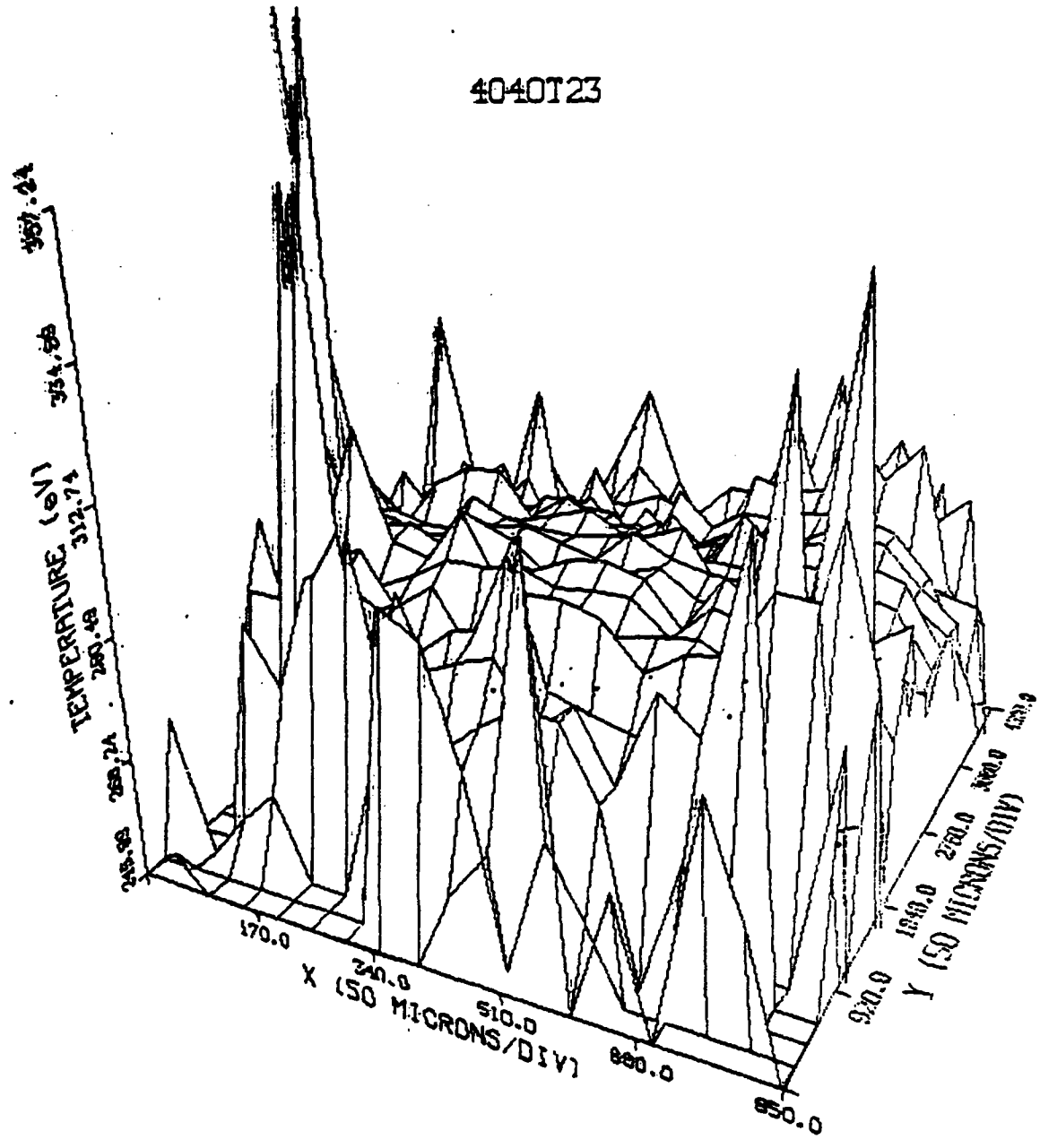

Figure IV.21. 2-D temperature map for Shot 4040, based on 1s - 2p/ $1s^2$ - $1s3p(^1P)$ line ratio assuming $n_i = 3 \times 10^{19}$ cm^{-3}, 500 μm radius.

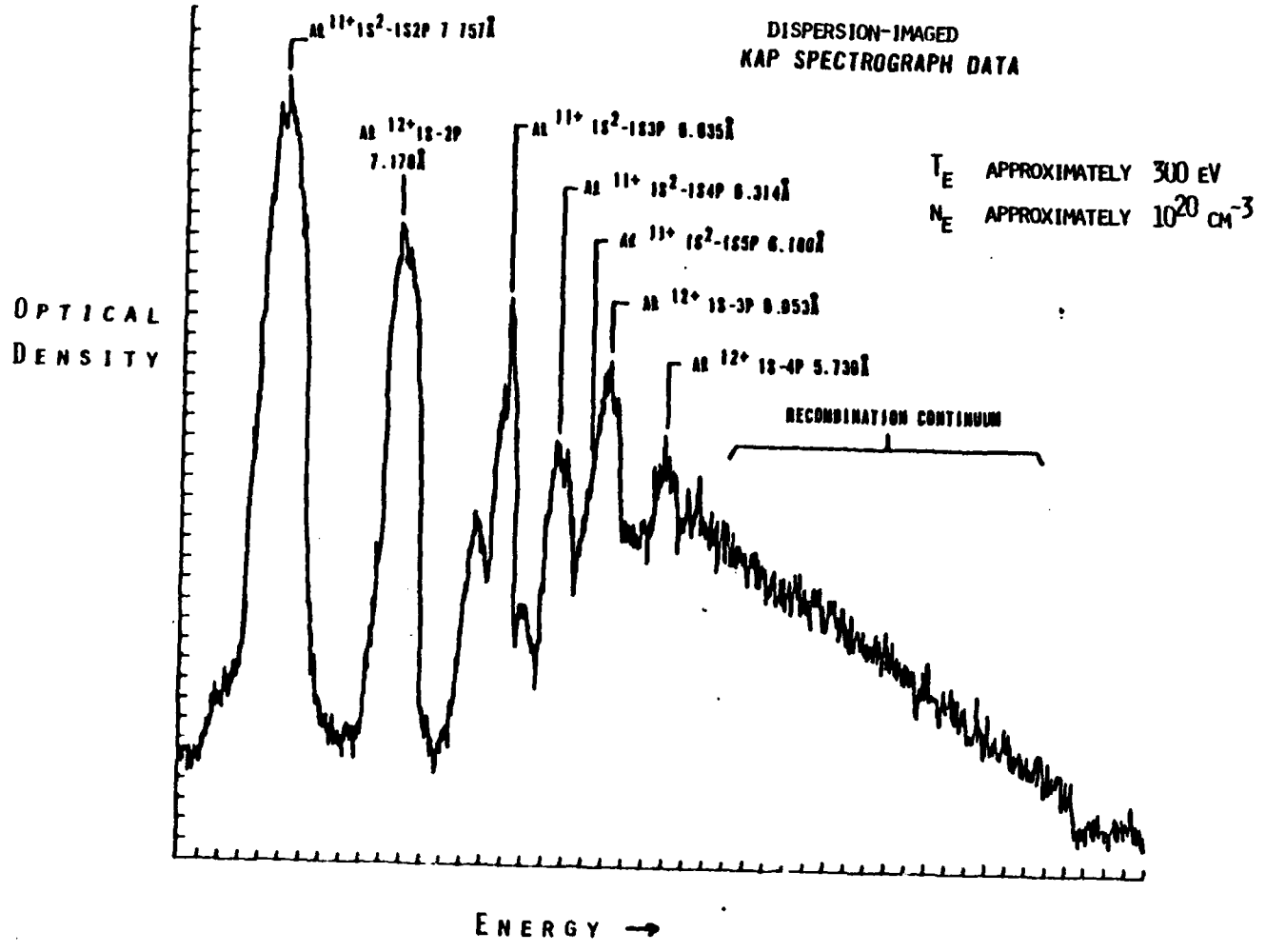

Figure IV.22. Optical density scan along a chord of the plasma, indicating recombination continuum and temperature.

spatially more detailed than any other studies of this kind of which we are aware, and the trends indicated are in agreement with 2-D MHD code simulations, such as shown in Figure IV.23.

D. Time-Resolved Spectroscopy

An attempt has been made to develop the capability to time-resolve the space-resolved aluminum K-shell spectra shown in this report. The basic idea is to replace the photographic film recording medium with an optical convertor. One can then use any one of a number of high-speed photographic techniques to record the spectral images with time resolution. We have chosen plastic scintillators (e.g., NE102, NE111) for the optical converter, since they exhibit fast (< few nanosecond) relaxation times, and their response to soft x-rays is well-documented. The preliminary design called for an array of photodiodes to monitor the temporal behavior of each of the major lines in the Al 1s - np series and recombination continuum, disregarding spatial resolution. A modified spectrograph to accomplish these measurements is shown in Figure IV.24. Unfortunately, the SHIVA facility was being upgraded from the time the instrument was assembled until the expiration of this contract, and no data could be taken. Subsequent plans included recording spectra with simultaneous 1-D spatial and temporal resolution using a high-speed streak camera, and, ultimately, full 2-D time-resolved spectroscopy with a fast framing camera.

E. Summary

We have used dispersion imaging in conjunction with conventional slit (one-dimensional pinhole) imaging with a convex curved KAP crystal spectrograph to record time-integrated, two-dimensional space-resolved K-shell spectra from highly ionized

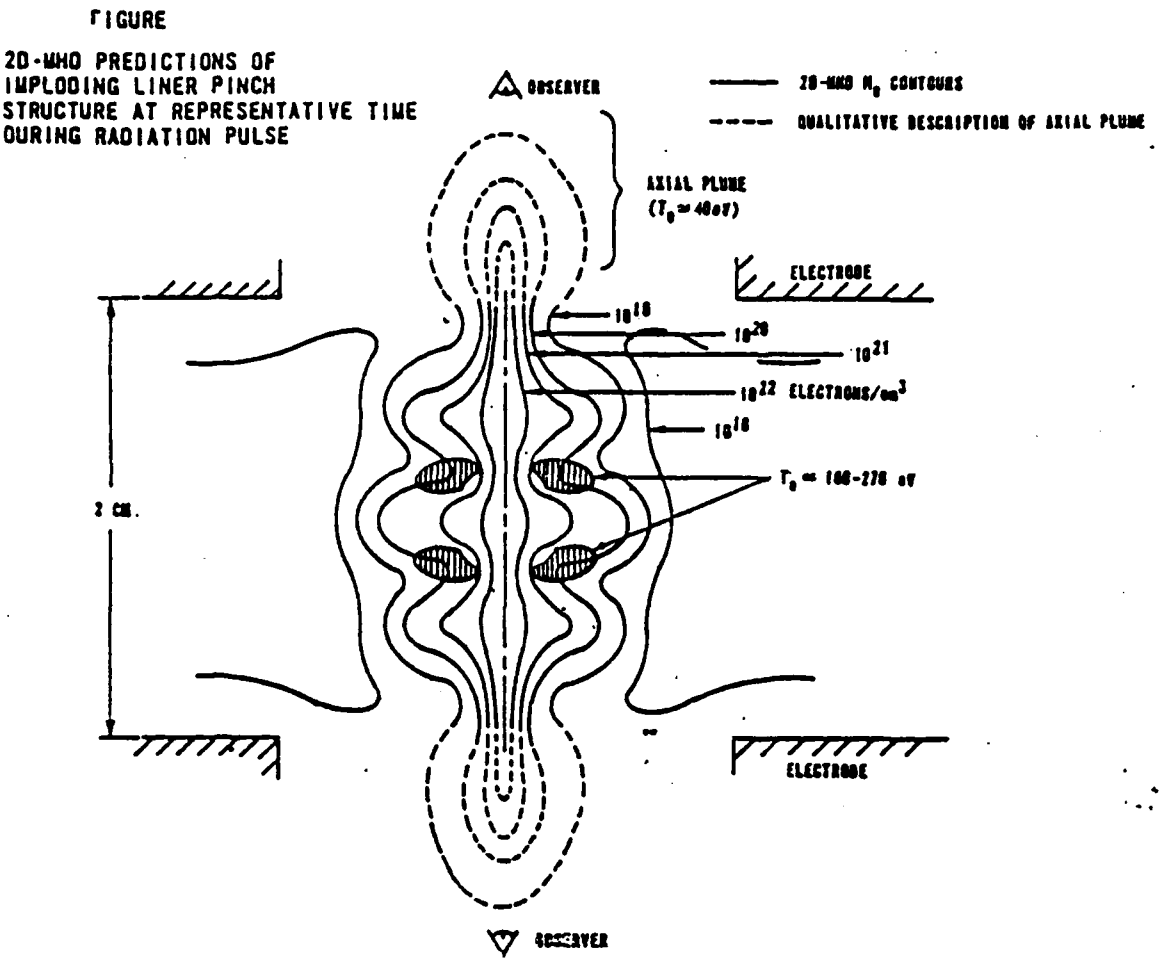

Figure IV.23. 2-D (r - 3) MHD code code prediction of isothermal and isodensity contours at time of SHIVA pinch.

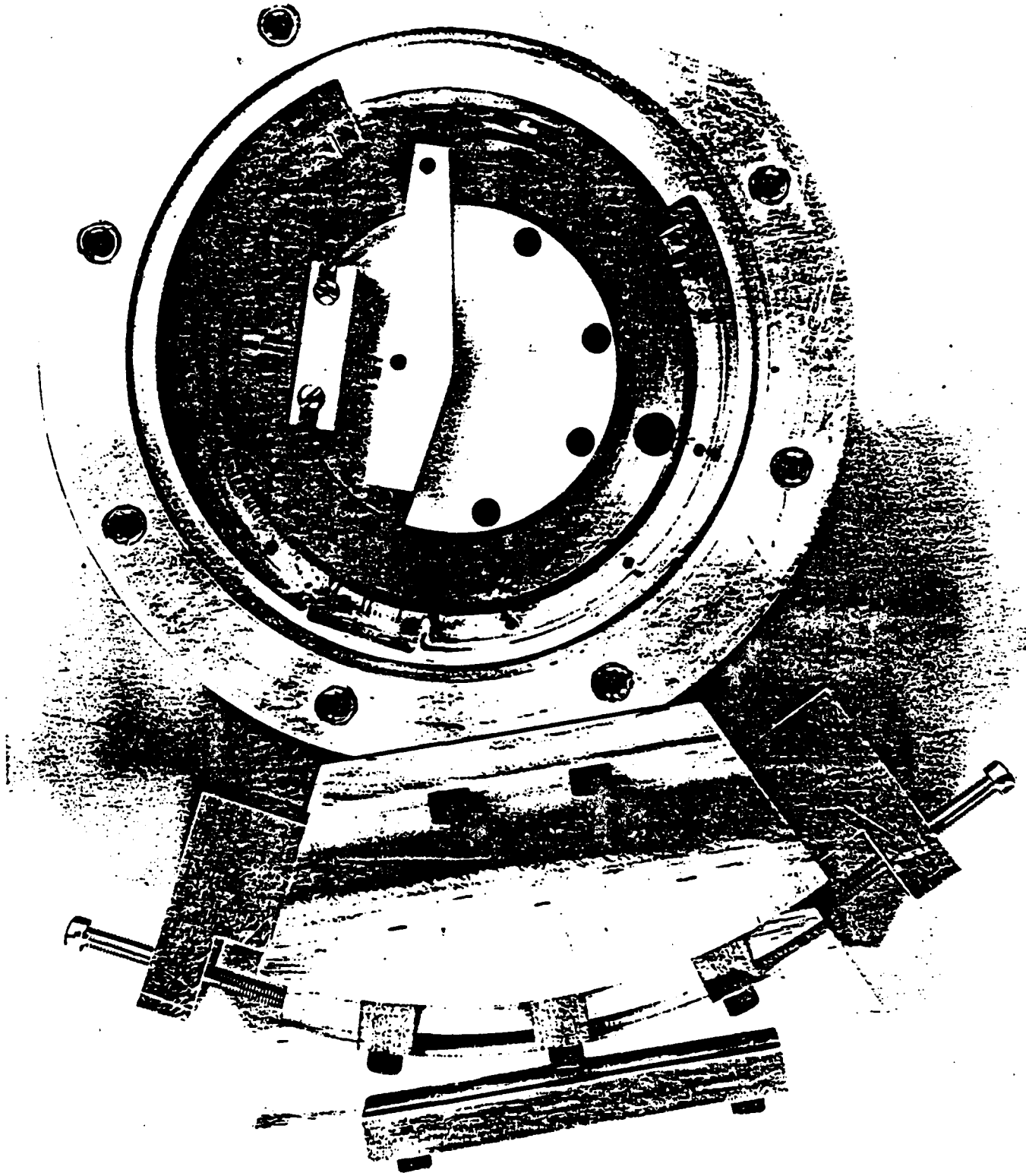

Figure IV.24. Time-resolved KAP crystal spectograph.

aluminum plasmas. Ray-tracing techniques have shown that for spectrally isolated lines in the 1s - np hydrogen-like and helium-like series, dispersion mapping is linear over typical parameter ranges for SHIVA extended plasma sources. We have taken the most current line ratio analysis calculations, including opacity effects, and made semiquantitative estimates of two-dimensional temperature and density distributions of SHIVA plasmas. These estimates, 10^{9} to 10^{20} cm^{-3} ion density (10^{20} to 10^{21} cm^{-3} electron density) and 200 to 500 eV temperature, and their distribuions, are in agreement with two-dimensional MHD computer simulations. Further details of the work in this section are presented in reference [68].

SECTION IV REFERENCES

IV. 1. Landshoff, R. K. and J. D. Perez, Phys. Rev. A 13, 1619 (1976).

IV. 2. Hoffmann, A. L. and E. A. Crawford, J. Appl. Phys. 49, 3219 (1978).

IV. 3. Duston, D. and J. J. Duderstadt, J. Appl. Phys. 49, 4388 (1978).

IV. 4. Duston, D. and J. J. Duderstadt, Phys. Rev. A 18, 1707 (1978).

IV. 5. Davis, J. and K. G. Whitney, J. Appl. Phys. 45, 5294 (1974).

IV. 6. Salzmann, D. and A. Krumbein, J. Appl. Phys. 49, 3229 (1978).

IV. 7. Perez, J. D. and G. L. Payne, Phys. Rev. A 21, 968 (1980).

IV. 8. Kilkenny, J. D., R. W. Lee, M. H. Key, and J. G. Lunney, Phys. Rev. A 22, 2746 (1980).

IV. 9. Colombant, D. G., K. G. Whitney, D. A. Tidman, N. K. Windsor, and J. Davis, Phys. Fluids 18, 1687 (1975).

IV. 10. Duston, D. and J. Davis, NRL Memorandum Report No. 3846 (1978) (unpublished).

IV. 11. Duston, D. and J. Davis, Phys. Rev. A 21, 1664 (1980).

IV. 12. Whitney, K. G., J. Davis, and J. P. Apruzese, Phys. Rev. A 22, 2196 (1980).

IV. 13. Duston, D. and J. Davis, Phys. Rev. A 21, 932 (1980).

IV. 14. Apruzese, J. P., J. Davis, D. Duston, and K. G. Whitney, J. Quant. Spectrosc. Radiat. Transfer 23, 479 (1980).

IV. 15. Apruzese, J. P., J. Quant. Spectrosc. Radiat. Transfer 25, 419 (1981).

IV. 16. Duston, D. and J. Davis, Phys. Rev. A 23, 2602 (1981).

IV. 17. Duston, D., J. Davis, and P. C. Kepple, Phys. Rev. A 24, 1505 (1981).

IV. 18. Duston, D. and J. Davis, J. Quant. Spectrosc. Radiat. Transfer 27, 267 (1982).

IV. 19. Duston, D. and J. Davis, NRL Memorandum Report No. 5038 (1983) (unpublished).

IV. 20. Burns, E.J.T., J. H. Degnan, R. E. Reinovsky, W. L. Baker, M. C. Clark, and C. R. McClenahan, Appl. Phys. Lett. 31, 477 (1977).

IV. 21. Burkhalter, P. and J. Davis, NRL Memorandum Report 3934, 1979 (unpublished).

IV. 22. Burkhalter, P. G., R. Schneider, C. M. Dozier, and R. D. Cowan, Phys. Rev. A 18, 718 (1978).

IV. 23. Gordon, H., M. G. Hobby, and N. J. Peacock, J. Phys. B 13, 1985 (1980).

IV. 24. Glibert, K. M., J. P. Anthes, M. A. Gusinow, M. A. Palmer, R. R. Whitlock, and D. J. Nagel, J. Appl. Phys. 51, 3 (1980).

IV. 25. Boiko, V. A., S. A. Pikuz, A. S. Safranova, A. Ya Faenov, P. O. Bogdanovich, G. V. Merkelis, Z. B. Rudzikas, and S.D. Sadziuviene, J. Phys. B 12, 1927 (1980).

IV. 26. Van Rohman, H., Z. Phys. 15, 510 (1914).

IV. 27. de Broglie, M. and F. A. Lindemann, C. R. Acad. Sci. Paris 158, 944 (1914).

IV. 28. Birks, L. S., Rev. Sci. Inst. 8, 1129 (1970).

IV. 29. Henke, B. L. and M. A. Tester in Advances in X-Ray Analysis, Vol. 18, edited by W. L. Pickles, C. S. Barrett, J. B. Newkirk, and C. O. Rudd (Plenum, New York, 1975), 76.

IV. 30. Burns, E.J.T. in Advances in X-Ray Analysis, Vol. 18, edited by W. L. Pickles, C. S. Barrett, J. B. Newkirk, and C. O. Rudd (Plenum, New York, 1975), 117.

IV. 31. Kastner, S. O., Appl. Opt. 18, 374 (1979).

IV. 32. Kiuttu, G. F., Air Force Weapons Laboratory Report AFWL-DYP-TN-79-117 (1979) (unpublished).

IV. 33. Gersten, M. and J. E. Rauch, J. Appl. Phys. 53, 1297 1982.

IV. 34. Liefield, R. J., J. Hanzely, T. B. Kirby, and D. M. Mott, in Advances in X-Ray Analysis, Vol. 13, edited by B. L. Henke, J. B. Newkirk, and G. R. Mallett (Plenum, New York, 1970), 373.

IV. 35. Brown, D. B. and M. Fatami, J. Appl. Phys. 45, 1544 (1974).

IV. 36. Chase, L. F., R. K. Bardin, T. R. Fisher, H. A. Grench, W. C. Jordan, D. A. Kohler, R. K. Landshoff, T. D. Miller, and J. G. Pronko, DNA Report 3404F (1974) (unpublished).

IV. 37. Birks, L. S., Electron Probe Microanalysis, 2nd ed. (Wiley-Interscience, New York, 1971), 43.

IV. 38. Dozier, D. M., D. B. Brown, and L. S. Birks, J. Appl. Phys. 47, 3732 (1976).

IV. 39. Benjamin, R. F., P. B. Lyons, and R. H. Day, Appl. Opt. 16, 393 (1977).

IV. 40. Dietz, E. R., T. S. Durland, B. L. Henke, and M. A. Tester in Low Energy X-Ray Diagnostics - 1981 (AIP Conf. Proc. No. 75), edited by D. T. Attwood and B. L. Henke (AIP, New York, 1981), 275.

IV. 41. Rauch, J. E., M. Gersten, C. E. Trivelpiece, L. N. Koppel, and J. L. Gaines, Bull. Am. Phys. Soc. 26, 967 (1981).

IV. 42. Turchi, P. J. and W. L. Baker, J. Appl. Phys. 44, 4936 (1973).

IV. 43. Baker, W. L., M. C. Clark, J. H. Degnan, G. F. Kiuttu, C. R. McClenahan, and R. E. Reinovsky, J. Appl. Phys. 49, 4694 (1978).

IV. 44. Reinovsky, R. E., J. H. Degnan, G. F. Kiuttu, R. A. Nuttelman, and W. L. Baker in Megagauss Physics and Technology, edited by P. J. Turchi (Plenum, New York, 1980), 313.

IV. 45. Yaakobi, B., T. C. Bristow, and A. Hanes, Opt. Comm. 14, 336 (1975).

IV. 46. Dozier, C. M., D. J. Nagel, and L. S. Birks, J. of Phys. E 10, 1183 (1977).

IV. 47. Kiuttu, G. F., J. H. Degnan, and D. M. Woodall, Bull. Am. Phys. Soc. 23 (1978).

IV. 48. H. R. Griem, Spectral Line Broadening by Plasmas (Academic, New York, 1974).

IV. 49. Pannecock, A., Mon. Not. 98, 694 (1938).

IV. 50. Inglis, D. and E. Teller, Astrophys. J. 90, 439 (1939).

IV. 51. Davis, J., NRL Memorandum Report 2655 (1973) (unpublished).

IV. 52. Burkhalter, P. G., C. M. Dozier, and D. J. Nagel, Phys. Rev. A 15, 700 (1977).

IV. 53. Burkhalter, P., J. Davis, J. Rauch, W. Clark, G. Dahlbacka, and R. Schneider, J. Appl. Phys. 50, 705 (1979).

IV. 54. Burkhalter, P. G., J. Shiloh, A. Fisher, and R. D. Cowan, J. Appl. Phys. 50, 4532 (1979).

IV. 55. Kepple, P. C. and H. R. Griem, NRL Memorandum Report 3634 (1978) (unpublished).

IV. 56. Griem, H. R., Plasma Spectroscopy (McGraw-Hill, New York, 1964), pp. 95-98.

IV. 57. ibid, pp. 175-176.

IV. 58. Johnson, D. J., Air Force Weapons Laboratory Report AFWL-TR-74-43 (1974).

IV. 59. Kiuttu, G. F., J. H. Degnan, R. A. Nuttelman, R. E. Reinovsky, D. M. Woodall, and W. L. Baker, Air Force Weapons Laboratory Report AFWL-DYP-TN-79-119 (1979) (unpublished); Bull. Am. Phys. Soc. 24, 1057 (1979).

IV. 60. Degnan, J.H., Rev. Sci. Inst. 50, 1223 (1979).

IV. 61. Woodall, D. M., J. H. Degnan, G. F. Kiuttu, R. J. Sand, R. E. Reinovsky and W. L. Baker, Bull. Am. Phys. Soc. 25, 872 (1980).

IV. 62. Degnan, J. H., R. J. Sand, G. F. Kiuttu, and D. M. Woodall in Low Energy X-Ray Diagnostics-1981 (AIP Conf. Proc. No. 75) edited by D. T. Attwood and B. L. Henke (American Inst. of Phys., New York, 1981), pp. 264-269.

IV. 63. Kiuttu, G. F., J. H. Degnan, R. J. Sand, and D. M. Woodall, Bull. Am. Phys. Soc. 26, 892 (1981).

IV. 64. Chase, L. F., W. C. Jordan, J. D. Perez, and R. R. Johnston, Phys. Rev. A 13, 1497 (1976).

IV. 65. Vinogradov, A. V., I. Yu. Skobelev, and E. A. Yukov, Kvant. Electron. (Moscow) 2, 1165 (1975) [Sov. J. Quant. Elec. 5, 630 (1975)].

IV. 66. Burkhalter, P. G., D. B. Brown, and M. Gersten, J. Appl. Phys. 52, 4379 (1981).

IV. 67. Duston, D., private communication.

IV. 68. Kiuttu, G. F., "Spectroscopy of High Density Plasmas," Ph.D dissertation, University of New Mexico, 1984.

LIST OF FIGURES

LIST OF FIGURES (continued)

LIST OF TABLES

V. APPENDIX, PUBLICATIONS, AND PRESENTATIONS

A. Presentations and Abstracts

The following pages include the abstracts submitted to technical conferences to report work supported in part or entirely by this grant.

4S19 Injection of a Marshall Gun Plasma along a Magnetic Field.* G. James, L. Sanchez, and D. Woodall, Univ. of New Mexico. We have produced a dense, fully-ionized plasma for planned relativistic electron beam heating experiments. A Marshall gun[1] operated in both Prefill and Gas PUFF (Deflagration[2]) modes has been used to inject plasma of $10^{21}/m^3$ density, into a 1-5 Tesla solenoidal magnetic field. Plasma density, temperature, and impurity content measurements have been made. The array of diagnostics on the experiment includes B loops, Faraday collectors, calorimeters, open shutter visible light photographs, a visible light 0.5 m spectrograph, and a pulsed-ruby laser interferometer. Experimental results will be presented, along with plans for further work.

[1]J. Marshall, Phys. Fluids 3, 134 (1960)

[2]D. Y. Cheng, Nucl. Fusion 10, 305 (1970)

*Work supported by AFOSR under Grant 79-0060

2V 2 2-D Temperature and Density Distributions from Spectroscopic Measurements of Imploding Liner Plasmas.* G.F. KUITTU[a], J.H. DEGNAN, R.J. SAND, and D.M. WOODALL[a], Air Force Weapons Laboratory, Kirtland AFB, New Mexico.—Using a convex curved KAP crystal orthogon imaging slit, we have recorded spatially resolved K shell spectra from hot (T_e = 40 - 400 eV) dense ($n_e = 10^{19} - 10^{21}$ cm^{-3}) aluminum plasmas. (The plasmas were formed in terawatt level electromagnetic implosions of aluminum-plastic foils at the Air Force Weapons Laboratory' SHIVA facility.) The approximately 1 cm diameter 2 cm long cylindrical sources were viewed end on, yielding axial line-of-sight and time integrated spectral intensities. The relative intensities of the lines and recombination continua were used to estimate local temperatures and densities. In this paper we present the measurement technique and analysis results for representative spatially resolved spectra.

*Work supported by AFOSR under Contract Nr 79-0060.

[a]Dept of Chemical and Nuclear Engineering, University of New Mexico.

1. G.F. Kiuttu, Air Force Weapons Laboratory Report, AFWL-DYP-TN-79-117 (unpublished).

7P3 Grazing Incidence X-Ray Spectroscopy for Analysis of SHIVA Spectral Output. D. WOODALL,* G. KIUTTU, R. NUTTELMAN, R. REINOVSKY, and W.L. BAKER, Air Force Weapons Laboratory, Kirtland AFB, NM.--The 1.9MJ SHIVA[1] bank provides an intense burst of soft x-radiation from an imploded metallic shell. To obtain absolute yields and improved energy resolution, we have prepared a grazing incidence spectrograph for use as a diagnostic. The GML5M[2] uses a 316/mm X-ray phase lamellar grating and the energy range covered in first order in our geometry is 70-620ev. We have calibrated the spectrometer (Ilford Q2 plates) in multiple orders at 109ev, 277ev, 523ev and 705ev, using the AFWL Henke tube X-ray facility. The expanding plasma and debris produced by the SHIVA bank requires interruption to protect the instrument from damage. We are using a serial pair of fast (theta-pinched conducting cylinder) and slow (pneumatically driven knife blade) shutters to isolate the GML5M from debris after the shot. Calibration results and experimental data will be presented and discussed.

*Also, University of New Mexico, Albuquerque, NM 87131
[1]W.L. Baker, J. Appl. Phys. 49, 4694 (1978)
[2]Grazing Measurement Limited, London, England

7P4 Dispersive Spectral Measurements of Imploding Liner Radiation Pulse.* J.H. DEGNAN, G.F. KIUTTU, R.A. NUTTELMAN, R.E. REINOVSKY, D.M. WOODALL,** and W.L. BAKER, Air Force Weapons Laboratory, Kirtland AFB, NM.--Convex curved crystal spectrographs (Lead Stearate, Lead Myristate, KAP, and RAP) and a 5 meter grazing, incidence spectrograph are used to obtain dispersive measurements of the ultrasoft and soft X-ray emission (70eV-3KeV) produced by an imploding plasma liner. The liner implosions, obtained by discharging the 1.3MJ, 1.4μsec SHIVA capacitor bank through 7cm radius, 2cm tall aluminized plastic cylinders, produce radiation pulses $\sim 10^{12}$ Watts[1]. Spectrograph data will be presented and discussed. It will be compared with unfolded spectra obtained from arrays of X-ray photodiodes and with theoretical predictions.

* Work supported by USAF
**Also with University of New Mexico, Department of Chemical and Nuclear Engineering
[1] W.L. Baker et al, JAP 49, 4694 (1978)

7P5 Soft X-Ray Imaging of Imploded Liner Plasmas.* G.F. KIUTTU, J.H. DEGNAN, R.A. NUTTELMAN, R.E. REINOVSKY, D.M. WOODALL,** and W.L. BAKER, Air Force Weapons Laboratory, Kirtland AFB, NM.--To investigate the spatial distribution of hot dense plasmas formed in the AFWL SHIVA imploding liner experiment[1], we have implemented several X-ray imaging diagnostics. They include simple pinhole cameras with X-ray transmission filters, space resolved convex curved spectrographs, and two time resolved X-ray pinhole cameras. One camera achieves time resolution with a transmission photodiode and scintillator viewed with a fast camera, the other with a gated microchannel plate, phosphor and film. Diagnostic design and calibration will be presented along with representative data.

* Work supported by USAF
**Also, with University of New Mexico, Department of Chemical and Nuclear Engineering
[1] W.L. Baker et al, J. Appl. Phys. 49, 4694 (1978).

2V 9 Spectral Features in the 80eV-2Kev Energy Range from an Imploded SHIVA Foil. D.M. WOODALL*, J.H. DEGNAN, G.F. KIUTTU*, R.J. SAND, R.E. REINOVSKY, and W.L. BAKER, Air Force Weapons Laboratory, Kirtland AFB NM--A 5 meter grazing incidence spectrograph was used to obtain detailed dispersive measurements of the ultra-soft X-ray emission from an imploding liner experiment. A 7cm radius, 2cm tall, 160ug/cm^2 aluminized plastic foil cylinder was driven by the AFWL SHIVA capacitor bank (1.3MJ, 100kV, 12MA, 1.2μs), producing a pinch radiation burst of ∿ 100kJ in ∿ 100nsec. The spectrograph covered the range 85ev-525ev in first order. Data indicated a strong continuum below the 284ev carbon edge with weak absorption lines (Al^{4+}, Al^{5+}) below 230ev, and Al^{11+} (3rd order), Al^{10+}, O^{7+} (2nd order), and C^{5+} emission lines at higher energies. These features are indicative of a cool (∿ 40ev) envelope surrounding a hotter (∿ 200ev) plasma core. We present detailed line shape analysis and spatial characteristics of the radiation source.

*Also University of New Mexico, Albuquerque NM 87131.

8T 2
PRODUCTION OF A HIGH DENSITY PLASMA TARGET FOR REB HEATING EXPERIMENTS.* L.K. LEN, D.M. WOODALL, C.A. EKDAHL,** UNIVERSITY OF NEW MEXICO, ALBUQUERQUE, NM 87131. We have studied the production of high density (Ne up to 2x10^{20}/m^3), uniform, field-embedded plasma for intense relativistic electron beam heating experiments.[1] A coaxial Marshall gun was discharged with a hydrogen gas prefill of 0.2-8.0 torr and in the deflagration, gas puff mode of Cheng.[2] A plasma column of 0.1 m diameter and 1.0 m length resulted from the combination of plasma streaming and shock ionization of the background gas. Plasma was embedded in a magnetic field up to 3.0 T for the heating experiments. Diagnostics include B-probes, Faraday cups, calorimeters, and visible spectroscopy using a 0.5 m Czerny-Turner instrument. Time-integrated density measurements using stark-broadened Hg show remarkable consistency with predictions, even using a low dynamic range film (Polaroid type 410) and Vidicon data analysis system.

*Work supported by Air Force Office of Scientific Research under Grant 79-0060.
**Also, Los Alamos Scientific Laboratory.
1. L.E. Thode, et al., Abstracts, IEEE Int. Conf. on Plasma Sci., Madison, WI, p. 23 (1980).
2. D. Y. Cheng, Nucl. Fusion, 10, 305 (1970).

The following list includes those conferences attended with partial or full support by this grant.

1. IEEE International Conference on Plasma Sciences, Montreal, Quebec, June 1979.

2. APS-Plasma Physics Division Annual Meeting, Boston, Massachusetts, November 1979.

3. NBS-3rd Workshop on the Uses of XUV and X-Ray Photometry, Bethesda, Maryland, November 1979.

4. IEEE International Conference on Plasma Sciences, Madison, Wisconsin, May 1980.

5. Workshop on particle Beam Research, Air Force Academy, Colorado Springs, Colorado, January 1980.

6. High Energy X-Ray Source Technology Conference, Air Force Weapons Laboratory, Kirtland Air Force Base, New Mexico, July 1980.

7. APS Plasma Physics Division Annual Meeting, San Diego, California, November 1980.

8. Energetic Electron Beam Meeting, Lawrence Livermore Laboratory, Livermore, California, November 1980.

9. IEEE International Conference on Plasma Sciences, Santa Fe, New Mexico, May 1981.

10. IEEE Third International Conference on Pulsed Power, Albuquerque, New Mexico, June 1981.

11. APS Conference on Low Energy X-ray Diagnostics, Livermore, California, July 1981.

12. APS Plasma Physics Division Annual Meeting, New York, New York, October 1981.

13. "The Snowplow and Deflagration Modes of Operation in Coaxial Plasma Guns," L. K. Len, Ph.D dissertation, University of New Mexico (1984).

14. "Spectroscopy of High Density Plasmas," G. F. Kiuttu, Ph.D dissertation, University of New Mexico (1984).

B. Publications

A number of the results obtained under the support of this grant are of sufficient interest to the technical community to deserve publication. Some of those results are being prepared for submittal. Attached is one report of research which has already been published in a conference proceedings, AIP Conference Proceedings No. 75, Low Energy X-Ray Diagnostics, 1981 (Monterey), E. B. Atwood and Henke (1981).

SOFT AND ULTRASOFT X-RAY MEASUREMENTS OF AIR FORCE WEAPONS LABORATORY SHIVA IMPLODING PLASMA LINER

J. H. DEGNAN and R. J. SAND, Air Force Weapons Laboratory

G. F. KIUTTU and D. M. WOODALL, University of New Mexico

Albuquerque, New Mexico

Measurements of the radiation from high energy density plasmas formed by electromagnetic implosion of aluminized plastic cylindrical foil liners is discussed. The implosions were driven by the SHIVA capacitor bank - originally a 1.1 MJ, 1.2 microsecond, 100 KV device, later upgraded to 1.9 MJ, 1.4 microseconds, 120 KV. Discharge currents were 7 to 12 MA and implosion times 1.2 to 1.5 microseconds.

Photon pulses were observed using arrays of x-ray photodiodes, calorimeters and bolometers, x-ray pinhole cameras, convex curved crystal and grazing incidence grating spectrographs. Photon pulse energies from 100 KJ to 240 KJ were observed (assuming isotropic emission) with FWHM from 80 to 200 nanoseconds. The best combined photon yield and FWHM was 240 KJ, 130 nanoseconds. Bolometer, calorimeter, x-ray photodiode comparisons, and time-resolved spectra deconvoluted from x-ray photodiode array data are discussed.

Detailed spectrograph data indicate a continuum-dominated spectrum with Al^{4+}, Al^{5+}, O^{4+}, and O^{5+} absorption lines for photon energies below 200 eV. Al^{10+}, Al^{11+}, Al^{12+}, O^{7+}, and C^{5+} emission line and recombination radiation were observed at higher photon energies. The data indicate a 10^{19} - 10^{21} cm^{-3} electron density, 200 - 400 eV inner core shining through a 40 eV absorbing region in the pinch.

Space-resolved spectrograph and x-ray pinhole camera data often show a cold spot in the center, suggestive of an absorbing axial plume. Gross radiation power, as well as spectral detail and pinch structure are in approximate agreement with pinch conditions predicted by 2-D MHD calculations.

Implosion experiments with aluminized deuterated plastic cylindrical foil liners (3% deuterium by weight) yielded up to 4×10^8 neutrons, observed with silver activation and scintillator-photomultiplier detectors. This is approximately consistent with the spatial-temporal temperature-density distributions predicted by 2-D MHD calculations, and obtained from detailed x-ray measurements, assuming a thermonuclear mechanism.

At the Air Force Weapons Laboratory, we have been experimentally and theoretically investigating imploding plasma liners for production of high energy density plasmas for several years.[1,2,3] The plasma liner implosion experiments have resulted in large photon pulses[2,4] in the ultrasoft and soft x-ray range. Using the SHIVA capacitor bank - a 1.1 MJ, 1.2 microsecond, 100 KV device[2,5] which was later upgraded to 1.9 MJ, 1.4 microsecond, 120 KV, plasma liner implosions were driven in Z-pinch like, 7 to 12 MA discharges. These discharges resulted in ∿ 20 cm/microsecond final implosion velocities with 15 to 25% of the stored electrical energy converted to implosion kinetic energy. Photon pulse energies from 100 KJ to 240 KJ (assuming isotropic emission) were observed with FWHM of the pulses ranging from 80 to 200 nanoseconds. The best combined yield and FWHM was 240 KJ, 130 nanoseconds.

Observation geometry is illustrated in Figure 1. The photon diagnostics were arrays of x-ray photodiodes[6], x-ray pinhole cameras, thermocouple calorimeters, a fast pulsed bolometer[4], crystal and grating spectrographs. Passive detectors (calorimeters, pinhole cameras, spectrograph) were protected with pneumatic closure shutters[7] from plasma and debris blast.

Response functions of filtered x-ray photodiodes (XRD's) used are shown in Figure 2. KF is 250 microgram/cm^2 $C_{14}H_{16}O_3$ (Kimfoil), and FVis 75 microgram/cm^2 $C_5H_8O_2$ (Formvar). Cathode material and filter material are both listed for each XRD. For example, Al/FV means Aluminum cathode, Formvar filter. Unfiltered response functions used were those of Cairns and Samson[8] at low energy, Burns and Day[9] from 109 to 1487 eV, Gaines[10] et al from 185 to 1487 eV, Gaines[10] et al and Lyons[11] et al above 1.5 KeV. These agree closely with those of Day[12] et al and Henke[13] et al, except near the Oxygen absorption edge.

Seven XRD traces from a representative implosion experiment are shown in Figure 3. These traces were used to obtain deconvoluted or unfolded time resolved photon spectra using a technique outlined in "Figure" 4. This technique

is simular to those used by Chase and Salisbury[14], and by Plimpton and Glibert[15], except for the smoothing routines. The rapid variation of XRD response functions made it advantageous to use ratio energy zoning and a combined product/root - logarithmic interpolation smoother with smoothing intervals varying with iteration pass. Tests with hypothetical spectra such as black bodies, using flat initial spectra, gave good convergence[16] for 6 or more distinct XRD's. As is well known[14, 15], smoothing is necessary to avoid artificial spectral features resulting from edge jumps in the XRD response functions.

A three - dimensional plot of the time resolved deconvoluted spectrum obtained from the traces in Fig. 3 is shown in Fig. 5. The two low energy humps merge into a single hump peaking near 100 eV photon energy at peak power ($P \underset{\sim}{\sim} 1.26 \times 10^{12}$ watts, maximum $dP/dh\upsilon \sim 2 \times 10^{7}$ Megawatts/KeV). The highest energy peak, near 2 KeV photon energy, is due to $A\ell^{11+}$ and $A\ell^{12+}$ line and recombination radiation - the detail of which is unresolved using this analysis technique and this XRD array.

Fig. 6 shows peak power deconvoluted spectra for several representative implosion experiments, indicating the reproducibility of a low energy hump peaking near 100 eV photon energy.

A comparison of deconvoluted spectrum peak power vs. nominal peak power for photon emission is shown in "Fig." 7. Nominal peak power is obtained using an Aℓ/FV XRD, assuming an average response of 40 amperes/Megawatt for 60 micrograms/cm^2 Formvar filter. The difference is in all cases less than factor of 2 and often less than 20%. Thus, the Aℓ/FV XRD signal enables a rapid approximate estimate of photon emission yield for the spectra we have been obtaining.

2

Low energy crystal (lead stearate)[17] spectrograph data, such as shown in Fig 8, indicate that the spectrum below 220 eV in photon energy is dominated by continuum or closely packed lines, with possible absorption features. The lowest energy strong lines are $A\ell^{10+}$ 2p-3d (52.37Å) and $A\ell^{10+}$ 2s-3p (48.32Å). These are always evident and always quite strong in Aℓ or Aluminized plastic liner implosions. Comparison of stearate spectrograph data with XRD array unfolded spectra gives approximate (factor of 2) agreement near the carbon absorption edge (284 eV), as shown in Fig. 9. The crystal response reported by Henke[18] and Kodak RAR 2490 film response reported by Benjamin, Day, and Lyons[19] were used to absolutely interpret the spectrograph data.

Thermocouple calorimeter data, such as that shown in Fig. 10, was taken to check yields interpreted from XRD array data. The comparison, shown in "Fig." 11, shows that calorimeters indicate yields from 1 to 4 times those obtained with XRD data. This suggests that the calorimeter sensed late time energy in addition to the prompt photon energy detected by XRD's. This late time energy could be low energy photons from afterglow or late time discharge plasma and/or plasma and hot gases reaching the calorimeter. The fast (500 microsecond) closure shutter may be too slow to stop streaming plasma and hot gases on some shots.

A fast, pulsed, large signal bolometer was developed[4] and used to thermally detect photons with time resolution adequate to confirm that their origin is the implosion pinch. Bolometer signal traces with and without a photon pulse are shown in Fig. 12. The bolometers were used with 60 microgram/cm^2 Formvar filters to suppress surface photo-ionization shunting of the bolometer foil current after the prompt photon pulse. Such surface photo-ionization, suspected due to elongated rise times for unfiltered bolometers, is presumably due to lower energy afterglow photons still incident after the main (prompt) photon pulse. Rauch[20] and Hanson[21] have since used

similar bolometers, unfiltered, with magnets to suppress photoionization shunting, which has enabled faster time response and the use of unfiltered bolometers.

The interpreted yield for a Formvar filtered bolometer signal is compared to that for a Cu/FV XRD signal, vs. black body temperature for assumed black body spectral shape in Fig. 13. The agreement was better than or on the order of 30% for a wide range of temperatures, as well as for a variety of other plausible spectral shapes. Thus, both thermal and photoelectric detectors were in substantial agreement on photon yield.

A print of the data record obtained from a 5 meter grazing incidence spectrograph[22] is shown in Fig. 14. Al^{10+}, Al^{11+}, Al^{12+}, O^{6+}, O^{7+}, and C^{5+} emission lines are evident above 230 eV in photon energy. At lower energies, the spectrum is continuum with absorption lines from O^{4+}, O^{5+}, Al^{4+}, Al^{5+}. This indicates a hotter interior plasma shining through a cooler ($\sim$ 40 eV), absorbing plasma. Broadening of the Al^{12+} 2s-5p and 2s-6p lines exceeded instrumental broadening. If this broadening is assumed to be Stark broadening, one obtains an estimate of the electron density $\sim 10^{22}$ cm^{-3} for the part of the plasma emitting thoses lines.

Data from a KAP spectrograph, collimated to reduce source broadening, is shown in Fig. 15. The Al^{11+} and Al^{12+} K shell line and recombination radiation are evident. To the extent that the spectrum can be characterized by a single electron temperature T_e and electron density n_e, $T_e \gtrsim 400$ eV (from recombination slope) and $n_e \sim 10^{20}$ cm^{-3} (from He-like resonance line to intercombination line ratio)[23, 24]. Of course, the radiation is really from a time dependent, inhomogeneous temperature and density distribution.

By removing the spectral collimation slit and adding a spatial imaging slit, one obtains 2 dimensional spatial imaging of the spectral lines[25]. Imaging in the spectral dispersion direction is by source broadening, while in the other direction it is 1 dimensional pinhole imaging. In the 2 dimensional imaged KAP spectrograph record shown in Fig. 16, the magnification

by source broadening is approximately one third that by slit imaging, so the elliptical "annular" spectral lines are due to circular annular line emission regions[22].

In Fig. 17, an uncollimated KAP spectrograph densitometer trace is shown, illustrating the degree of source broadening. The best fit electron temperature and density are $\sim$ 300 eV and $\sim 10^{20}$ cm^{-3}, based on recombination slope and intensity.[22]

X-ray pinhole camera images, such as that shown in Fig. 18, often show an annular or ring shaped emission regions, as is also evident in some 2 demensional imaged KAP spectrograph records.[22]

Two dimensional magnetohydrodynamic calculations of plasma liner implosions predict electron density and temperature profiles similar to that shown in Fig. 19.[26] The axial plume and the ring shaped regions with high electron temperature are qualitatively consistent with the annular emission regions observed experimentally[22]. The predicted $\sim$ 40 eV plume temperature is consistent with the absorption lines seen in lower energy spectrograph data.[22]

Implosion experiments with deuterated aluminized plastic foil cylinders[27], in which the foils were 3% deuterium by mass and final implosion velocities were $\sim$ 20 cm/micosecond, resulted in neutron yields $\sim 10^7$ to 10^8. A comparison of yields obtained from Ag activation and lead shielded scintillator - photomultiplier detector data is shown in "Fig." 20. The detectors were calibrated in situ with a pulsed neutron source and cross - calibrated with a large Ag detector previously calibrated at Livermore[28]. The observed yields were approximately consistent with those obtained by applying Rose and Clark neutronics[29] to two dimensional magnetohydrodynamic

predictions of ion temperature and density spatial and temporal distributions.

Ongoing and future work includes experiments with faster implosions driven by capacitor bank discharges sharpened using inductive storage, opening switch techniques.[30, 31,32, 33]. The use of time and space resolved spectrographs will be emphasized in this work.

REFERENCES

1. P.J. Turchi and W.L. Baker, J. Appl. Phys. 44, 4936 (1973)

2. W.L. Baker, M.C. Clark, J.H. Degnan, G.F. Kiuttu, C.R. McClenahan , R.E. Reinovsky, J. Appl. Phys. 49, 4694 (1978)

3. T.W. Hussey, N.F. Roderick, D.A. Kloc, J. Appl. Phys. 51, 1452 (1980); N.F. Roderick, T.W. Hussey, R.J. Faehl, R.W. Boyd, Appl. Phys. L. 32, 273 (1978)

4. J.H. Degnan, Rev. Sci. Inst. 50, 1223 (1979)

5. G. Barton and D. Markins, Maxwell Laboratories, Report No. AFWL-TR-75-271 (1975)

6. D.J. Johnson, Report No. AFWL-TR-74-43 (1974)

7. R.E. McDonald of Lockheed Palo Alto Research Laboratories (and now of Spectral Precesion, Inc.) provided pneumatic fast closure shutter design.

8. R.B. Cairns and J.A.R. Samson, J. Opt. Soc. Am. 56, 1568 (1968)

9. E.J.T. Burns and R.H. Day, private communication; E.J.T. Burns and J.F. Thurston, Appl. Spect. 31, 317 (1977)

10. J.L. Gaines and R.D. Ernst, Report No. UCIR-1075 (1956); J.L. Gaines, private communication.

11. P.B. Lyons, private communication

12. R.H. Day, P. Lee, E.B. Salomen, D.J. Nagel, Report No. LA-UR-79-1360 (1979)

13. R.L. Henke, J.P. Knauer, K. Premeratne, Bull. Am. Phys. Soc. 24, 1098 (1979)

14. L. Chase and S. Salisbury, private communication

15. J. Plimpton and K. Glibert, private communication

16. J.H. Degnan, R.E. Reinovsky, G.F. Kiuttu, M.C. Clark, W.L. Baker, IEEE Conference Record - 1978 IEEE International Conference on Plasma Science, P. 50 (1978)

17. The lead stearate crystals were fabricated and supplied by B.L. Henke.

18. B.L. Henke and M.A. Tester, Adv. in X-ray Analysis, edited by W.L. Pickles, C.S. Barrett, J.B. Newkirk, C.O. Rund (Plenum, New York, 1975) Vol. 18, p. 76

19. R.F. Benjamin, P.B. Lyons, and R.H. Day, Report No. LA-UR-76-1502 (1975)

20. John Rauch, Report No. MLR 933 (1980)

21. D.L. Hanson, R.B. Spielman, J.P. Anthes, Bull. Am. Phys. Soc. 25, 890 (1980)

22. D.M. Woodall, J.H. Degnan, G.F. Kiuttu, R.J. Sand, R.E. Reinovsky, W.L. Baker, Bull. Am. Phys. Soc. 25 872 (1980)

23. E.J.T. Burns, J.H. Degnan, R.E. Reinovsky, W.L. Baker, M.C. Clark, C.R. McClenahan, Appl. Phys. L. 31, 477 (1977)

24. A.H. Gabriel and C. Jordan, Case Studies in Atomic Collision Physics, edited by E.W. McDaniel and M.R.C. McDowell (North-Holland, Amsterdam, 1972) Vol. 2, Chapter 4; C.P. Bhalla, A.H. Gabriel, and L.P. Presnykov, Mon. Not. R. Astron Soc. 172, 359 (1975)

25. G.F. Kiuttu, AFWL-DYP-TN-79-117 (1979)

26. T.W. Hussey, N.F. Roderick, D. Kloc, private communication

27. W.L. Baker, C.W. Beason, J.H. Degnan, G.F. Kiuttu, D.A. Kloc, R.A. Nuttleman, R.E. Reinovsky, R.J. Sand, D.M. Woodall, Bull. Am. Phys. Soc. 25, 834 (1980)

28. D.R. Slaughter and W.L. Pickles, Report No. UCRL-81137 (1978)

29. D.J. Rose and M. Clark, Plasmas and Controlled Fusion (MIT Press, Cambridge, Mass., 1961)

30. C.R. McClenahan, J.H. Goforth, J.H. Degnan, R.M. Henderson, W.H. Janssen, W.E. Walton, Report No. AFWL-TR-78-130 (1980)

31. D.L. Smith, R.P. Henderson, and R.E. Reinovsky, 2nd IEEE International Pulse Power Conference - Digest of Technical Papers, P. 287 (1979)

32. R.P. Henderson, D.L. Smith, and R.E. Reinovsky, 2nd IEEE International Pulse Power Conference - Digest of Technical Papers, P. 347 (1979)

33. W.L. Baker, J.H. Degnan, J.F. Francis, R.P. Henderson, J.R. Kerns, R.E. Reinovsky, and R.J. Sand, IEEE Conference Record - 1981 IEEE International Conference on Plasma Science, P. 63 (1981)

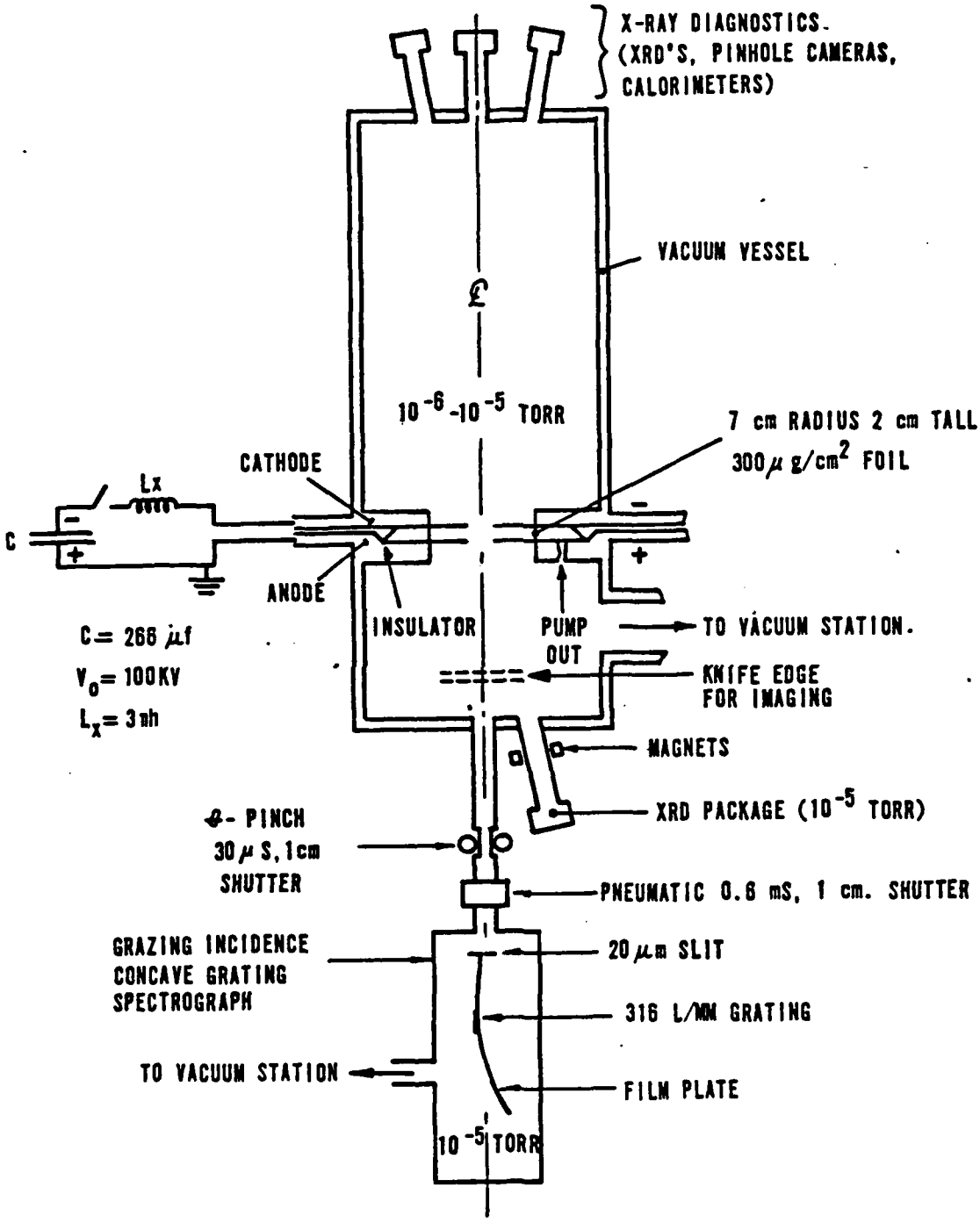

FIGURE 1.

SCHEMATIC OF SHIVA DIAGNOSTIC GEOMETRY
WITH GRATING SPECTROGRAPH
(NOT TO SCALE)

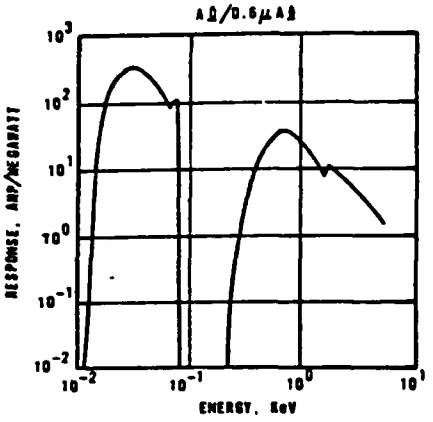

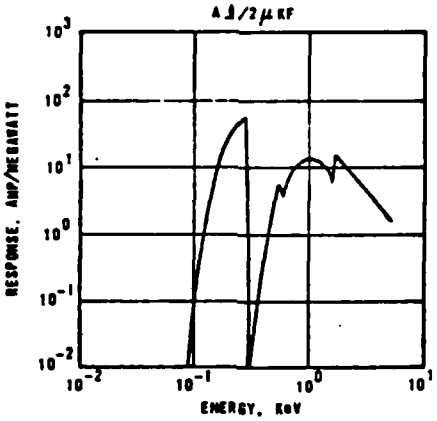

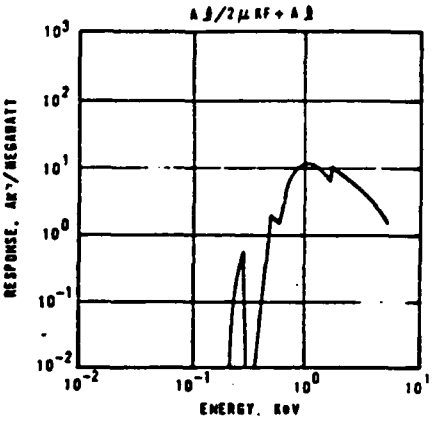

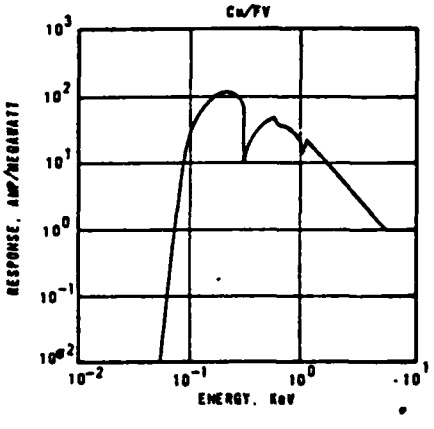

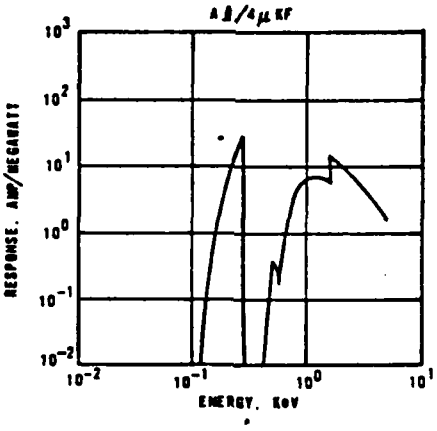

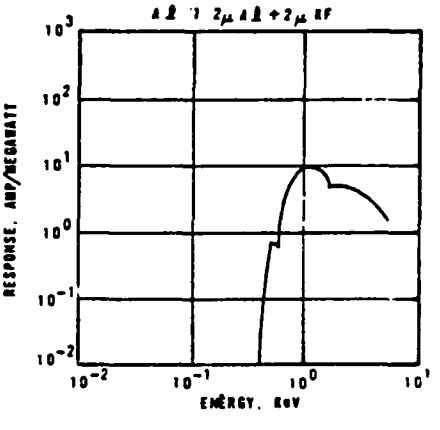

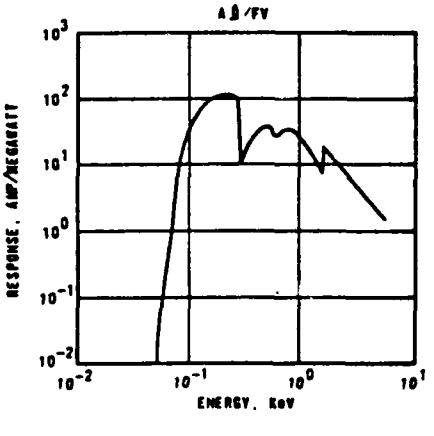

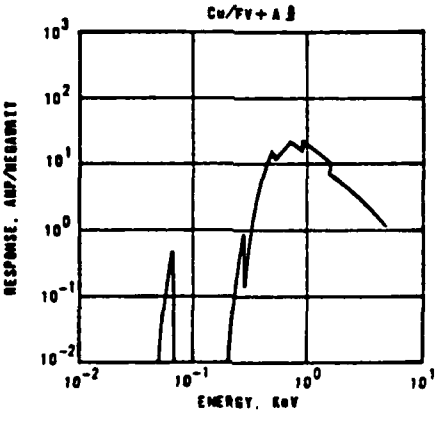

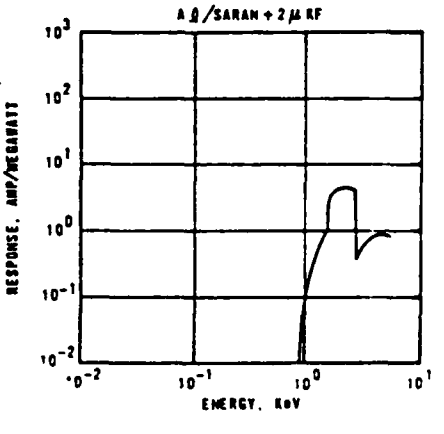

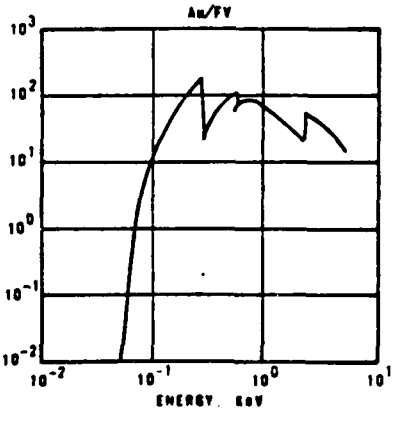

Filtered XRD Response Curves

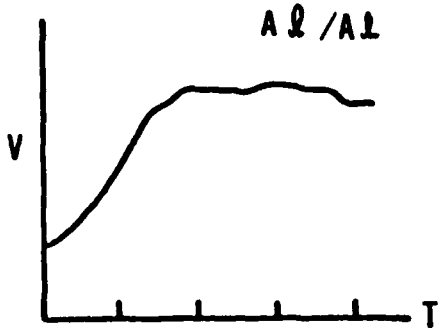

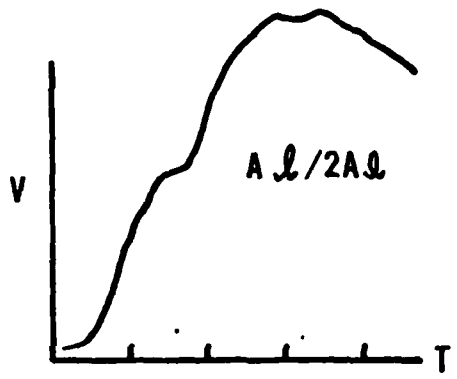

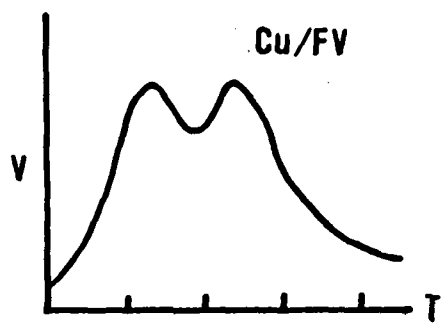

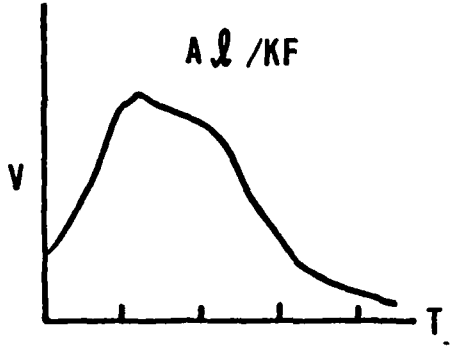

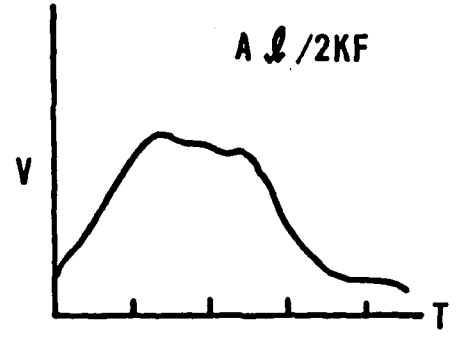

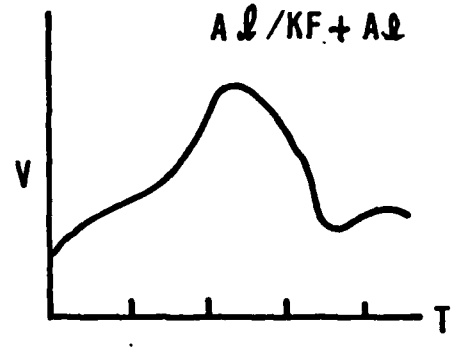

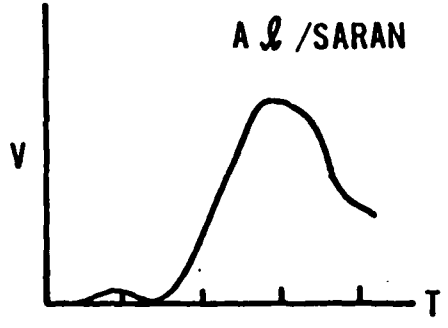

SHIVA SHOT 3220 XRD SIGNALS (50 NANOSECONDS/DIVISION)

$P_{NOM} = 1.64 \times 10^{12}$ WATTS

USING AN ARRAY OF FILTERED XRDs, ONE CAN DECONVOLVE, OR "UNFOLD", A SMOOTH TIME-DEPENDENT RADIATION SPECTRUM CONSISTENT WITH THE ARRAY OF SIGNALS. THE TECHNIQUE IS THE SAME USED TO INTERPRET UNDERGROUND TEST DATA. GIVEN XRD SIGNALS $V_K(T)$ AND RESPONSE FUNCTIONS $R_K(E)$, THE ITERATION EQUATIONS ARE

$$VC_K = \int R_K(E)\, S(E)\, dE \qquad (1)$$

$$S^1(E) = S(E)\, \frac{\sum_K R_K(E)\ (V_K / VC_K)}{\sum_K R_K^1(E)} \qquad (2)$$

WHERE $VC_K(T)$ = CALCULATED SIGNAL,
$S(E)$ = TRIAL SPECTRUM,
$S^1(E)$ = CORRECTED SPECTRUM,

AND $$R_K^1(E) = R_K(E) / \int R_K(E)\, dE. \qquad (3)$$

A FLAT SPECTRUM IS USED TO INITIATE THE ITERATION PROCESS. TWO DIFFERENT SMOOTHING TECHNIQUES ARE INCORPORATED TO INSURE CONVERGENCE.

COMPUTATIONAL STUDIES, SUCH AS HYPOTHETICAL BLACKBODY UNFOLD TESTS, INDICATE THAT AT LEAST 6 OR 7 DIFFERENT DETECTORS ARE NEEDED TO UNFOLD SMOOTH SPECTRA IN THE 10-1000 EV RANGE.

TOP 7 3220

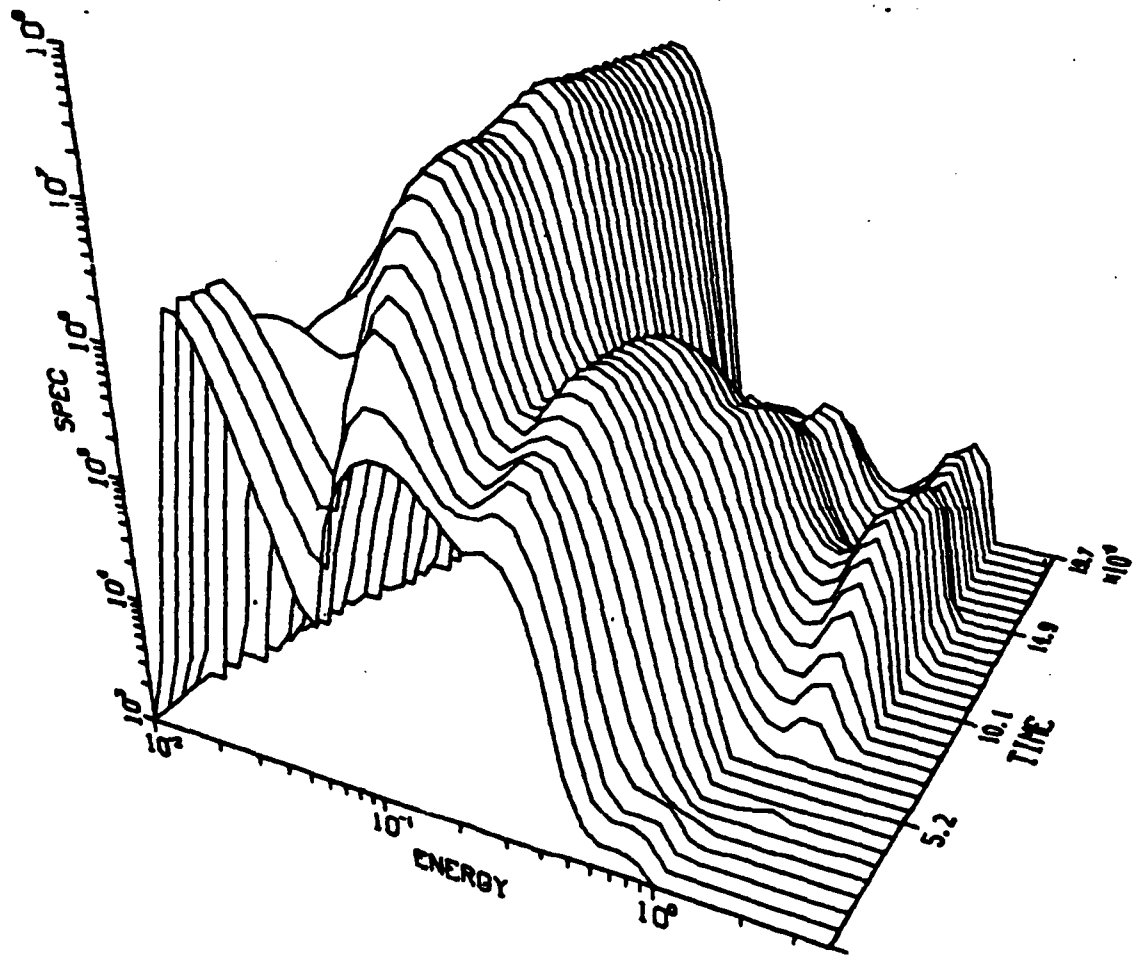

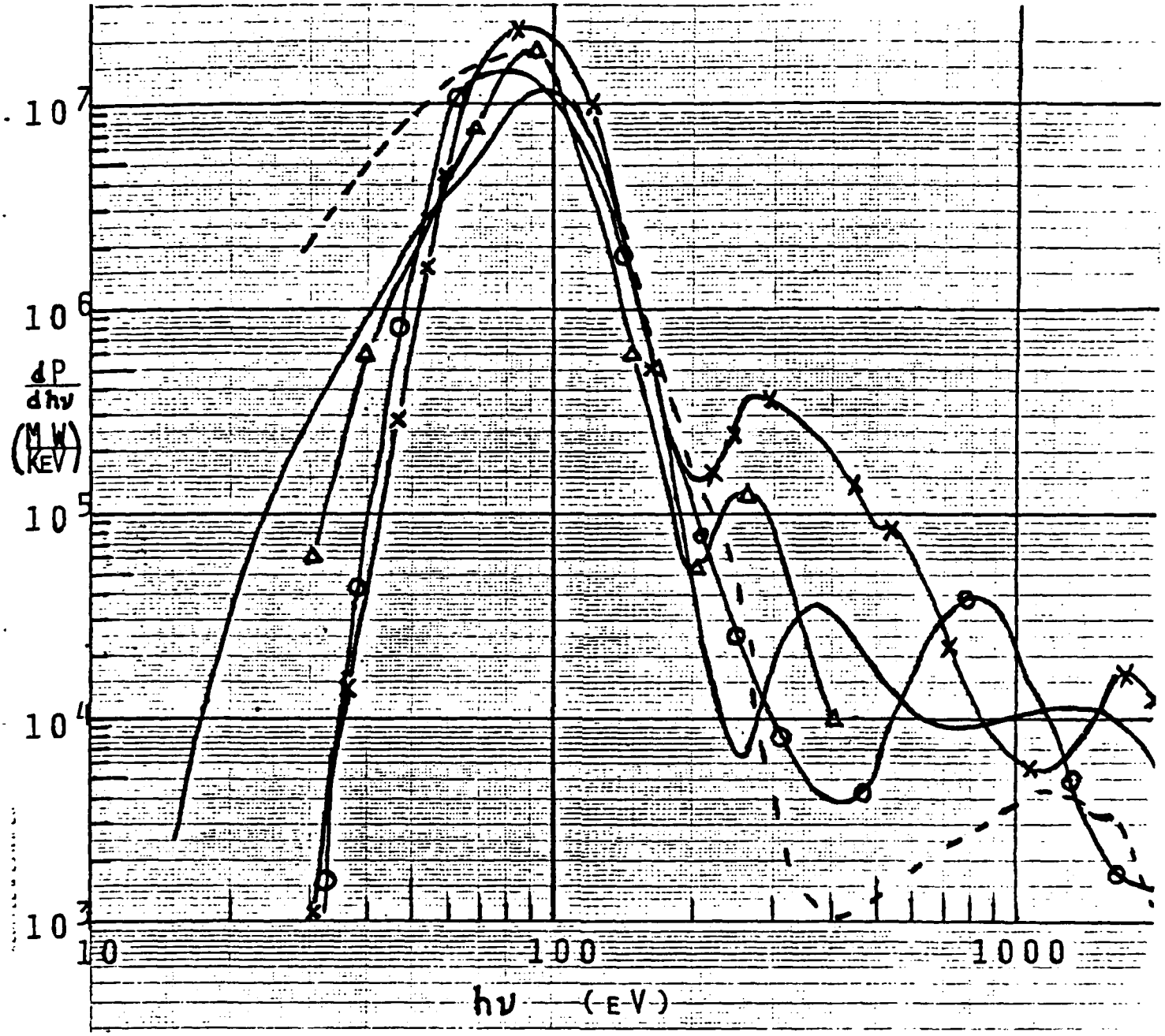

THE MOST REPRODUCIBLE FEATURES OF PHOTON SPECTRA DECONVOLUTED FROM XRD ARRAYS ARE A MAIN PEAK NEAR 100 eV AND A SMALL PEAK IN THE 1-2 KeV RANGE. THE LATTER IS AL^{11+} AND AL^{12+} LINE AND RECOMBINATION RADIATION WHOSE DETAILS ARE NOT RESOLVED.

COMPARISON OF DECONVOLUTED SPECTRUM PEAK POWER vs. NOMINAL PEAK POWER

SHOT	P_{DC}/P_{NOM}
3125	0.6
3146	1.0
3158	1.57
3169	0.89
3177	1.08
3186	0.95
3187	0.87
3190	1.41
3191	1.79
3213	0.96
3220	0.80

NOMINAL PEAK POWER IS OBTAINED FROM FV FILTERED AL CATHODE XRD SIGNAL, ASSUMING AVERAGE RESPONSE = 40 AMPERES/MEGAWATT.

RATIO OF DECONVOLUTED SPECTRUM PEAK POWER TO NOMINAL PEAK POWER WAS IN ALL CASES BETWEEN 0.5 AND 2, AND WAS USUALLY ABOVE 0.8.

LEAD STEARATE SPECTROGRAPH DATA

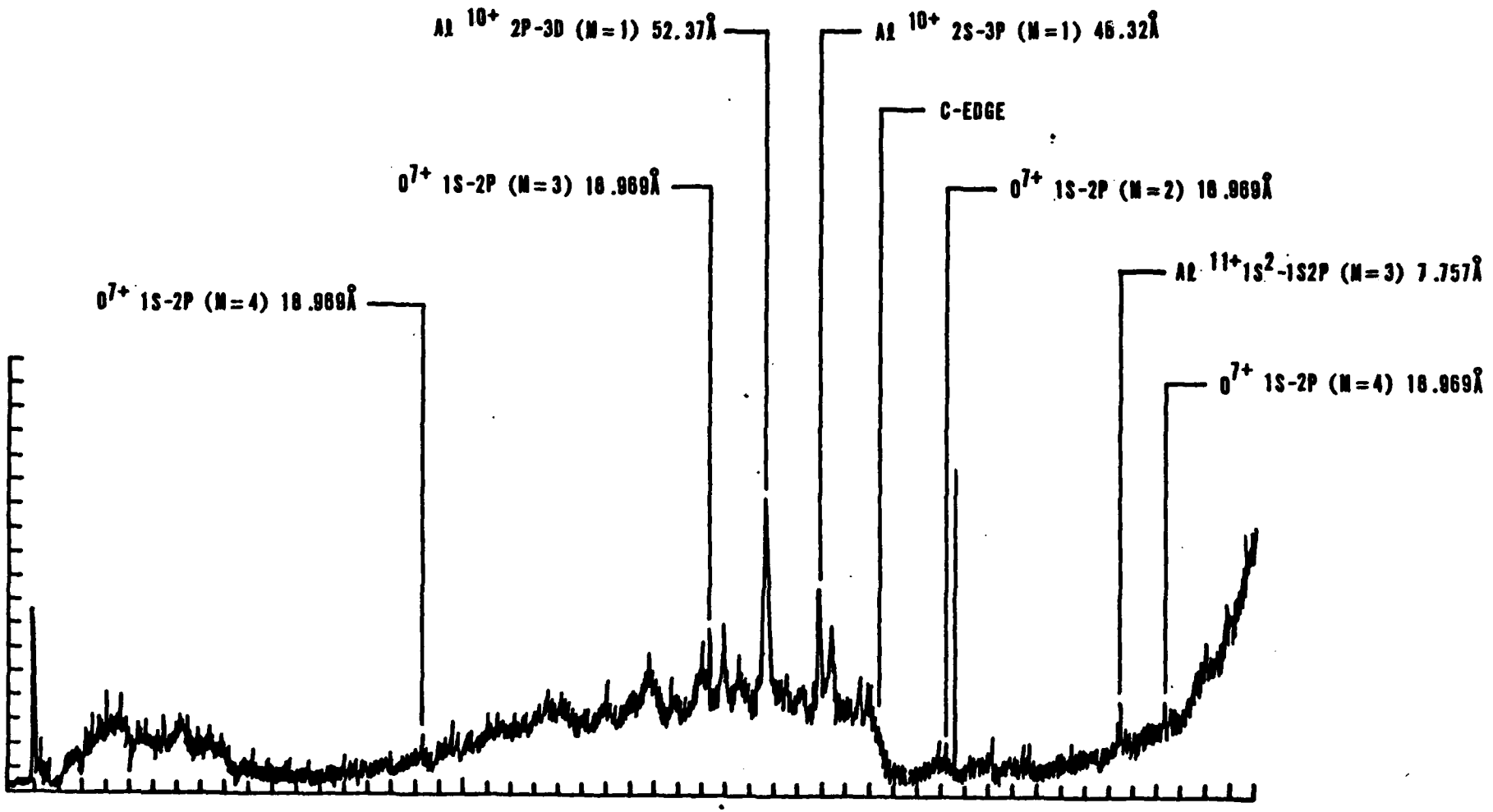

Comparisons of lead stearate specrograph data (interpreted for absolute spectral energy density) with spectra deconvoluted from XRD array data were in approximate agreement near the C absorption edge – at which energy the spectrograph response is best known.

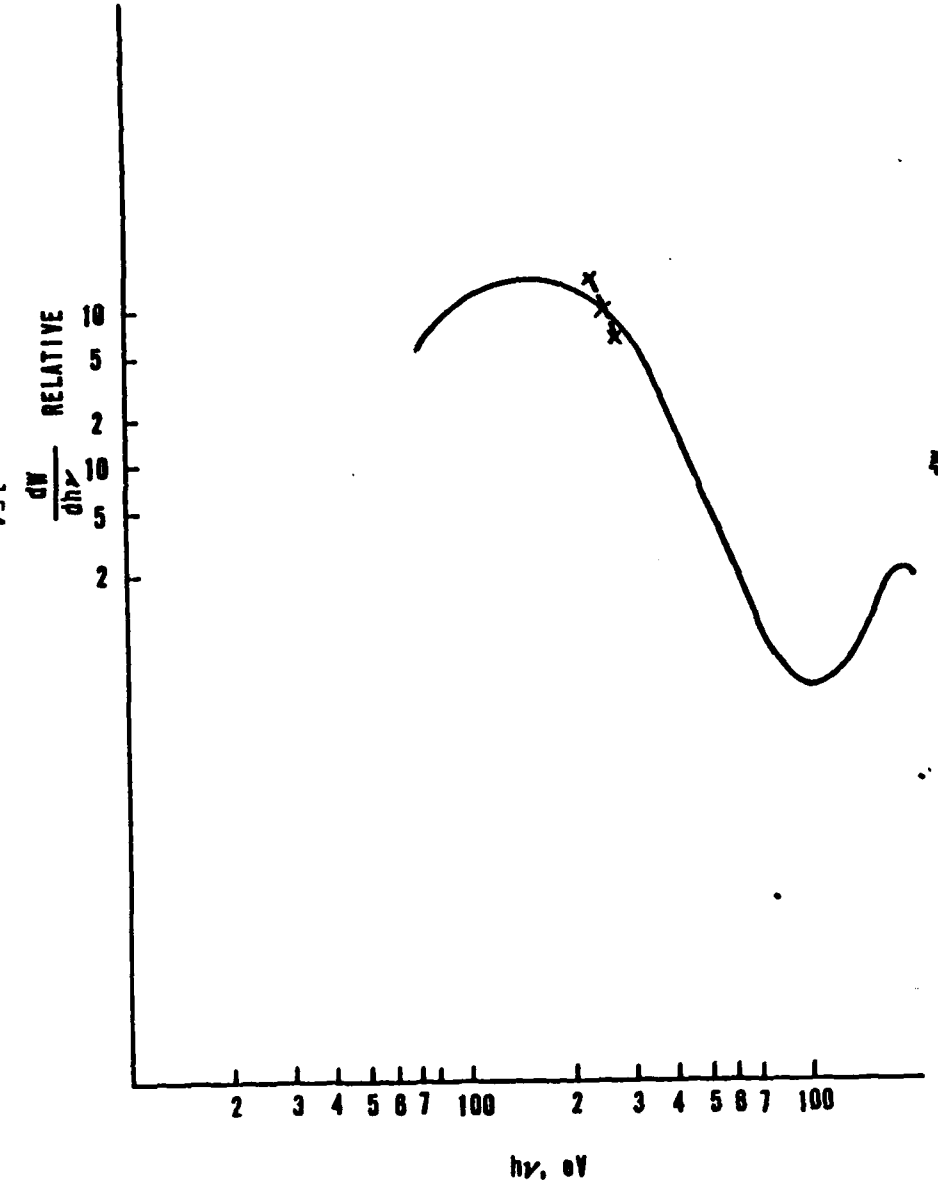

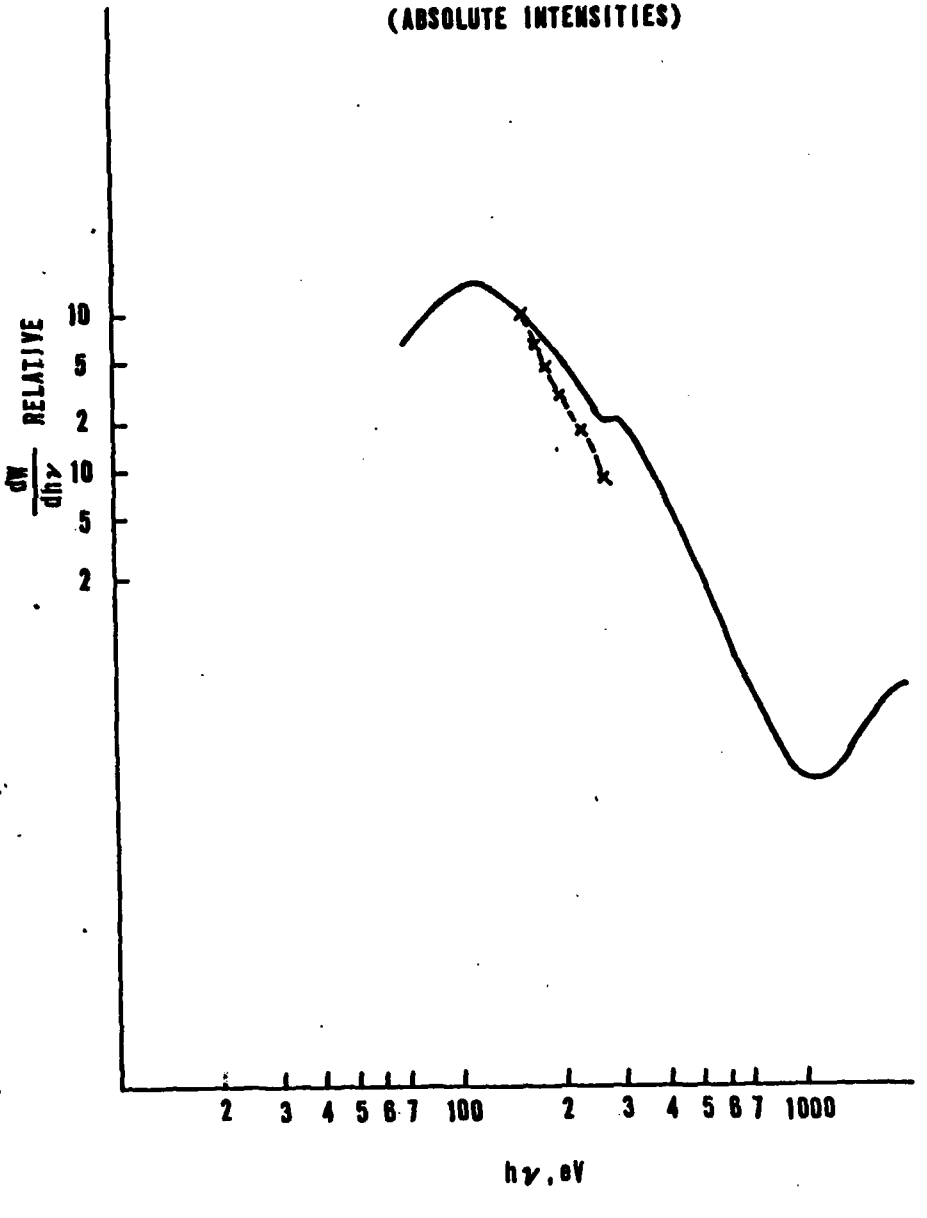

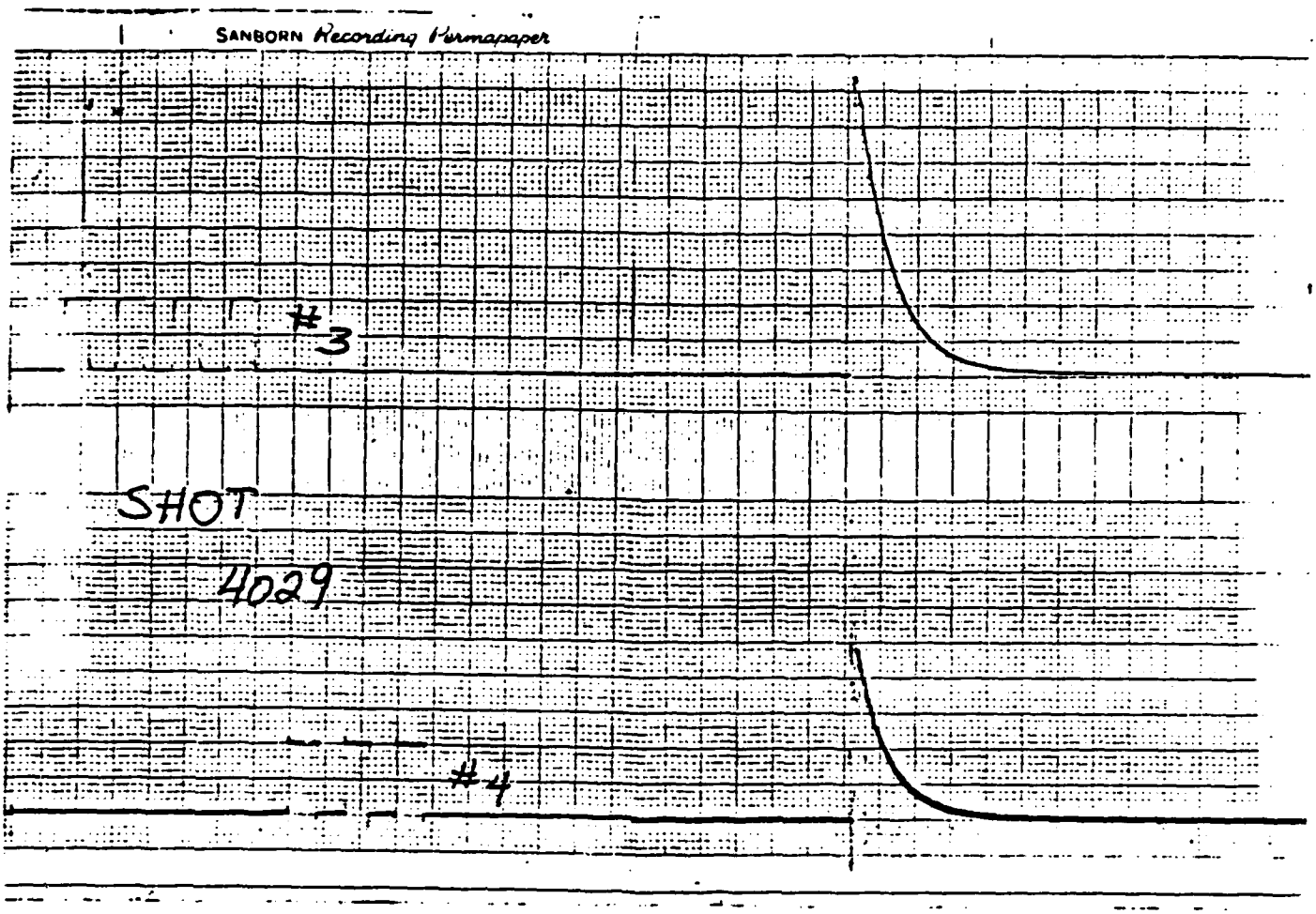

CALORIMETER TRACES

20 μV / SMALL DIVISION

700 JOULES / μV

#3 BARE

#4 60 μG / CM^2 $C_5H_8O_2$ FILTER

CALORIMETER - XRD COMPARISON

SHOT	Y_{CAL}/Y_{XRD}
3187	1.97
3190	1.02
3191	0.82
3222	1.80
3223	2.60
3224	3.90
3226	3.80

BARE CALORIMETER DATA SUGGESTED YIELDS BETWEEN 1 AND 4 TIMES NOMINAL YIELDS OBTAINED FROM XRD DATA. THIS SUGGESTS THAT CALORIMETER SENSED LATE TIME ENERGY, POSSIBLY DUE TO INADEQUATE SPEED OF BLAST CLOSURE SHUTTERS, ON SOME SHOTS.

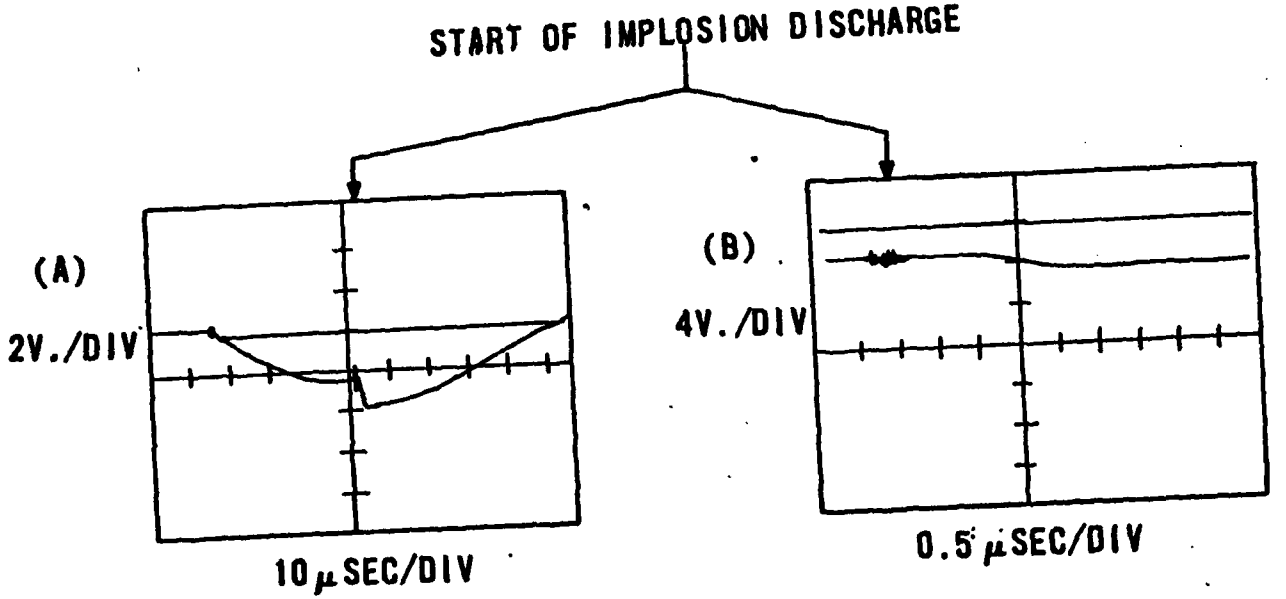

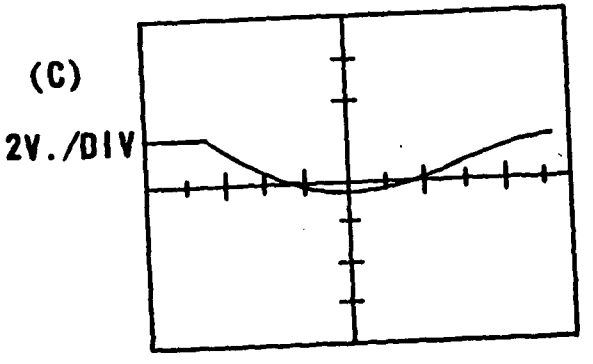

BOLOMETER SIGNAL TRACES

(A), (B) : with x-rays

(C) : without x-rays

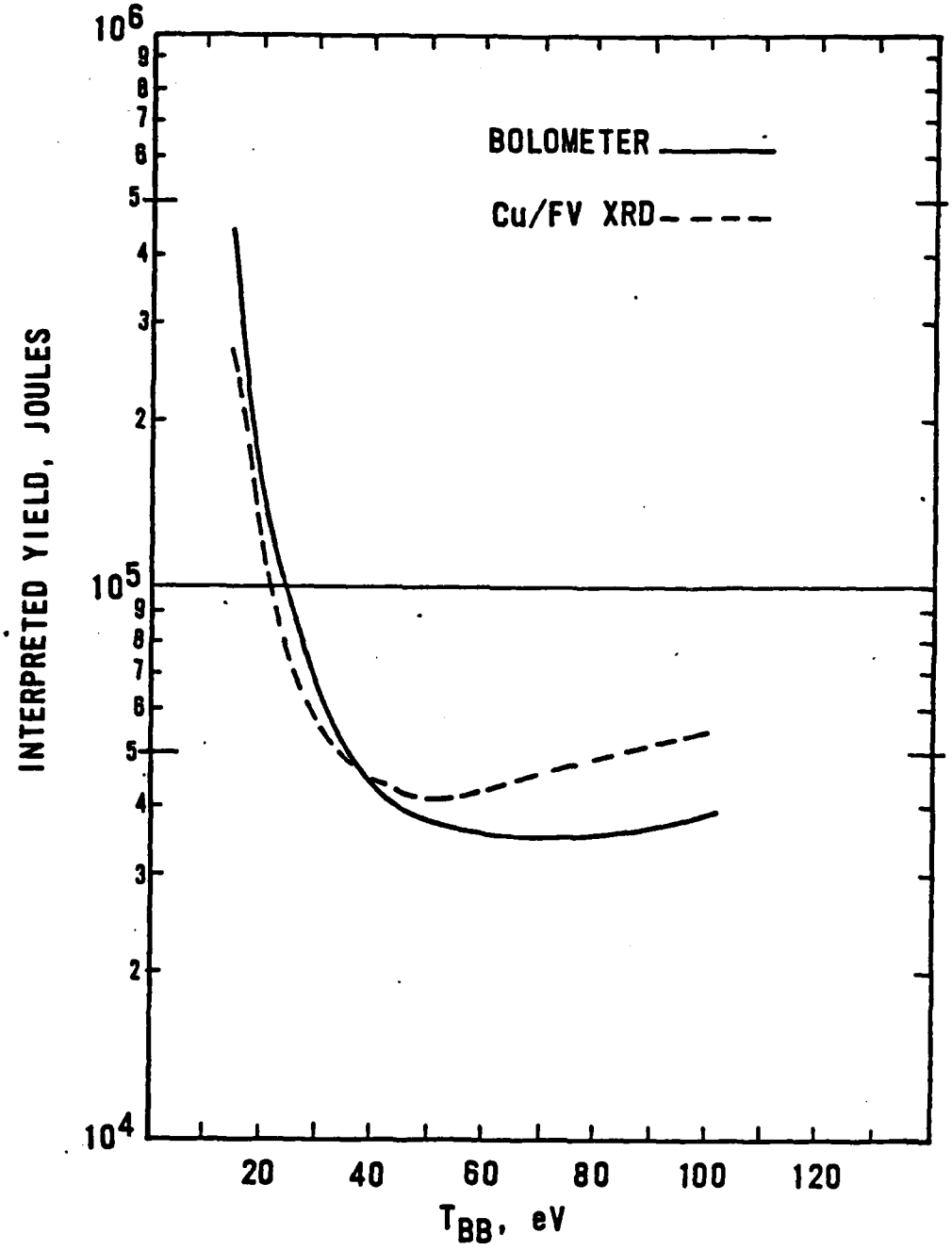

FAST PULSED BOLOMETER DATA AGREED SUBSTANTIALLY WITH XRD DATA ON PHOTON ENERGY YIELD. THIS AGREEMENT WAS BETTER THAN OR ON THE ORDER OF 30% FOR A WIDE RANGE OF ASSUMED SPECTRAL SHAPES.

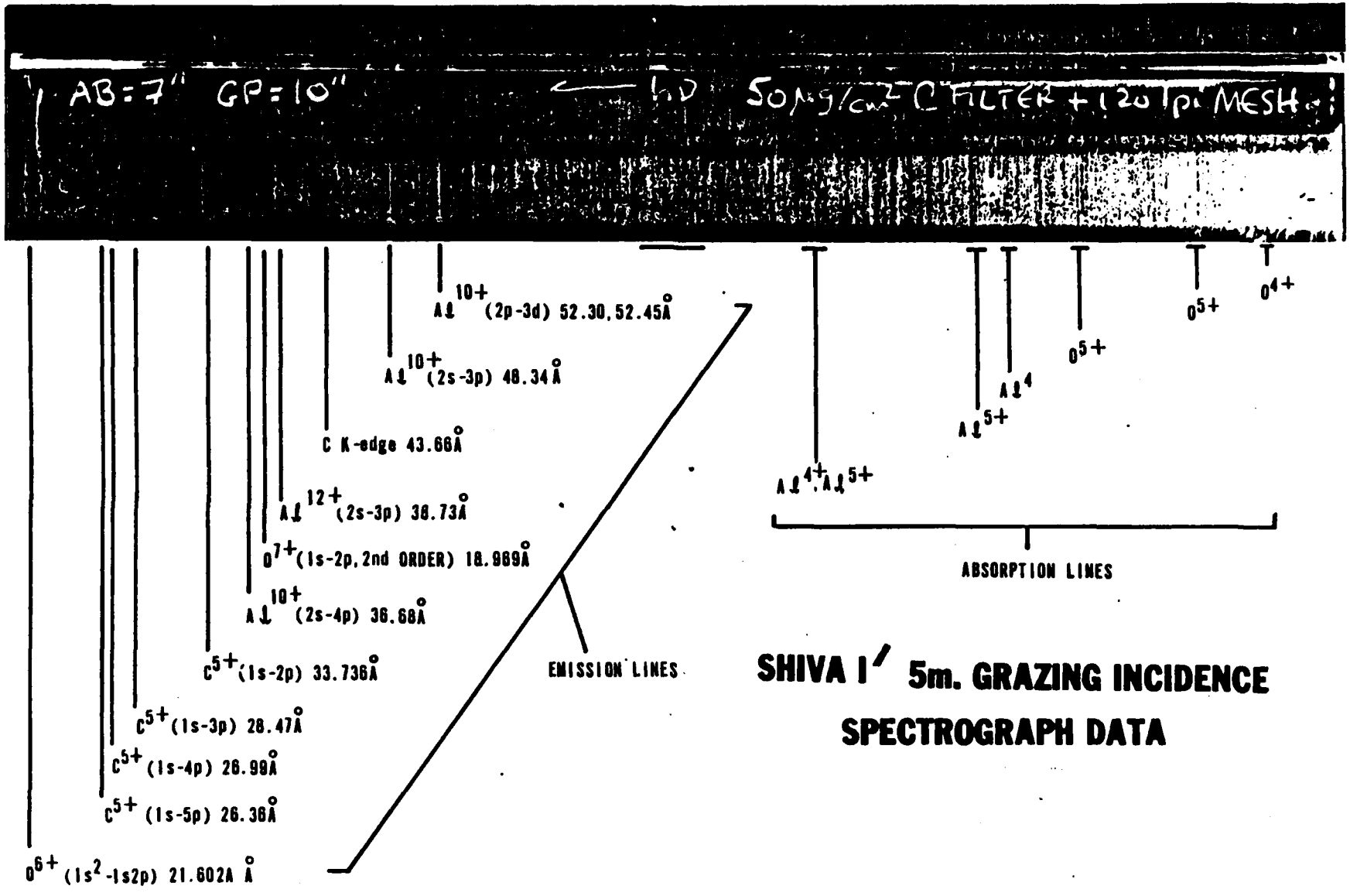

SHIVA I′ 5m. GRAZING INCIDENCE SPECTROGRAPH DATA

BY REMOVING THE ENTRANCE APPERTURE TO THE KAP CURVED CRYSTAL SPECTROGRAPH AND INSERTING AN IMAGING SLIT PERPENDICULAR TO THE CRYSTAL AXIS, TWO-DIMENSIONAL IMAGES OF THE PINCHED PLASMA HAVE BEEN OBTAINED AT DISCREET WAVELENGTHS IN THE AL 11^+ AND 12^+ 1S-NP LINE SERIES.

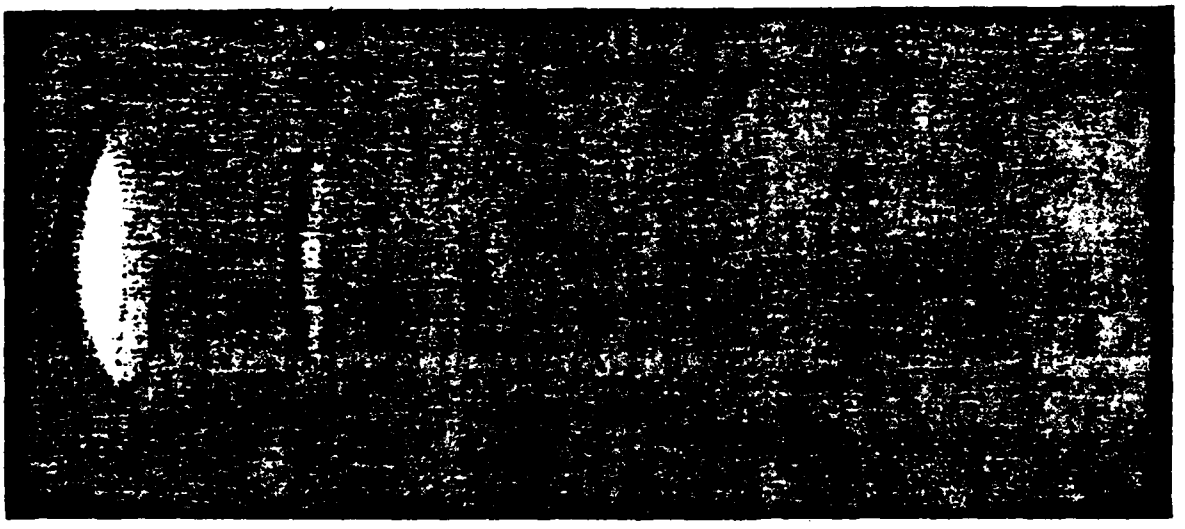

$1s^2$-1s2P 7.757A

$1s^2$-1s3P 6.635A

1s-3P 6.053A

1s-2P 7.176A

$1s^2$-1s4P 6.314A

$1s^2$-1s5P 6.180A

KAP SPECTROGRAPH DATA

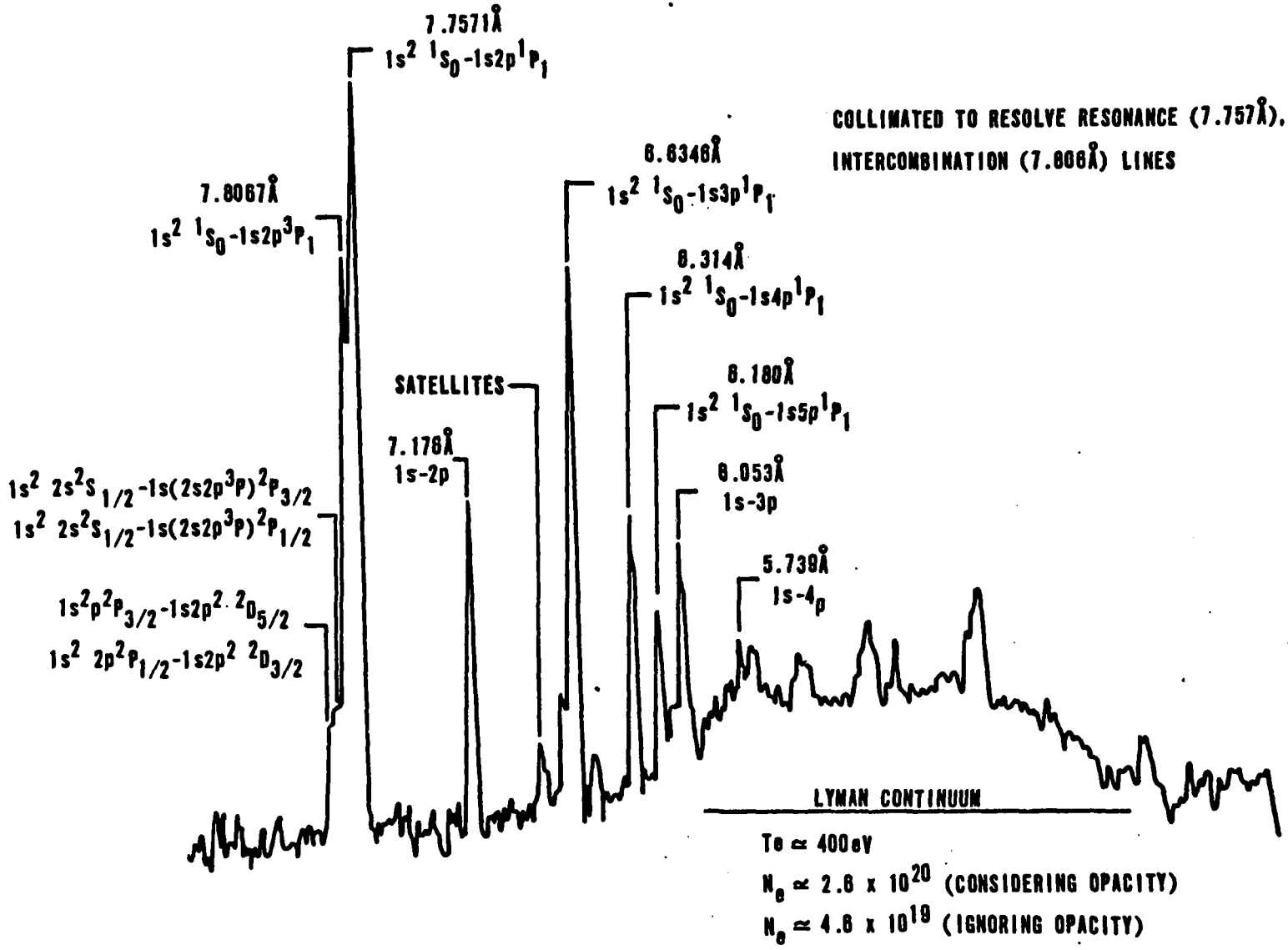

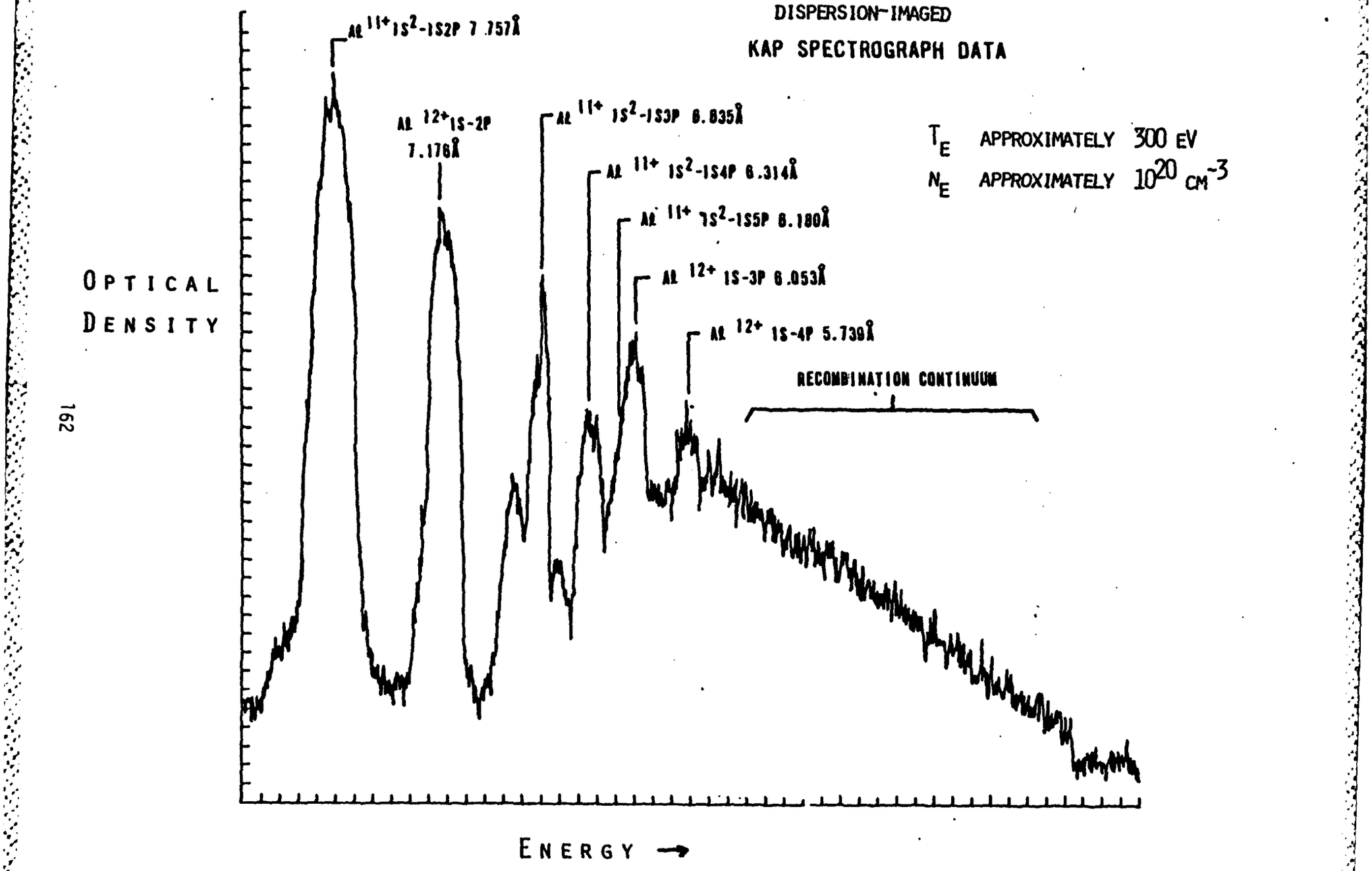
DISPERSION-IMAGED
KAP SPECTROGRAPH DATA
Al 11+ 1S2-1S2P 7.757Å
Al 12+ 1S-2P 7.176Å
Al 11+ 1S2-1S3P 6.835Å
Al 11+ 1S2-1S4P 6.314Å
Al 11+ 1S2-1S5P 6.180Å
Al 12+ 1S-3P 6.053Å
Al 12+ 1S-4P 5.739Å
RECOMBINATION CONTINUUM
T_E APPROXIMATELY 300 eV
N_E APPROXIMATELY 10^{20} cm^{-3}
OPTICAL DENSITY
ENERGY →

THE TWO-DIMENSIONAL IMAGES OF HIGHER ENERGY RADIATION FROM PINHOLE CAMERA AND DISPERSION-IMAGED SPECTROGRAPH DATA ARE CONSISTENT WITH THE PINCHED PLASMA DENSITY AND TEMPERATURE PROFILES CALCULATED WITH 2-D MHD SIMULATION CODES.

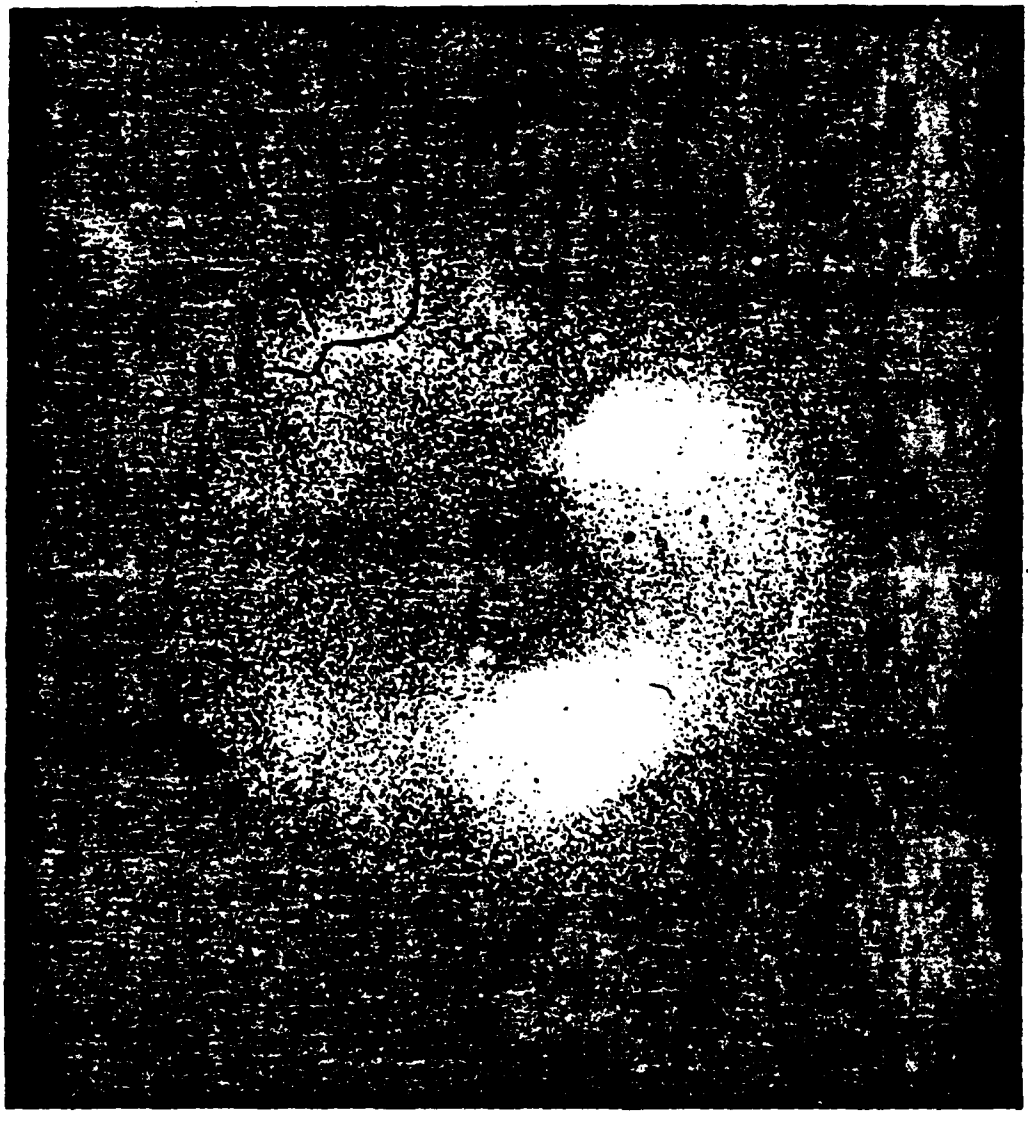

X-RAY PINHOLE PHOTOGRAPH OF THE PINCH SHOWING ANNULAR EMISSION PATTERN. FILM WAS KODAK 2490 RAR. ENERGY RANGE .8-2 KEV.

2D-MHD PREDICTIONS OF IMPLODING LINER PINCH STRUCTURE AT REPRESENTATIVE TIME DURING RADIATION PULSE

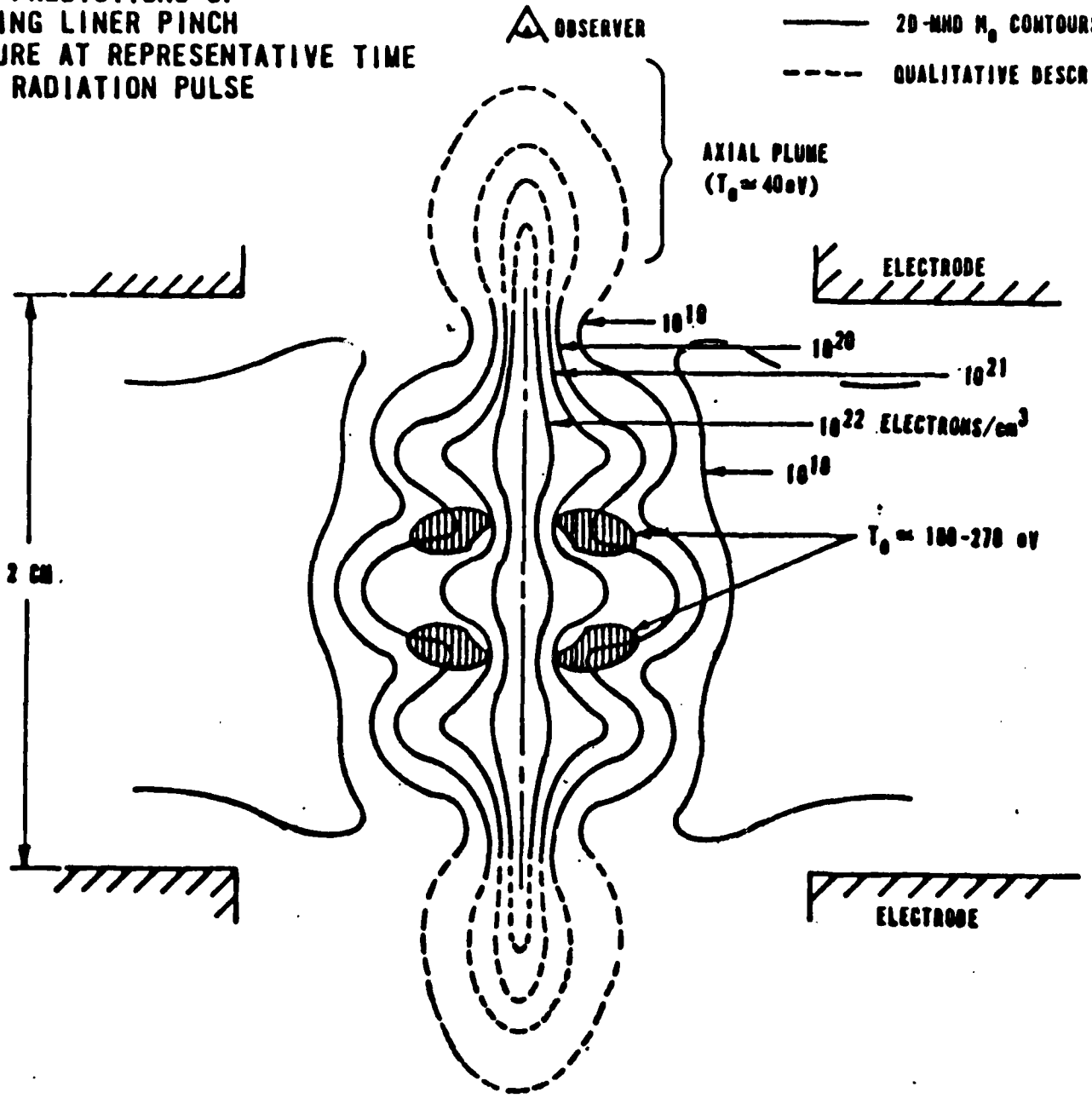

COMPARISON OF ACTIVATION & TOF DATA

SHIVA SHOT	SILVER ACTIVATION NOMINAL NEUTRON YIELD	TOF NOMINAL NEUTRON YIELD
4028	6.60×10^7	7.40×10^7
4029	2.44×10^7	1.45×10^7
4030	3.20×10^6	4.40×10^6
4039	1.12×10^8	1.22×10^8
4040	2.19×10^7	2.70×10^7
4044	4.15×10^7	
4045	1.25×10^7	1.30×10^7
4046	1.68×10^7	3.50×10^7
4047	2.58×10^7	3.80×10^7
4048	1.00×10^7	1.50×10^7
4049	1.21×10^8	
4052	4.56×10^8	
5017	1.07×10^6	
5021	2.52×10^6	
5024	1.48×10^7	

Acknowledgements

The deconvolution technique is similar to that used by L. Chase and J. Salisbury of LPARL, and by J. Plimpton and K. Glibert of SNL.

The related contributions of W.L. Baker, E. J. T. Burns, R.H. Day, B.L. Henke, T.W. Hussey, J.D. Letterio, R.E. Reinovsky, N.F. Roderick, and others are acknowledged and appreciated.

REFERENCES

1. Thode, L. E. and Sudan, R. N., Phys, Fluids 18, 1552 (1975) and Phys. Fluids 18, 1564 (1975.
2. Thode, L. E., Phys. Fluids 19, 305 (1976).
3. Thode, L. E., Phys. Fluids 20, 2121 (1977).
4. Sethian, J. D. and Ekdahl, C. A, Phys. Rev. Lett. 42, 711 (1979).
5. Clark, M. C., "Foilless Diode Operation on a 7 MeV, 80 kA Electron Beam Machine," Bull. Am. Phys. Soc. 74, 1085 (1979).
6. Cheng, D. Y., Nuclear Fusion 10, 305 (1970).
7. Cheng, D. Y., "The Application of a Deflagration Gun to Fusion Systems," Proc. of High Beta Workshop, Los Alamos (1975), p. 681.
8. Clark, M. C., "Transport and Stability of a Magnetized Electron Beam Propagating Through Neutral Gas," Bull. Am. Phys. Soc. 25, 913 (1980).
9. H. R. Griem, Plasma Spectroscopy, McGraw-Hill, Inc., New York, 1964.
10. H. R. Griem, Spectral Line Broadening of Plasmas, Academic Press, New York, 1974.
11. W. L. Wiese, D. R. Pagnette, and J. E. Solarski, Phys. Rev., 129, 1225 (1963).
12. R. H. Huddlestone and S. L. Leonard, editors, Plasma Diagnostic Techniques, Academic Press, New York, 1965.
13. W. Lochte-Holtgreven, editor, Plasma Diagnostics, North-Holland Publishing Company, Amsterdam, 1968.
14. P. R. Bevington, Data Reduction and Error Analysis for the Physical Sciences, McGraw-Hill, Inc., New York, 1969.
15. See, for example, integrals 190 and 191 in Standard Mathematical Tables, 18th Student Edition, published by the Chemical Rubber Company.
16. A. Kuthy, Nucl. Inst. and Meth., 180, 7 (1981).
17. A.P.G. Kuthy, J. Appl. Phys., 50, 6139 (1979).
18. W. L. Baker et al, JAP 49, 4694 (1978).
19. The shutter design was obtained from Lockheed Palo Alto Research Labs.
20. Bank is a Magneform unit, from Maxwell Laboratories, Inc.
21. Grazing Measurements, Ltd., London, England.
22. M. G. Hobby and N. J. Peacock, J. Phys. E, Sci. Inst. 6, 854 (1973).
23. R. Speer, private communication.
24. G. F. Kiuttu, et al, Bull. Am. Phys, Soc. 24, 1057 (1979).
25. J. H. Degnan, et al, Bull. Am. Phys, Soc. 24, 1057 (1979).

26. B. Kohn, D. Kloc, and T. Hussey, private communication.
27. J. H. Degnan, et al, IEEE Int. Conf. on Plasma Sciences, Monterrey, Calif. (1978), p. 50, Conference Record.
28. P. C. Kepple and H. R. Griem, "Stark Profile Calculations for Lyman Series Lines of One Electron Ions in Dense Plasmas," NRL Memorandum Report 3634 (1978).
29. Jones, M. E. and Thode, L. E., "Theory and Simulation of Foilless Diodes," Bull. Am. Phys. Soc. 24, 977 (1979).
30. Newberger, B. S. and Thode, L. E., "Linear Theory of a Scattered Changed Particle Beam Interacting with a Collisional Plasma," Bull. Am. Phys. Soc. 24, 1097 (1979).
31. Thode, L. E., Cary, J. R., Jones, M. E., Mostrom, Newberger, B. S. and Clark, M. C., "Potential for Anomalous Generation of High Energy Density Plasma to Drive Hybrid Inertial Confinement Devices," Abstracts of IEEE Int'l Conf. on Plasma Sci, Madison, WI, 1980, p. 23.
32. Newberger, B. S., "Competition between Filamentation and Two-Stream Instabilities in a 'Cool' Relativistic Electron Beam," Bull. Am. Phys. Soc. 25, 853 (1980).
33. Jones, M. E., Mostrom, M. A. and Thode, L. E., "Analytical and Numerical Studies of Foilless Diodes," Bull. Am. Phys. Soc 25, 840 (1980).
34. Thode, L. E., Jones, M. E., Mostrom, M. A. and Morr, D. C., "Electromagnetic (Filamentation) Interaction Between a Scattered Relativistic Electron Beam and a Finite Temperature, Collisional Plasma," Bull. Am. Phys. Soc. 25, 1037 (1980).
35. Riepe, K. B., et al, "A High-Density Plasma Source Using a Current Driven Ionizing Shock Wave," Bull. Am. Phys. Soc. 25, 959 (1980).
36. Sheffield, R. L., et al., "Interaction of a Highly Collimated Intense Relativistic Electron Beam with Hydrogen," Bull. A.m. Phys. Soc. 25, 1039 (1980).
37. Len, L. K., Woodall, D. M., and Ekdahl, C. A., "Production of a High Density Plasma Target for REB Heating Experiments," Bull. Am. Phys. Soc. 25, 1011 (1980).
38. Kiuttu, G. F., Degnan, J. H. and Clark, M. C., "Stark Broadening Measurement of Relativistic Electron Beam Propagation," Bull. Am. Phys. Soc. 25, 913 (1980).

39. Baker, W. L., et al, "Neutron Production in the AFWL SHIVA Electromagnetically-driven Pinch," IEEE Int'l Conf. on Plasma Sci., Madison, WI, Conf. Abstracts IEEE 80 Ch 1544-6 NPS, p. 36 (1980).
40. Baker, W. L., et al, "SHIVA I and I' Results: Electromagnetic Implosion Generation of Pulsed High Energy Density Plasmas," High Energy X-Ray Source Technology Conf., Air Force Weapons Lab, KAFB, Albuquerque, NM, July (1980).
41. Woodall, D. M., et al, "Grazing Incidence Spectrograph Measurements of SHIVA Imploding Linear Radiation Pulse," IEEE Int'l Conf. on Plasma Sci., Madison, WI, Conf. Abstracts, IEEE 80 Ch 1544-6 NPS, p. 90.
42. Woodall, D. M., et al, "Spectral Features in the 80 eV-2 keV Energy Range from an Imploded SHIVA Foil," Bull. Am. Phys. Soc. 25, 872 (1980).

END

FILMED

4-84

DTIC